

Optimization and Modeling  
of the Spin Hall Effect in Dilute Alloys  
A Theoretical Study

---

---

Dissertation

---

---

zur Erlangung des Doktorgrades der Naturwissenschaften  
*doctor rerum naturalium (Dr. rer. nat.)*

der Naturwissenschaftlichen Fakultät II  
Chemie, Physik und Mathematik  
der Martin-Luther-Universität Halle-Wittenberg

vorgelegt von

CHRISTIAN HERSCHBACH  
geboren am 16. April 1986 in Halle (Saale)

**Gutachter:**

1. Prof. Dr. Ingrid Mertig, Martin-Luther-Universität Halle-Wittenberg
2. Prof. Dr. Georg Woltersdorf, Martin-Luther-Universität Halle-Wittenberg
3. Prof. Dr. Jairo Sinova, Johannes Gutenberg-Universität Mainz

**Ort und Tag der Verteidigung:** Halle (Saale), 07. Dezember 2015

---

# Abstract

---

This work studies the extrinsic contributions to the spin Hall effect. The description of electronic structure is based on density functional theory by means of a relativistic Korringa-Kohn-Rostoker Green function method. The electronic and spin transport calculations for skew scattering applied to ultrathin bismuth-doped noble metal films are conducted in the framework of a linearized Boltzmann equation. The computations predict colossal spin Hall effects with spin Hall angles up to about 80% for one-monolayer films. It is shown that the required resonant scattering can be tuned by strain engineering, which deposits the film on an appropriate substrate. The description of bulk systems utilizes a generalized phase shift model, which demonstrates a subtle interplay between spin-orbit and potential scattering in different angular-momentum channels. First steps towards a semiclassical *ab initio* description of the side-jump mechanism are made by two approaches. A Berry curvature-based ansatz leads to impurity-independent results, whereas a generalized phase shift model identifies contributions with and without dependence on the scattering-in term (vertex corrections).

Diese Arbeit untersucht die extrinsischen Beiträge zum Spin-Hall-Effekt. Die Beschreibung der elektronischen Struktur basiert auf Dichtefunktionaltheorie mittels einer relativistischen Greenschen-Funktionsmethode nach Korringa, Kohn und Rostoker. Die Berechnungen zum elektronischen und Spintransport bezogen auf skew scattering, welche für ultradünne, mit Bismut dotierte Edelmetallfilme Anwendung fanden, wurden im Rahmen einer linearisierten Boltzmann-Gleichung durchgeführt. Die Berechnungen sagen riesige Spin-Hall-Effekte mit Spin-Hall-Winkeln bis zu 80% für Monolagenfilme voraus. Es wird gezeigt, dass die erforderliche Resonanzstreuung durch Verzerrung über Filmwachstum auf geeignetem Substrat eingestellt werden kann. Die Beschreibung von Volumensystemen verwendet ein verallgemeinertes Streuphasenmodell, welches ein subtiles Zusammenspiel zwischen Spin-Bahn- und Potentialstreuung in verschiedenen Drehimpulskanälen demonstriert. Erste Schritte in Richtung einer semiklassischen Beschreibung des side jump-Beitrages basierend auf ersten Prinzipien werden durch zwei Ansätze gemacht. Ein auf der Berry Curvature basierender Ansatz führt auf fremdatomunabhängige Resultate während ein weiteres verallgemeinertes Streuphasenmodell Beiträge identifiziert, welche abhängig beziehungsweise unabhängig vom sogenannten scattering-in Term (Vertexkorrekturen) sind.



*"That's the entrance fee."*

— Balázs László Gyórfy



# Contents

Nomenclature	9
<b>1 Introduction</b>	<b>11</b>
<b>2 Theoretical Background</b>	<b>17</b>
2.1 Electronic Structure . . . . .	17
2.1.1 Density Functional Theory . . . . .	17
2.1.2 Green Function . . . . .	20
2.1.3 KKR Method . . . . .	22
2.2 Semiclassical Electronic Transport . . . . .	36
2.2.1 Boltzmann Equation . . . . .	36
2.2.2 Transition Matrix . . . . .	38
2.3 Contributions to the Spin Hall Effect . . . . .	41
2.3.1 Intrinsic Contribution . . . . .	41
2.3.2 Extrinsic Contributions . . . . .	43
2.4 Phase Shift Models for the Spin Hall Effect . . . . .	50
2.4.1 Longitudinal Conductivity . . . . .	50
2.4.2 Skew Scattering . . . . .	51
2.4.3 Side Jump . . . . .	55
<b>3 Results</b>	<b>59</b>
3.1 Bismuth Impurities in Noble Metal Films - Colossal Spin Hall Effect .	59
3.2 Analysis of the Giant Spin Hall Effect in Cu(Bi) Alloys . . . . .	72
3.3 Potential Scattering versus Spin-Orbit Scattering . . . . .	79
3.4 Towards an <i>Ab Initio</i> Semiclassical Description of Side Jump . . . . .	85
<b>4 Summary</b>	<b>91</b>
<b>Appendices</b>	
<b>A Gauge Dependence of Transport Properties</b>	<b>93</b>
<b>B Longitudinal Conductivity in the Phase Shift Model</b>	<b>95</b>
<b>C Integrals Over Spherical Harmonics</b>	<b>97</b>
<b>D Side-Jump Conductivity within the Phase Shift Model</b>	<b>99</b>
<b>E Side-Jump Phase Shift Model - Comparison to Fert and Levy</b>	<b>105</b>
<b>Bibliography</b>	<b>109</b>
<b>List of Publications</b>	<b>117</b>

<b>Eidesstattliche Erklärung</b>	<b>119</b>
<b>Acknowledgment</b>	<b>121</b>
<b>Curriculum Vitae</b>	<b>123</b>

---



# Nomenclature

---

$E_F$ .....	Fermi energy
AHE .....	anomalous Hall effect
ASA .....	atomic sphere approximation
DFT .....	density functional theory
fcc .....	face-centered cubic
GGA .....	generalized gradient approximation
iLDOS .....	impurity local density of states
KKR .....	Korringa-Kohn-Rostoker
LDA .....	local density approximation
LDOS .....	local density of states
ML .....	monolayers
MT .....	muffin tin
MTA .....	muffin-tin approximation
RTA .....	relaxation time approximation
SHA .....	spin Hall angle
SHC .....	spin Hall conductivity
SHE .....	spin Hall effect
SJ .....	side jump
SOC .....	spin-orbit coupling



*“Begin at the beginning and go on till you come to the end: then stop.”*

— Lewis Carroll, *Alice’s Adventures in Wonderland*

Spin electronics, called spintronics in short, was and still is a flourishing field of research [1]. Its main feature is the usage of the electron’s spin degree of freedom. Precisely, spin currents and spin-polarized currents are employed to store, transport or manipulate data [2] but also other applications as the cooling of samples by spin-polarized currents [3] are possible. While the last-mentioned application of spintronics is still at the beginning of its possibilities, further effects already found implementation in everyday life. One of the most famous phenomena with important application is the giant magnetoresistance (GMR) effect, which was discovered independently at Orsay by Albert Fert [4] and at Jülich by Peter Grünberg [5] in 1988. Due to this phenomenon, it became possible to increase the storage capacity of hard disk drives tremendously [6] for which, in consequence, the Nobel price for physics was awarded to both in 2007 [7, 8].

Naturally, spin-polarized transport arises in materials with an uneven spin population at the Fermi energy [9]. Since the consequence of the asymmetric occupation is a magnetic moment, magnetic materials were investigated in order to inject the spin-polarized currents into semiconductors or nonmagnetic samples for a more efficient use. However, problems arising due to conductivity mismatch [10, 11] prevent effective applications of this procedure. Additionally, strong spin-flip processes at the interface between both materials decrease the efficiency since the spin-polarization of the current gets lost [12].

An alternative route circumventing the problem of spin injection is to create spin-polarized or pure spin currents directly in the desired non-magnetic material already used in microelectronics. A phenomenon accomplishing this is the so-called *spin Hall effect* (SHE), whose fundamental background was built already in 1965 by Mott and Massey [13] as well as Landau and Lifshitz [14]. They showed that spin-orbit coupling (SOC) can cause a left-right asymmetry for scattering of electrons with opposite spins. However, only more than three decades later, precisely in 1999, Hirsch proposed a suitable experiment [15]. In the subsequent years, ongoing progress made the effect observable in semiconductors [16] and used it to propose new spintronic devices recently [17].

Nevertheless, the history of the eponymous Hall effect goes back into 1879, when it was observed by Edwin Hall [18]. In his experiment, a conductor was exposed to an electric current in a stationary magnetic field perpendicular to the current. He could observe an electric voltage perpendicular to the directions of both electrical current and magnetic field since the evocative Lorentz force deflects the electrons to one

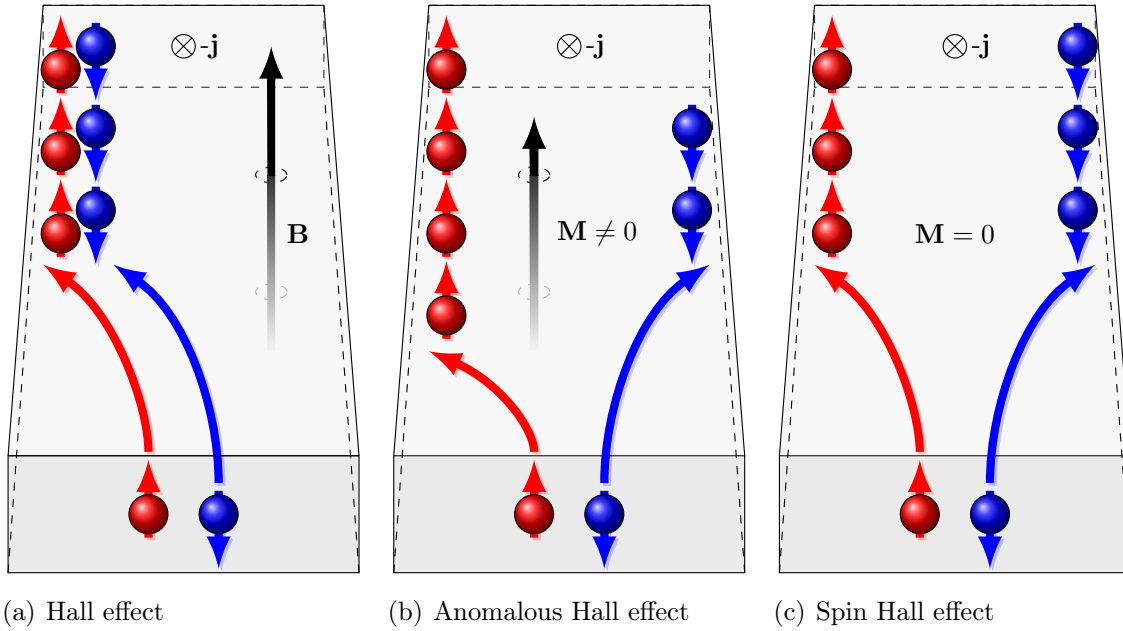


Figure 1.1.: Various Hall effects. The ordinary Hall effect is caused by the Lorentz force which pushes the conduction electrons to one edge of the sample. Anomalous (or extraordinary) and spin Hall effect occur in absence of a magnetic field. Due to the either finite or vanishing magnetization, the experimental results differ, whereas the origin of both effects is the same.

edge of the sample as illustrated in figure 1.1(a). About two years later, Hall published results for ferromagnetic samples where the effect was about ten times larger than for nonmagnetic materials [19]. Considering the Hall resistivity in dependence of the applied magnetic field  $H$

$$\rho_{\text{Hall}}(H) = \mu_0 R_s M(H) + \mu_0 R_0 H, \quad (1.1)$$

the special character of the discovered anomalous Hall effect (AHE) can be revealed as a steep slope for small values of  $H$  in contrast to a much gentler slope for large magnetic inductions as can be seen in figure 1.2. In fact, the first part is proportional to the sample's magnetization  $M$  which saturates at a specific value for  $H$ , whereas the direct effect of the magnetic field itself is much lower [20, 21]. Equation (1.1) contains the vacuum permeability  $\mu_0$  as well as the constants  $R_s$  and  $R_0$  which characterize the strength of the anomalous and the ordinary Hall resistivities, respectively [22].

It took until the 1950s when Karplus and Luttinger [23] as well as Smit [24, 25] presented first explanations for the anomalous Hall effect which is sketched in figure 1.1(b). Basically, different mechanisms lead to an asymmetric spin-dependent deflection of electrons. Due to the unequal number of electrons in the sample with spin state *up* or *down*, the entire number of electrons at opposite edges differ which leads to the emergence of the Hall voltage. Since the occurrence of spin-dependent deflection processes is not in the least linked to the magnetic character of the material, the underlying mechanisms arise in nonmagnetic samples as well. The experimental result is obviously different in comparison to magnets because the equal number of

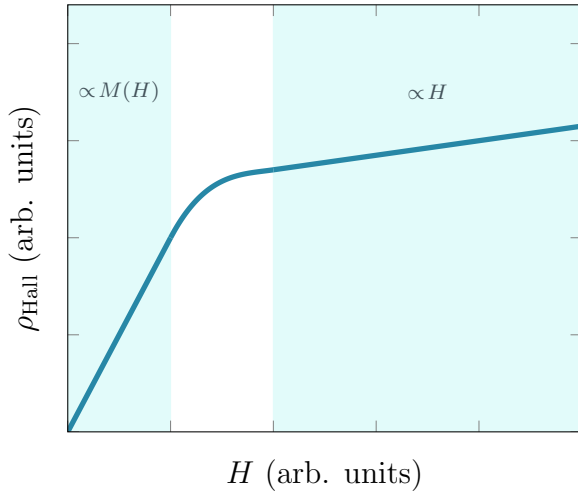


Figure 1.2: Hall resistivity depending on the applied magnetic field. The domains with the different slopes can be ascribed to the anomalous Hall effect (proportional to the magnetization  $M$ ) and the ordinary Hall effect linear in  $H$ .

spin-up and spin-down electrons enforces a vanishing Hall voltage. Nevertheless, the deflection processes lead to spin accumulation and the appearance of spin currents. The emergence of such spin currents caused by charge currents in non-magnetic materials is called spin Hall effect [26] and is depicted in figure 1.1(c).

Prior to a closer consideration of the underlying physics that leads to the spin-dependent electron deflection, a basic definition of spin currents in comparison to charge currents is required. In order to get an easy picture, a non-relativistic treatment can be used which leads to the two-current model [27] with two independent spin channels contributing to the total current. Within this picture, the total charge current density is given by the sum

$$\mathbf{j}_c = \mathbf{j}^\uparrow + \mathbf{j}^\downarrow \quad (1.2)$$

of both spin channel contributions, whereas the difference

$$\mathbf{j}_s = \mathbf{j}^\uparrow - \mathbf{j}^\downarrow \quad (1.3)$$

leads to the spin current density. Ohm's law

$$\mathbf{j} = \underline{\sigma} \mathbf{E}, \quad (1.4)$$

which connects the electric current density to the applied electric field via the conductivity tensor, can be formulated for each spin channel separately

$$\mathbf{j}^{\uparrow(\downarrow)} = \underline{\sigma}^{\uparrow(\downarrow)} \mathbf{E}. \quad (1.5)$$

The spin-dependent conductivity tensors for systems with cubic symmetry and a spin-quantization axis along  $z$  direction possess special symmetries and have the forms [28]

$$\underline{\sigma}^\uparrow = \begin{pmatrix} \sigma_{xx}^\uparrow & -\sigma_{yx}^\uparrow & 0 \\ \sigma_{yx}^\uparrow & \sigma_{xx}^\uparrow & 0 \\ 0 & 0 & \sigma_{zz}^\uparrow \end{pmatrix} \quad \text{and} \quad \underline{\sigma}^\downarrow = \begin{pmatrix} \sigma_{xx}^\uparrow & \sigma_{yx}^\uparrow & 0 \\ -\sigma_{yx}^\uparrow & \sigma_{xx}^\uparrow & 0 \\ 0 & 0 & \sigma_{zz}^\uparrow \end{pmatrix} \quad (1.6)$$

when the presence of time reversal symmetry is assumed. I want to emphasize that the spin-down conductivity tensor was expressed in terms of spin-up quantities

deliberately in order to highlight the existing relationship. Combining the above equations one can easily find that the charge conductivity tensor

$$\underline{\sigma}^c = \underline{\sigma}^\uparrow + \underline{\sigma}^\downarrow = \begin{pmatrix} 2\sigma_{xx}^\uparrow & 0 & 0 \\ 0 & 2\sigma_{xx}^\uparrow & 0 \\ 0 & 0 & 2\sigma_{zz}^\uparrow \end{pmatrix} = \begin{pmatrix} \sigma_{xx} & 0 & 0 \\ 0 & \sigma_{xx} & 0 \\ 0 & 0 & \sigma_{zz} \end{pmatrix} \quad (1.7)$$

does not show off-diagonal, i.e. Hall, components, whereas the spin conductivity tensor

$$\underline{\sigma}^s = \underline{\sigma}^\uparrow - \underline{\sigma}^\downarrow = \begin{pmatrix} 0 & -2\sigma_{yx}^\uparrow & 0 \\ 2\sigma_{yx}^\uparrow & 0 & 0 \\ 0 & 0 & 0 \end{pmatrix} = \begin{pmatrix} 0 & -\sigma_{yx}^s & 0 \\ \sigma_{yx}^s & 0 & 0 \\ 0 & 0 & 0 \end{pmatrix} \quad (1.8)$$

merely consists of those. As was already mentioned, the spin Hall effect describes the appearance of a transverse spin current by reason of an applied charge current. Accordingly, the quantification of the strength of the phenomenon is commonly carried out by the ratio of the so-called *spin Hall conductivity* (SHC) and the longitudinal charge conductivity

$$\alpha = \frac{\sigma_{yx}^s}{\sigma_{xx}}, \quad (1.9)$$

which is called the *spin Hall angle* (SHA).

With the understanding that the spin Hall effect manifests itself via an off-diagonal component in the (spin) conductivity tensor, it is worth to consider the underlying physics. It is commonly accepted to distinguish the following different mechanisms, which can be identified by various approaches [22, 26, 29]. Firstly, it is possible to separate the *intrinsic* contribution appearing in ideal crystals. Additionally, two *extrinsic* effects emerge in the presence of defects or impurities in the system. They are known as the *skew-scattering* and *side-jump* mechanisms. As shown in figure 1.3, generally, all these effects are superimposed in the sample which provides the total spin Hall conductivity as the sum of the corresponding contributions

$$\sigma_{yx}^s = \sigma_{yx}^{s \text{ intr}} + \sigma_{yx}^{s \text{ sj}} + \sigma_{yx}^{s \text{ skew}}. \quad (1.10)$$

The knowledge of the single contributions to the SHE eases the interpretation of experimental results. For instance, several investigations on gold samples report results varying by up to two orders of magnitude [30–32] including the *giant* SHE in Au with  $\alpha \approx 11\%$  obtained by Seki et al. [30]. The large differences can only be understood in terms of extrinsic contributions with various strengths since the intrinsic part should be the same in all cases. The influence of extrinsic effects can be very large, especially in the dilute impurity limit where the skew-scattering contribution dominates [33]. Therefore, the investigation of the skew-scattering mechanism is an important step in order to reveal systems with a large SHE. A theoretical investigation by Gradhand et al. [34] predicted the alloy Cu(Bi), i.e. bismuth impurities in copper, to provide a large SHA of the order of 10%. The occurrence of a giant SHE in this material combination was recently confirmed experimentally [35]. Besides the approach of varying the skew-scattering contribution due to different impurities in bulk hosts [34, 36], experiments of Gu et al. [37] targeted thin gold films with platinum impurities and revealed that the reduced sample dimension can have significant impact on the obtained results. These findings motivated the theoretical

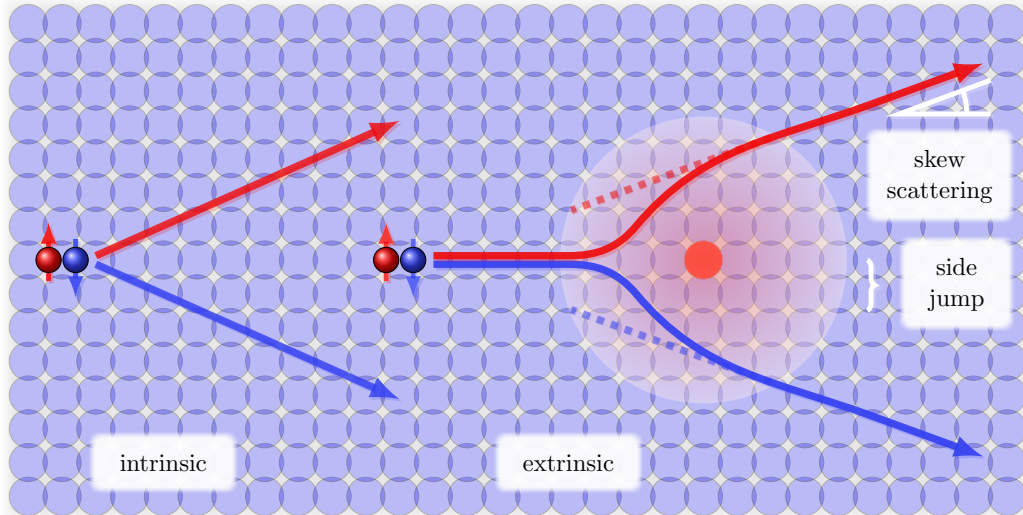


Figure 1.3.: Classical trajectories of spin-up and spin-down electrons illustrating intrinsic and extrinsic contributions to the spin Hall effect. While the intrinsic mechanism affects the electrons in the ideal sample, the skew-scattering and side-jump effects occur due to scattering events at defects and impurities. Skew scattering results in an angle between the trajectories before and after scattering whereas side jump emerges as a displacement. It is noteworthy that intrinsic, skew-scattering and side-jump contributions do not necessarily have the same sign for the respective spin state.

study on ultrathin films that showed a strongly enhanced effect for one-monolayer films as well as a large influence of the impurity position within the system [H1]. Accordingly, a big part of this thesis is dedicated to the combination of the aforementioned results. In particular, the skew-scattering contribution and its potential to optimize the spin Hall effect in noble-metal thin-film systems with bismuth impurities shall be investigated. For this task, an established *ab initio* method is used. While the electronic structure is obtained on the basis of density functional theory (DFT) by means of a relativistic Korringa-Kohn-Rostoker (KKR) Green function method, the transport calculations are carried out within a semiclassical approach using the linearized Boltzmann equation.

The used *ab initio* method is computationally quite demanding. In order to circumvent some of the required efforts, a phase shift model describing skew scattering in bulk samples will be investigated. This approach is based on a generalization of the resonant scattering model proposed by Fert and Levy [38] in order to include all potentially contributing orbital-momentum channels. Within the thesis, the validity of this model will be discussed by comparison to material-specific first-principle calculations. Additionally, the reformulation will allow for conclusions that go beyond the original model of Fert and Levy.

In addition to the investigation of skew scattering, the side-jump contribution to the SHE will be examined by two simplified approaches. The first one follows a suggestion of Sinitsyn et al. [39] focusing on the host properties expressed in terms of the Berry curvature obtained from first principles here. In contrast to this approach, the second ansatz stresses the system's impurity properties. Precisely, the resonant scattering model from Fert and Levy [38] is extended similarly to the mentioned case of skew scattering and will be applied to certain material combinations.





# Theoretical Background

---

*“When your code is properly written, it knows more than you.”*

— Leonid Sandratskii

## 2.1. Electronic Structure

### 2.1.1. Density Functional Theory

In order to describe a solid from a quantum mechanical point of view, the Schrödinger equation

$$\hat{H} \psi(\mathbf{r}) = E \psi(\mathbf{r}) \quad \text{with} \quad \int d^3r \psi^*(\mathbf{r}) \psi(\mathbf{r}) = 1 \quad (2.1)$$

serves as a suitable starting point. It connects the Hamilton operator  $\hat{H}$  via the wave function  $\psi(\mathbf{r})$  with the energy eigenvalue  $E$ . In a solid consisting of nuclei (n) and electrons (e), the Hamiltonian consists of a sum over several contributions

$$\hat{H} = \hat{\mathcal{T}}_n + \hat{\mathcal{T}}_e + \hat{V}_{nn} + \hat{V}_{en} + \hat{V}_{ee}. \quad (2.2)$$

The single terms represent the kinetic energy ( $\hat{\mathcal{T}}$ ) of nuclei and electrons as well as the interaction potential ( $\hat{V}$ ) between nuclei, electrons and nuclei, and electrons, respectively.

A first and fundamental approximation to simplify equation (2.2) is the adiabatic or Born-Oppenheimer approximation [40, 41]. It relies on the large discrepancy of electron and proton mass which differ by three orders of magnitude. Hence, it is a proper assumption to consider the motion of electrons and nuclei independently. Accordingly, the Hamiltonian describing the electron motion in the field of static nuclei reads

$$\hat{H}_e = -\frac{\hbar^2}{2m_e} \sum_{i=1}^{N_e} \frac{\partial^2}{\partial \mathbf{r}_i^2} + \sum_{i=1}^{N_e} V(\mathbf{r}_i) + \frac{1}{2} \sum_{i=1}^{N_e} \sum_{\substack{j=1 \\ j \neq i}}^{N_e} \frac{e^2}{|\mathbf{r}_i - \mathbf{r}_j|}, \quad (2.3)$$

where the external potential  $V(\mathbf{r}_i)$  describes the Coulomb interaction between electrons and nuclei. The other variables have their usual meaning of Planck’s constant ( $\hbar$ ), electron mass ( $m_e$ ), number of electrons ( $N_e$ ) and electron space coordinate ( $\mathbf{r}_i$ ). Despite this simplification, the problem (2.3) remains unsolvable because the electron wave function  $\psi(\mathbf{r}_1, \dots, \mathbf{r}_{N_e})$  depends on approximately  $10^{23}$  coordinates which do not decouple.

In order to solve the introduced problem it is worth to consider density functional theory as a suitable tool. The basis of this concept is the theorem of Hohenberg and Kohn which says that the ground state energy of a many-body system is a unique functional of the electron density,  $E[n(\mathbf{r})]$ , for a given external potential  $V(\mathbf{r})$  [42]. A possible decomposition valuable for the further analysis reads

$$E[n(\mathbf{r})] = \mathcal{T}[n(\mathbf{r})] + \int d^3r V(\mathbf{r}) n(\mathbf{r}) + \frac{1}{2} \iint d^3r d^3r' \frac{e^2}{|\mathbf{r} - \mathbf{r}'|} n(\mathbf{r}) n(\mathbf{r}') + E_{xc}[n(\mathbf{r})]. \quad (2.4)$$

The main problem of equation (2.4) is the unknown functional dependence of the kinetic energy  $\mathcal{T}[n(\mathbf{r})]$  and the exchange-correlation energy  $E_{xc}[n(\mathbf{r})]$  on the electron density. This issue can be overcome by a variational procedure proposed by Kohn and Sham [43] which leads to the so-called Kohn-Sham equations

$$\left( -\frac{\hbar^2}{2m} \nabla^2 + V_{\text{eff}}(\mathbf{r}) \right) \psi_i(\mathbf{r}) = E_i \psi_i(\mathbf{r}), \quad (2.5a)$$

$$V_{\text{eff}}(\mathbf{r}) = V_{\text{eff}}[n(\mathbf{r})] = V(\mathbf{r}) + \int d^3r' \frac{e^2 n(\mathbf{r}')}{|\mathbf{r} - \mathbf{r}'|} + \frac{\delta E_{xc}(n(\mathbf{r}))}{\delta n(\mathbf{r})}. \quad (2.5b)$$

This system of equations describes the motion of non-interacting electrons under the influence of an effective external potential in a Schrödinger-like structure. Nevertheless, if the exact exchange-correlation potential is known, it yields the same electron density as the system consisting of interacting particles. Since an exact term for the exchange-correlation energy is unidentified yet, it is an important task to find an appropriate ansatz for the exchange-correlation energy. A usual approach, which was tested successfully for metallic systems, is the so-called local density approximation (LDA). As a basic assumption, it supposes a locally slowly changing electron density which leads to

$$E_{xc}^{\text{LDA}}[n(\mathbf{r})] = \int d^3r \varepsilon_{xc}(n(\mathbf{r})) n(\mathbf{r}). \quad (2.6)$$

In this equation  $\varepsilon_{xc}(n(\mathbf{r}))$  represents the exchange and correlation energy per electron in a homogeneous electron gas with density  $n$ . The electron density  $n(\mathbf{r})$  can be parametrized by a set of one-electron wave functions

$$n(\mathbf{r}) = \sum_{i=1}^{N_e} |\psi_i(\mathbf{r})|^2. \quad (2.7)$$

In order to get the fundamentally important electron density from equation (2.7), it is required to pass through a self-consistent Kohn-Sham loop which should be initiated with a problem-adapted starting density  $\tilde{n}(\mathbf{r})$ . By this, the effective potential  $V_{\text{eff}}(\mathbf{r}) = V_{\text{eff}}[\tilde{n}(\mathbf{r})]$  is calculated via equation (2.5b) and used to solve the Kohn-Sham equation (2.5a). The resulting single-particle wave functions can be utilized to get the new electron density  $n(\mathbf{r})$  via equation (2.7). For  $n(\mathbf{r}) \neq \tilde{n}(\mathbf{r})$ ,  $n(\mathbf{r})$  serves as the new starting density for another cycle. In case of a consistency  $n(\mathbf{r}) = \tilde{n}(\mathbf{r})$ , the correct effective potential which leads to the sought electron density is found and this part of the problem is solved.

For the investigation of the spin Hall effect, it is essential to introduce spin-orbit coupling in the used formalism. Hence, a relativistic approach [44, 45] needs to be used. The corresponding Kohn-Sham-Dirac equation for the non-magnetic case considered here is

$$[c\boldsymbol{\alpha} \cdot \mathbf{p} + \underline{\beta}m_e c^2 + V_{\text{eff}}(\mathbf{r})\underline{\mathbb{1}}_4] \psi(E, \mathbf{r}) = W\psi(E, \mathbf{r}), \quad (2.8)$$

where  $V_{\text{eff}}(\mathbf{r})$  has the same meaning as in equation (2.5b). Here,  $\underline{\alpha}_i$  and  $\underline{\beta}$  indicate the four-dimensional Dirac matrices

$$\boldsymbol{\alpha} = (\underline{\alpha}_x, \underline{\alpha}_y, \underline{\alpha}_z) \quad \text{with} \quad \underline{\alpha}_i = \begin{pmatrix} \underline{\mathbb{0}}_2 & \underline{\sigma}_i \\ \underline{\sigma}_i & \underline{\mathbb{0}}_2 \end{pmatrix}, \quad (2.9)$$

$$\underline{\sigma}_x = \begin{pmatrix} 0 & 1 \\ 1 & 0 \end{pmatrix} \quad \underline{\sigma}_y = \begin{pmatrix} 0 & -i \\ i & 0 \end{pmatrix} \quad \underline{\sigma}_z = \begin{pmatrix} 1 & 0 \\ 0 & -1 \end{pmatrix}, \quad (2.10)$$

$$\underline{\beta} = \begin{pmatrix} \underline{\mathbb{1}}_2 & \underline{\mathbb{0}}_2 \\ \underline{\mathbb{0}}_2 & -\underline{\mathbb{1}}_2 \end{pmatrix} \quad \underline{\mathbb{1}}_4 = \begin{pmatrix} \underline{\mathbb{1}}_2 & \underline{\mathbb{0}}_2 \\ \underline{\mathbb{0}}_2 & \underline{\mathbb{1}}_2 \end{pmatrix} \quad \underline{\mathbb{1}}_2 = \begin{pmatrix} 1 & 0 \\ 0 & 1 \end{pmatrix} \quad \underline{\mathbb{0}}_2 = \begin{pmatrix} 0 & 0 \\ 0 & 0 \end{pmatrix} \quad (2.11)$$

consisting of Pauli and unit matrices. The relativistic energy-momentum relation is given by [45]

$$W^2 = c^2 p^2 + m_e^2 c^4, \quad E \equiv W - m_e c^2, \quad (2.12)$$

where  $p$  and  $c$  represent the electron momentum and the speed of light, respectively. The eigenfunctions  $\psi$  of the Kohn-Sham-Dirac Hamiltonian in equation (2.8) obey a bispinor decomposition [44]

$$\psi(E, \mathbf{r}) = \sum_{\kappa\mu} \begin{pmatrix} g_{\kappa}(E, r) \chi_{\kappa\mu}(\hat{\mathbf{r}}) \\ i f_{\kappa}(E, r) \chi_{-\kappa\mu}(\hat{\mathbf{r}}) \end{pmatrix} \quad (2.13)$$

within relativistic  $\kappa\mu$  representation [44, 45] related to the quantum numbers  $l$  and  $j$  by

$$\kappa = \begin{cases} l & , j = l - \frac{1}{2} \\ -l - 1 & , j = l + \frac{1}{2} \end{cases} \quad \text{and} \quad \mu \in \{-j, -j + 1, \dots, j - 1, j\}. \quad (2.14)$$

The  $\chi_{\kappa\mu}$  are the so-called spin-angular functions. Their relation to the spherical harmonics is given by the Clebsch-Gordan coefficients  $C$  and the non-relativistic spinors [45]

$$\Phi_{\frac{1}{2}} = \begin{pmatrix} 1 \\ 0 \end{pmatrix}, \quad \Phi_{-\frac{1}{2}} = \begin{pmatrix} 0 \\ 1 \end{pmatrix} \quad (2.15)$$

as

$$\chi_{\kappa\mu}(\hat{\mathbf{r}}) = \sum_{s=\pm\frac{1}{2}} C(l, j, \frac{1}{2}|\mu - s, s) Y_l^{\mu-s}(\hat{\mathbf{r}}) \Phi_s. \quad (2.16)$$

### 2.1.2. Green Function

In this work, the method to solve the Kohn-Sham-Dirac equation (2.8) with the effective potential  $V_{\text{eff}}$  from (2.5b) is the so-called Korringa-Kohn-Rostoker formalism, which is explained in more detail in subsection 2.1.3. Since it is a Green function technique, I will shortly discuss the necessary basics which rely on reference [46] in large part.

The Green function approach is ideally suited to deal with ordinary linear homogeneous differential equations of the type presented in equation (2.1) and used in the following as

$$\hat{H}(\mathbf{r}) \psi_i(\mathbf{r}) = E_i \psi_i(\mathbf{r}). \quad (2.17)$$

The Green function itself in operator representation is the solution of the equation

$$\left[ z - \hat{H} \right] \hat{G}(z) = \mathbb{1} \quad (2.18)$$

with the complex energy parameter  $z = E + i\eta$ . Since the imaginary part  $\eta$  is defined to be positive, only the upper part of the complex energy plane is considered. Taking into account the completeness of the eigenfunction system  $\psi_i(\mathbf{r})$ , it is possible to write the so-called spectral representation of the Green function by combining equations (2.17) and (2.18)

$$\hat{G}(E) = \lim_{\eta \rightarrow 0^+} \sum_i \frac{|\psi_i\rangle \langle \psi_i|}{E + i\eta - E_i}. \quad (2.19)$$

Equation (2.19) delivers the Green function depending on real energies  $E$  which is the appropriate quantity for practical applications. In order to get the fundamentally important electron density, which was already mentioned in equation (2.7), the Dirac identity

$$\lim_{y \rightarrow 0^+} \frac{1}{x \pm iy} = \mathcal{P} \left( \frac{1}{x} \right) \mp i\pi \delta(x) \quad (2.20)$$

containing the Cauchy principal value  $\mathcal{P}$  can be employed. Applying equation (2.20) to the real space analogue of the spectral representation of the Green function (2.19) allows for an identification with the local density of states (LDOS)

$$n(\mathbf{r}, E) = \sum_i |\psi_i(\mathbf{r})|^2 \delta(E - E_i) \equiv -\frac{1}{\pi} \text{Im} G(\mathbf{r}, \mathbf{r}; E). \quad (2.21)$$

On the one hand, equation (2.21) gives the possibility to obtain the charge density as the fundamental quantity in DFT

$$n(\mathbf{r}) = \int_{-\infty}^{E_F} dE n(\mathbf{r}, E) = -\frac{1}{\pi} \int_{-\infty}^{E_F} dE \text{Im} G(\mathbf{r}, \mathbf{r}; E) \quad (2.22)$$

via an energy integration over all occupied electronic states. The upper boundary is defined by the Fermi energy ( $E_F$ ) which separates occupied from unoccupied states. On the other hand, an integration over the system volume  $V_s$  results in the density

of states

$$n(E) = \int_{V_s} d^3r n(\mathbf{r}, E) = -\frac{1}{\pi} \text{Im Tr } \hat{G}(E), \quad (2.23)$$

if the normalization of the eigenfunctions is taken into account and  $\text{Tr } \hat{G}(E) = \sum_i \langle \psi_i | \hat{G}(E) | \psi_i \rangle$  represents the trace of the Green function.

As shown in equations (2.21) - (2.23), the knowledge of the Green function's diagonal element  $G(\mathbf{r}, \mathbf{r}; E)$  leads to the knowledge of the electronic properties of a system via the LDOS. The remaining task is to find an appropriate way to determine the Green function. Although the evaluation of equation (2.19) is feasible, it is possibly not the most elegant way for practical applications.

A convenient approach is to start from two Hamilton operators  $\hat{H}$  and  $\hat{H}$  which differ by a potential difference  $\Delta V = \hat{H} - \hat{H}$  only. The definitions of respective Green functions are carried out analogously to equation (2.18)

$$\left[ z - \hat{H} \right] \hat{G}(z) = \mathbb{1} \quad \text{and} \quad \left[ z - \hat{H} \right] \hat{G}(z) = \mathbb{1}. \quad (2.24)$$

Combining these equations with the definition of  $\Delta V$  leads to the so-called Dyson equation [44]

$$\hat{G}(z) = \hat{G}(z) + \hat{G}(z) \Delta V \hat{G}(z) \quad (2.25)$$

which allows to calculate the (unknown) Green function  $\hat{G}(z)$  for the system of interest from the (known) Green function  $\hat{G}(z)$  of a reference system based on the knowledge of the potential perturbation  $\Delta V$ . Defining the transition operator  $\hat{T}$  with

$$\hat{T}(z) \hat{G}(z) = \Delta V \hat{G}(z) \quad (2.26)$$

is a helpful step to enable an effective determination of  $\hat{G}(z)$  since it yields

$$\hat{T}(z) = \Delta V \left( \mathbb{1} - \hat{G}(z) \Delta V \right)^{-1}. \quad (2.27)$$

Evaluating equation (2.27) allows for the calculation of the  $T$  operator if the Green function of the reference system and the corresponding potential difference are known. Using the transition operator delivers the Dyson equation in its alternative form

$$\hat{G}(z) = \hat{G}(z) + \hat{G}(z) \hat{T}(z) \hat{G}(z) \quad (2.28)$$

to get the sought Green function directly from the reference Green function. In addition, the wave functions of the considered system can be calculated if the reference wave functions are known. The analogue formulation to equations (2.25) and (2.28) for the wave function  $|\psi\rangle$  is called Lippmann-Schwinger equation and reads

$$\begin{aligned} |\psi\rangle &= |\hat{\psi}\rangle + \hat{G}(E) \hat{T}(E) |\hat{\psi}\rangle \\ &= |\hat{\psi}\rangle + \hat{G}(E) \Delta V |\psi\rangle. \end{aligned} \quad (2.29)$$

### 2.1.3. KKR Method

The electronic structure calculations performed during this work are based on the multiple-scattering Green function method developed by J. Korringa [47], W. Kohn and N. Rostoker [48]. Accordingly, this technique is commonly known as KKR method [44].

Beyond the possibility to use the KKR approach for band structure calculations of ideal three-dimensional metals, some further development allowed for additional applications. Important steps were taken by Zeller and Dederichs [49–51] in order to consider impurities in crystals. The evolution to the screened KKR formalism allowed for an effective treatment of systems with larger unit cells. This is most convenient to study layered systems and free-standing films [52, 53]. The used implementation is well described in the corresponding PhD theses of P. Zahn [53] and M. Czerner [54].

One of the important characteristics of the KKR formalism is that the scattering properties of single atoms can be considered independently from the contributions due to their structural arrangement. In short, it is possible to examine the single-scattering contribution and the multiple-scattering contribution separately.

In order to use this feature, a first approach, called muffin-tin approximation (MTA), treats single atoms in separate unit cells. The spherically symmetric potential of an isolated atom serves as a suitable approximation for the atomic potentials in a solid. According to this, one considers a sphere  $n$  at the lattice site  $\mathbf{R}_n = \tilde{\mathbf{r}} - \mathbf{r}$  with a spherically symmetric potential

$$V_n(\mathbf{r}) = \begin{cases} V_{\text{atom}}(r), & r < R_{\text{MT}} \\ 0, & r > R_{\text{MT}} \end{cases} \quad (2.30)$$

that fits completely within the unit cell. In this description,  $\mathbf{R}_n$  is a lattice vector,  $\mathbf{r}$  is a local vector in the muffin-tin (MT) sphere and  $\tilde{\mathbf{r}}$  is the global vector coordinate. The corresponding radius of the sphere,  $R_{\text{MT}}$ , is the so-called muffin-tin radius. The name is connected to the look of a muffin tin if several of such spheres come together as shown in figure 2.1(a). The superposition of these single-particle potentials gives the crystal potential

$$V(\mathbf{r}) = \sum_n V_n(\mathbf{r}). \quad (2.31)$$

A first problem of this approach arises if one tries to calculate for example the density of states according to equation (2.23). The integration within the MT spheres is easy due to the chosen symmetry of the potential in equation (2.30). For the interstitial region, this advantage is lost. To overcome this problem, the atomic sphere approximation (ASA) can be used. The central point is that the radius of the sphere which limits the region of non-zero potential is enlarged until its volume is equal to the unit cell volume. Consequently, integrations as in equation (2.23) run over spherically symmetric regions only, which simplifies the procedure. The disadvantage is that overlapping areas are counted twice while interstitial domains are neglected. A schematic picture of this situation is shown in figure 2.1(b). Therefore, this approximation provides good results if the integrated contributions of both parts, the neglected and the double counted, are similar. For metallic systems, this

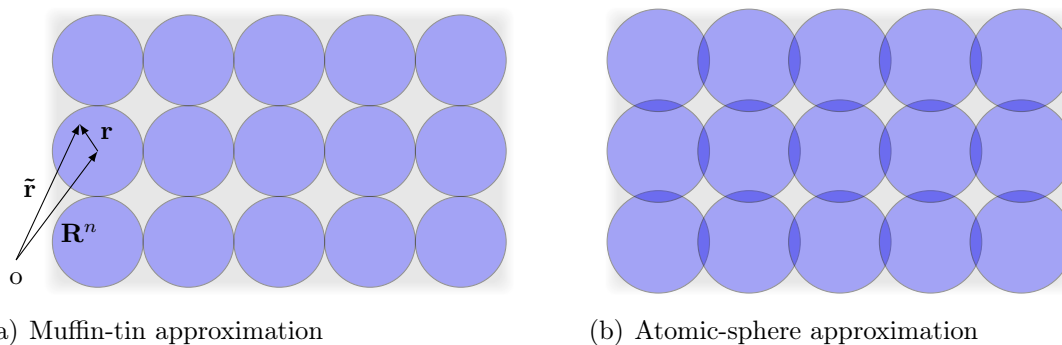


Figure 2.1.: Schematic illustration of the potential landscape for muffin-tin and atomic-sphere approximation.

is usually the case.

Subsequently, the contribution due to the single-site scattering shall be discussed and is followed by a related consideration of the multiple-scattering contribution. For reasons of simplicity, the formulation will be presented in the non-relativistic picture. Nevertheless, an introduction into the relativistic formalism will be presented as well. For the presentation of the used KKR formalism to determine the electronic structure of the investigated systems, atomic units are used which means  $\hbar = 2m = \frac{e^2}{2} = 1$  and  $c = 274.074$ . Consequently, lengths are given in units of the Bohr radius  $a_0 = 0.0529177$  nm while energies are given in Rydbergs with  $1\text{Ry} = 13.6058$  eV.

### Free-Particle Solution

The evaluation of the Dyson equation (2.28) or the Lippmann-Schwinger equation (2.29) requires knowledge of the Green function and wave function of a reference system. Since they can be written analytically for the free-particle case, this should serve as the origin for further considerations. The interest is dedicated to the Schrödinger equation for free particles

$$\left(-\frac{\partial^2}{\partial \mathbf{r}^2} - \mathring{E}_{\mathbf{k}}\right) \mathring{\psi}_{\mathbf{k}}(\mathbf{r}) = 0. \quad (2.32)$$

The resulting plane wave  $\mathring{\psi}_{\mathbf{k}}$  having the continuous energy spectrum  $\mathring{E}_{\mathbf{k}} = k^2$  can be expanded in terms of a localized complete set of basis functions. Using a basis set with spherical symmetry, which is needed especially evaluating the single-site scattering problem later on, the wave function can be rewritten as

$$\mathring{\psi}_{\mathbf{k}}(\mathbf{r}) = \frac{1}{\sqrt{V}} e^{i\mathbf{k}\cdot\mathbf{r}} = \frac{4\pi}{\sqrt{V}} \sum_L i^l j_l(kr) Y_L(\hat{\mathbf{r}}) Y_L^*(\hat{\mathbf{k}}) \quad (2.33)$$

and is normalized to the system volume  $V$ . Furthermore, it is expanded using the combined index  $L = \{l, m\}$  which includes the angular momentum  $l$  as well as the magnetic quantum number  $m$ . The wave function's angular dependence is described by the complex spherical harmonics  $Y_L$  which depend on the unit vectors along  $\mathbf{r}$

or  $\mathbf{k}$  direction, respectively. The radial part comes from the corresponding radial Schrödinger equation for free particles

$$\left( -\frac{1}{r} \frac{\partial^2}{\partial r^2} r + \frac{l(l+1)}{r^2} - E \right) \psi_l(r, E) = 0 \quad (2.34)$$

and contributes to the wave function as the spherical Bessel function  $j_l(kr)$ . The spherical Neumann functions  $n_l(kr)$  also solve equation (2.34) but, in contrast to  $j_l(kr)$ , diverge at the origin and therefore cannot contribute to the obtained series expansion. Nevertheless, they, as well as the spherical Hankel functions  $h_l^\pm(kr) = n_l(kr) \mp i j_l(kr)$ , are important for the completeness of the differential equation's solution.

An interesting and later on helpful characteristic between  $j_l(kr)$  and  $n_l(kr)$  is that they fulfil the Wronski relation

$$W[j_l(kr), n_l(kr)] = \begin{vmatrix} j_l(kr) & n_l(kr) \\ \frac{d}{d(kr)} j_l(kr) & \frac{d}{d(kr)} n_l(kr) \end{vmatrix} = \frac{1}{k^2 r^2}, \quad (2.35)$$

which can be obtained easily in the large argument limit. Being non-zero, equation (2.35) shows that both solutions are linearly independent.

Having the wave function in hand it is now possible to obtain the Green function using equations (2.19) and (2.33). A detailed derivation can be found in appendix A1.3 of reference [55]. The final result for the free-electron Green function in space representation reads

$$\hat{g}(\mathbf{r}, \mathbf{r}'; E) = \sum_L Y_L(\hat{\mathbf{r}}) \hat{g}_l(r, r'; E) Y_L^*(\hat{\mathbf{r}}'), \quad (2.36)$$

$$\hat{g}_l(r, r'; E) = \sqrt{E} j_l(kr_<) h_l^+(kr_>), \quad (2.37)$$

where the angular-resolved radial Green function  $\hat{g}_l(r, r'; E)$  includes  $r_< = \min\{r, r'\}$  and  $r_> = \max\{r, r'\}$ .

## Single-Site Scattering

The formulation of the single-site scattering problem

$$\left( -\frac{\partial^2}{\partial \mathbf{r}^2} + V(r) - E \right) \psi_L^n(\mathbf{r}) = 0 \quad (2.38)$$

differs from the free-particle case (2.32) by a spherically symmetric potential  $V(r)$  which retains the angular momentum conservation. Consequently, the scattering states decouple in an angular part represented by the (complex) spherical harmonics and a radial contribution pursuant to

$$\psi_L = R_l(r, E) Y_L(\hat{\mathbf{r}}). \quad (2.39)$$

The angular-resolved wave function in (2.33) and the Green function (2.37) for the free particle case can serve as a reference system in order to obtain  $R_l(r, E)$  from a



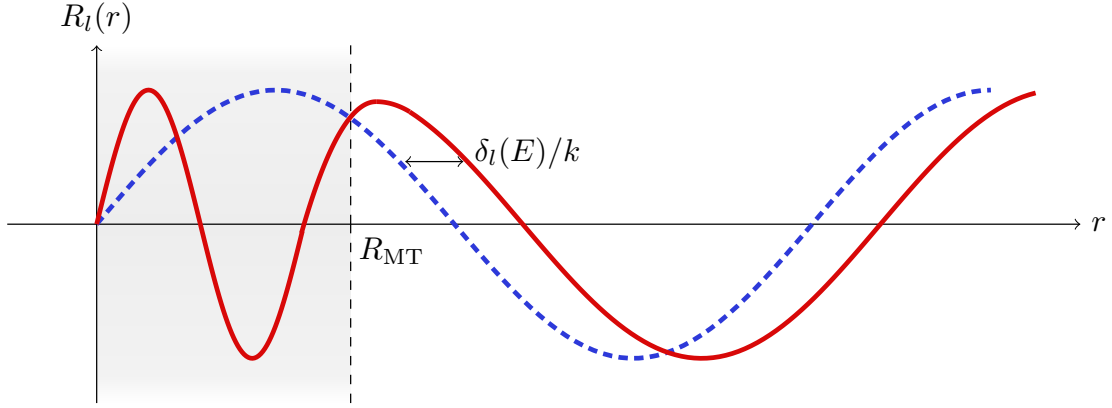


Figure 2.2.: Schematic sketch to visualize the scattering phase shift  $\delta_l(E)$  between the radial wave function for spherically symmetric potential (solid red) and free particle solution (dashed blue) outside the muffin-tin radius  $R_{\text{MT}}$ .

corresponding radial Lippmann-Schwinger equation according to (2.29). The combination of these equations, using an angular momentum expansion for the transition matrix, leads to the regular solution

$$R_l(r, E) = j_l(kr) + k t_l(E) h_l^+(kr). \quad (2.40)$$

The scattering phase shifts, which play an important role in parts of the thesis, are introduced in detail in what follows.

Outside the muffin-tin sphere, far away from the scattering potential ( $kr \gg 1$ ), the regular free-particle solution  $j_l(kr)$  and the regular single-site scattering solution  $R_l(r, E)$  feel the same vanishing potential and should behave equally. The only difference is a phase shift  $\delta_l(E)$  accompanied by the scattered wave during the interaction with  $V(r)$ . Considering the asymptotic behavior of the spherical Bessel functions, the situation can be formulated as [55, 56]

$$R_l(r, E) \xrightarrow{\lim kr \rightarrow \infty} j_l(kr + \delta_l(E)) = C_l \frac{\sin(kr - l\frac{\pi}{2} + \delta_l(E))}{kr}. \quad (2.41)$$

A related schematic representation can be seen in figure 2.2. Due to the large prominence of the phase shifts in the presented work, it is worth to formulate the scattering solutions depending on  $\delta_l(E)$ . In order to do so, one inserts the Hankel function  $h_l^+(kr)$  in equation (2.40) and considers the large argument cases  $j_l(kr) \propto \sin(kr - l\frac{\pi}{2})/(kr)$  and  $n_l(kr) \propto -\cos(kr - l\frac{\pi}{2})/(kr)$  which lead to

$$R_l(r, E) = (1 - i k t_l(E)) \frac{\sin(kr - l\frac{\pi}{2})}{kr} - k t_l(E) \frac{\cos(kr - l\frac{\pi}{2})}{kr}. \quad (2.42)$$

Additionally, one can stress the identity  $\sin(x + y) = \sin x \cos y + \cos x \sin y$  in order to separate  $\delta_l(E)$  in equation (2.41) leading to

$$R_l(r, E) = C_l \left( \cos \delta_l(E) \frac{\sin(kr - l\frac{\pi}{2})}{kr} + \sin \delta_l(E) \frac{\cos(kr - l\frac{\pi}{2})}{kr} \right). \quad (2.43)$$

A direct comparison of equations (2.42) and (2.43) delivers  $C_l = e^{i\delta_l(E)}$  and finally gives

$$R_l(r, E) = e^{i\delta_l(E)} (\cos\delta_l(E) j_l(kr) - \sin\delta_l(E) n_l(kr)) \quad (2.44)$$

as the regular solution of the single-site scattering problem depending on the free-particle solutions perturbed by the scattering phase shifts  $\delta_l(E)$ . The consideration of  $V(r) \rightarrow 0$  and consequently  $\delta_l(E) \rightarrow 0$  in (2.44) changes  $R_l(r, E)$  to  $j_l(kr)$  and shows the plausibility of the obtained result.

The previous comparison also enables us to find an expression for the single-site scattering  $T$  matrix

$$t_l(E) = -\frac{1}{k} \sin\delta_l(E) e^{i\delta_l(E)}. \quad (2.45)$$

In order to find the irregular single-site wave function, which is important for the completeness of the solution, one can use

$$N_l(r, E) = \tilde{C}_l (\sin\delta_l(E) j_l(kr) + \cos\delta_l(E) n_l(kr)) \quad (2.46)$$

as a starting point. It is the analog of equation (2.43) with interchanged coefficients to ensure the correct behaviour in the zero-potential limit. The appropriate choice for  $\tilde{C}_l$  results from the Wronskian  $W[R_l(kr), N_l(kr)]$  which should give the same result as for the free-particle solutions in equation (2.35). It leads to  $\tilde{C}_l = e^{-i\delta_l(E)}$  and therefore

$$N_l(r, E) = e^{-i\delta_l(E)} (\sin\delta_l(E) j_l(kr) + \cos\delta_l(E) n_l(kr)) \quad (2.47)$$

is the irregular solution of the single-site scattering problem formulated in dependence on the free-particle solutions perturbed by the scattering phase shifts  $\delta_l(E)$ . The single-site scattering Green function, which is defined by

$$\left( E + \frac{\partial^2}{\partial \mathbf{r}^2} - V(r) \right) g(\mathbf{r}, \mathbf{r}'; E) = \delta(\mathbf{r} - \mathbf{r}'), \quad (2.48)$$

can be obtained by solving the radial Dyson equation according to (2.28) with the free-particle Green function as reference. The solution outside the muffin-tin radius ( $r, r' > R_{\text{MT}}$ ) is straightforward. The remaining part can be constructed by requiring continuity at  $r = R_{\text{MT}}$ . Finally, the single-site scattering Green function can be written as [55]

$$\begin{aligned} g(\mathbf{r}, \mathbf{r}'; E) &= \sum_L Y_L(\hat{\mathbf{r}}) g_l(r, r'; E) Y_L^*(\hat{\mathbf{r}}') \\ g_l(r, r'; E) &= k H_l^+(r_>, E) R_l(r_<, E) \\ H_l^+(r, E) &= \begin{cases} N_l(r, E) - i e^{-2i\delta_l(E)} R_l(r, E), & r < R_{\text{MT}} \\ h_l^+(kr) = n_l(kr) - i j_l(kr), & r > R_{\text{MT}}. \end{cases} \end{aligned} \quad (2.49)$$

The zero-potential limit with vanishing scattering phase shifts shows that the result (2.49) is consistent with the previous consideration since  $R_l(r, E)$ ,  $N_l(r, E)$ , and  $H_l^+(r, E)$  become  $j_l(kr)$ ,  $n_l(kr)$ , and  $h_l^+(kr)$ , respectively and therefore  $g(\mathbf{r}, \mathbf{r}'; E)$  turns into  $\dot{g}(\mathbf{r}, \mathbf{r}'; E)$ .

## Multiple Scattering

The consideration of the KKR approach continues with the representation of the multiple-scattering contribution. It characterizes a propagating wave that experiences several single-site scattering events described in the previous section. A suitable approach is based on a crystal potential as in equation (2.31). The used cell-centered coordinates are introduced in figure 2.3(a).

Similar to equation (2.48) the multiple-scattering Green function is defined by

$$\left(E + \frac{\partial^2}{\partial \mathbf{r}^2} - V_n(r)\right) G(\mathbf{R}^n + \mathbf{r}, \mathbf{R}^{n'} + \mathbf{r}'; E) = \delta_{nn'} \delta(\mathbf{r} - \mathbf{r}'). \quad (2.50)$$

The case  $n = n'$  delivers an inhomogeneous differential equation describing the single-site scattering Green function as in (2.48), whereas the other case  $n \neq n'$  provides the homogeneous differential equation characterizing the multiple scattering between different cell potentials. The total Green function of the full problem can be written as the general solution of the homogeneous equation and a special solution of the inhomogeneous part

$$G(\mathbf{R}^n + \mathbf{r}, \mathbf{R}^{n'} + \mathbf{r}'; E) = \delta_{nn'} g^n(\mathbf{R}^n + \mathbf{r}, \mathbf{R}^{n'} + \mathbf{r}'; E) + \sum_{L, L'} R_L^n(\mathbf{r}, E) G_{LL'}^{nn'}(E) R_{L'}^{\times n'}(\mathbf{r}', E). \quad (2.51)$$

This function is expanded into the solutions of the single-site scatterer given by equation (2.39) as

$$R_L^n(\mathbf{r}, E) = R_l^n(r, E) Y_L(\hat{\mathbf{r}}) \quad (2.52)$$

and includes the unknown expansion coefficients  $G_{LL'}^{nn'}(E)$  which are called structural constants or structural Green function since they describe the influence of the geometric structure. The complex conjugation  $\times$  acts solely on the spherical part

$$R_L^{\times n}(\mathbf{r}, E) = R_L^n(r, E) Y_L^*(\hat{\mathbf{r}}). \quad (2.53)$$

Clarity is achieved by the short form

$$G(\mathbf{R}^n + \mathbf{r}, \mathbf{R}^{n'} + \mathbf{r}'; E) = G^{nn'}(\mathbf{r}, \mathbf{r}'; E). \quad (2.54)$$

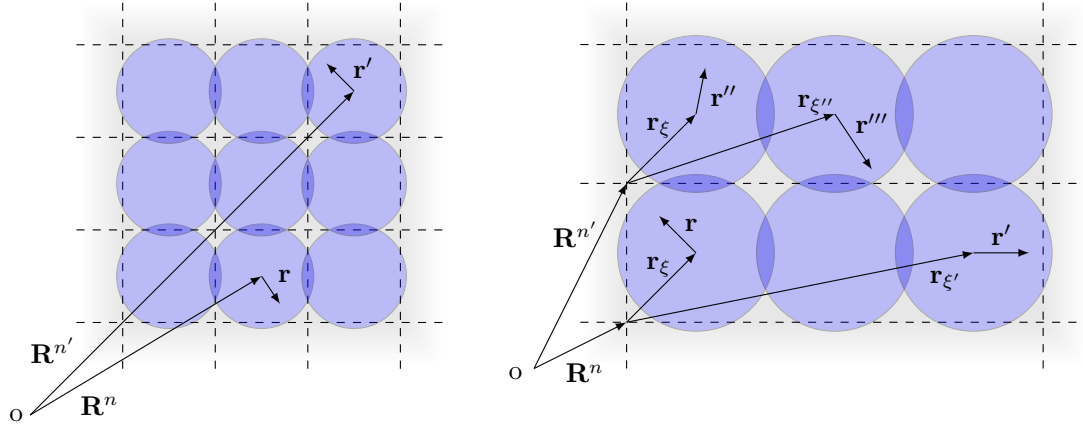
Inserting the Green function (2.51) into the Dyson equation (2.25) firstly provides terms  $\sim \delta_{nn'}$  forming the on-site Green function

$$\hat{g}^n(E) = \tilde{\hat{g}}^n(E) + \hat{g}^n(E) \Delta V^n \hat{g}^n(E) \quad (2.55)$$

where  $\Delta V$  represents the potential difference between the physical and the reference system. Secondly, it delivers the so-called algebraic Dyson equation

$$\hat{G}_{LL'}^{nn'}(E) = \tilde{\hat{G}}_{LL'}^{nn'}(E) + \sum_{n'', L''} \tilde{\hat{G}}_{LL''}^{nn''}(E) \Delta t_{L''}^{n''}(E) \hat{G}_{L''L'}^{n''n'}(E) \quad (2.56)$$

for the structural Green function which includes the difference between the single-site T-matrices of the real and the reference system,  $\Delta t_l^n(E) = t_l^n(E) - \tilde{t}_l^n(E)$ . The tilde marks quantities of a reference system which has to be specified yet.



(a) Cell-centered ASA coordinates with lattice vectors  $\mathbf{R}^n$  and  $\mathbf{R}^{n'}$  (b) Cell-centered ASA coordinates for a lattice with atomic basis with lattice vectors  $\mathbf{R}^{n_i}$  and basis vectors  $\mathbf{r}_{\xi_i}$

Figure 2.3.: Cell-centered coordinates with (a) mono-atomic basis or (b) multi-atomic basis.

For ordinary metals and simple bulk systems the mono-atomic basis is sufficient but a general description requires the transition to a multi-atomic basis depicted in figure 2.3(b). Especially for free-standing films (so-called slabs) considered in this thesis, this approach is essential. The underlying Bravais lattice is generated by the lattice vectors  $\mathbf{R}^n$ , while the atoms in the unit cell are reached by the vectors  $\mathbf{r}_{\xi}$ . Consequently, the position of the atom  $\xi$  in the unit cell  $n$  is represented by

$$\mathbf{R}_{\xi}^n = \mathbf{R}^n + \mathbf{r}_{\xi}, \quad (2.57)$$

whereas the connection vector between two arbitrary atoms is

$$\mathbf{R}_{\xi\xi'}^{nn'} = \mathbf{R}_{\xi'}^{n'} - \mathbf{R}_{\xi}^n = \mathbf{R}^{nn'} + \mathbf{r}_{\xi\xi'}. \quad (2.58)$$

The necessary transformation of equation (2.56) for this situation can be achieved by adding the atomic index  $\xi$

$$\hat{G}_{LL'}^{nn'}(E) = \hat{G}_{LL'}^{nn'}(E) + \sum_{n'', \xi'', L''} \hat{G}_{LL''}^{nn''}(E) \Delta t_{L''}^{\xi''}(E) \hat{G}_{L''L'}^{n''n'}(E), \quad (2.59)$$

where  $n$  represents the cell index now. This cell index is missing in the single-site scattering matrices due to the translational invariance of the ideal crystal potential. The system periodicity allows for an efficient calculation of the structural Green function by a Fourier transformation

$$G_{LL'}^{\xi\xi'}(\mathbf{k}, E) = \sum_{n'} e^{+i\mathbf{k}\mathbf{R}^{0n'}} \hat{G}_{LL'}^{0n'}(E) \quad (2.60)$$

with the corresponding back transformation

$$\hat{G}_{LL'}^{nn'}(E) = \frac{1}{V_{\text{BZ}}} \int_{\text{BZ}} d^d k e^{-i\mathbf{k}\mathbf{R}^{nn'}} G_{LL'}^{\xi\xi'}(\mathbf{k}, E). \quad (2.61)$$

As a reference, an arbitrary cell (here:  $n = 0$ ) can be chosen since  $\hat{G}_{LL'}^{nn'}(E)$  solely depends on the difference vector  $\mathbf{R}^{nn'}$ . The sum in (2.60) runs over all cells of the Bravais lattice while the integration in (2.61) is carried out in the (first) Brillouin zone only. The corresponding volume  $V_{\text{BZ}}$  is connected to the volume of the elementary cell in real space by  $V_{\text{EC}} = (2\pi)^d V_{\text{BZ}}^{-1}$ . The appearing  $d$  stands for the system dimension for which the Fourier transformation can be applied. In bulk systems  $d = 3$  while the free-standing films are periodic in plane only which implicates  $d = 2$ . Accordingly, it is possible to formulate the Fourier transformed algebraic Dyson equation

$$\hat{G}_{LL'}^{\xi\xi'}(\mathbf{k}, E) = \hat{G}_{LL'}^{\xi\xi'}(\mathbf{k}, E) + \sum_{\xi'', L''} \hat{G}_{LL''}^{\xi\xi''}(\mathbf{k}, E) \Delta t_{l''}^{\xi''}(E) \hat{G}_{L''L'}^{\xi''\xi'}(\mathbf{k}, E). \quad (2.62)$$

It is numerically demanding to solve equation (2.62) by direct inversion but rather advantageous [53] to use the representation

$$\hat{G}_{LL'}^{\xi\xi'}(\mathbf{k}, E) = -\delta_{LL'} \delta_{\xi\xi'} [\Delta t^{-1}(E)]_l^\xi - [\Delta t^{-1}(E)]_l^\xi [M^{-1}(\mathbf{k}, E)]_{LL'}^{\xi\xi'} [\Delta t^{-1}(E)]_{l'}^{\xi'}, \quad (2.63)$$

which includes the so-called KKR matrix

$$M_{LL'}^{\xi\xi'}(\mathbf{k}, E) = \hat{G}_{LL'}^{\xi\xi'}(\mathbf{k}, E) - \delta_{\xi\xi'} \delta_{LL'} [\Delta t^{-1}(E)]_l^\xi. \quad (2.64)$$

Equation (2.64) is the final key to solve the presented problem. The knowledge of the Green function of an appropriate reference system, which will be specified later, and the corresponding transition matrix provides the KKR matrix, which in turn yields the Fourier-transformed structural Green function via equation (2.63). Evaluating the Brillouin zone integration in (2.61) delivers the structural Green function in real space. This allows for the construction of the Green function of the ideal crystal via equation (2.51), where the on-site Green function and the regular single site scattering solution are known by the equations (2.49) and (2.40), respectively. Finally, the actually sought charge density can be calculated by equation (2.22).

## Perturbed System

The research of the extrinsic spin Hall effect requires the consideration of lattice imperfections. In particular, the present thesis examines clean host systems doped with impurities. The Bloch states of the ideal crystal

$$\begin{aligned} \psi_{\mathbf{k}}^{\nu}(\mathbf{R}_{\xi}^n + \mathbf{r}) &= \frac{1}{\sqrt{V}} \sum_L e^{i\mathbf{k}\mathbf{R}^n} \hat{c}_L^{\xi}(\mathbf{k}, \nu) \hat{R}_l^{\xi}(r, E) Y_L(\hat{\mathbf{r}}) \\ &= \frac{1}{\sqrt{V}} \sum_L \hat{c}_L^{\xi}(\mathbf{k}, \nu) \hat{R}_l^{\xi}(r, E) Y_L(\hat{\mathbf{r}}), \end{aligned} \quad (2.65)$$

which are expanded in the single-site scattering solutions and normalized with respect to the crystal volume  $V$ , serve as a suitable starting point for the investigation of the perturbed system.

Similar to the unperturbed wave function (2.65) it is possible to construct the perturbed one as

$$\psi_{\mathbf{k}}^{\nu}(\mathbf{R}_{\xi}^n + \mathbf{r}, \xi_0) = \frac{1}{\sqrt{V}} \sum_L c_L^{\xi}(\mathbf{k}, \nu, \xi_0) R_l^{\xi}(r, \xi_0, E) Y_L(\hat{\mathbf{r}}). \quad (2.66)$$

The introduced impurity breaks the system's translational invariance. Consequently, the potential perturbation depends on the cell index  $n$  as well as on the atomic index  $\xi$  now. Using once more the cell index  $n = 0$ , one investigates a finite defect cluster around the atom at  $\mathbf{R}_{\xi_0}^0$ . In metallic systems the screening of the perturbed potential is short ranged which usually allows for the restriction to the next 4 nearest neighbor shells. For the considered systems crystallizing in face-centered cubic (fcc) structure the investigated impurity cluster consists of 55 atoms.

The Lippmann-Schwinger equation connecting perturbed and unperturbed wave functions can be transformed [57] into a formulation for the expansion coefficients

$$c_L^{\xi}(\mathbf{k}, \nu, \xi_0) = \mathring{c}_L^{\xi}(\mathbf{k}, \nu) + \sum_{n', \xi', L'} G_{LL'}^{nn'}(E) \Delta t_{L'}^{\xi'}(\xi_0, E) c_{L'}^{\xi'}(\mathbf{k}, \nu, \xi_0), \quad (2.67)$$

which is formally solved by

$$c_L^{\xi}(\mathbf{k}, \nu, \xi_0) = \sum_{n', \xi', L'} D_{LL'}^{nn'}(\xi_0, E) \mathring{c}_{L'}^{\xi'}(\mathbf{k}, \nu) \quad (2.68)$$

using

$$D_{LL'}^{nn'}(\xi_0, E) = \left[ \left( 1 - \mathring{G}(E) \Delta t(\xi_0, E) \right)^{-1} \right]_{LL'}^{nn'}. \quad (2.69)$$

With the help of the algebraic Dyson equation (2.59), the employed matrix  $D$  can be expressed in terms of the known structural Green function and transition matrix

$$D_{LL'}^{\xi\xi'}(\xi_0, E) = \delta_{nn'} \delta_{\xi\xi'} \delta_{LL'} + G_{LL'}^{\xi\xi'}(\xi_0, E) \Delta t_{L'}^{\xi'}(\xi_0, E). \quad (2.70)$$

## Reference System

As often mentioned before, the free-electron case could serve as a reference system for the identification of the Green function for the ideal crystal since the corresponding solutions are known analytically. An emerging problem is the infinite sum in the Fourier transformation (2.60) which cannot be simply evaluated this way. In order to make the sum finite and ensure a good convergence, a special reference potential  $\tilde{V}$  is introduced [53, 58, 59]. It consists of repulsive muffin-tin potentials centered at the atomic lattice sites. The corresponding structural Green function can be calculated evaluating the Dyson equation (2.25) in real space with the free-particle solution as reference. The advantage of the obtained Green function is its fast exponential decay with the distance  $R^{nn'}$ . Due to this screening, the numerical evaluation of equation (2.60) can be restricted to a finite cluster around a reference atom. Finally, the screened structural constants are Fourier transformed and used to evaluate a Dyson equation in reciprocal space in order to get the structural Green function of the

investigated host system.

It is important to take into account that the reference system can introduce non-physical states in the energy interval of interest. To avoid such states, the reference potential should have a strength of at least about 4 Ry [53].

## Relativistic Formalism

The emergence of the spin Hall effect is based on the presence of spin-orbit coupling. Since this is a relativistic effect, the electronic structure needs to be determined accordingly. Again, the appropriate classification of a relativistic state is carried out in  $\kappa\mu$ -representation from equation (2.14). While the non-relativistic notation used the combined index  $L = \{l, m\}$ , we now use  $Q = \{\kappa, \mu\}$  with  $\bar{Q} = \{-\kappa, \mu\}$ . The entire investigation in this thesis is restricted to non-magnetic materials. Hence, the following formulations will cover this case only. Consequently, the Green function can be written as

$$G^{\xi\xi'}(\mathbf{r}, \mathbf{r}'; E) = \delta_{nn'}\delta_{\xi\xi'} g^\xi(\mathbf{r}, \mathbf{r}'; E) + \sum_{Q, Q'} R_Q^\xi(\mathbf{r}, E) G_{QQ'}^{\xi\xi'}(E) \left( R_{Q'}^{\xi'}(\mathbf{r}', E) \right)^\times \quad (2.71)$$

with the regular solution in dependence of the index  $Q$  following equation (2.13)

$$R_Q^\xi(\mathbf{r}, E) = \begin{pmatrix} g_Q^\xi(r) \chi_Q(\hat{\mathbf{r}}) \\ i f_Q^\xi(r) \chi_{\bar{Q}}(\hat{\mathbf{r}}) \end{pmatrix}, \quad (2.72)$$

which takes the form of a bispinor and contains the spin-angular functions from equation (2.16). The special complex conjugation firstly mentioned in equation (2.53) only acts on the non-spherical part as

$$\left( R_Q^\xi(\mathbf{r}, E) \right)^\times = \left( g_Q^\xi(r) \chi_Q^\dagger(\hat{\mathbf{r}}), -i f_Q^\xi(r) \chi_{\bar{Q}}^\dagger(\hat{\mathbf{r}}) \right). \quad (2.73)$$

The related algebraic Dyson equation

$$\hat{G}_{QQ'}^{\xi\xi'}(E) = \hat{G}_{QQ'}^{\xi\xi'}(E) + \sum_{n'', \xi'', Q''} \hat{G}_{QQ''}^{\xi\xi''}(E) \Delta t_{Q''}^{\xi''}(E) \hat{G}_{Q''Q'}^{\xi''\xi'}(E) \quad (2.74)$$

includes the matrix elements of the single-site  $T$  matrix, which can be written as

$$\begin{aligned} \Delta t_Q^\xi(E) &= \int d^3r \left( \tilde{R}_Q^\xi(\mathbf{r}, E) \right)^\dagger \Delta V^\xi(r) R_Q^\xi(\mathbf{r}, E) \\ &= \int_0^{R_{\text{ASA}}^n} r^2 dr \left[ \left( \tilde{g}_Q^\xi \right)^* g_Q^\xi + \left( \tilde{f}_Q^\xi \right)^* f_Q^\xi \right] \Delta V^\xi(r) \end{aligned} \quad (2.75)$$

in the investigated non-magnetic case. Consequently, the fundamentally important KKR matrix takes the form

$$M_{QQ'}^{\xi\xi'}(\mathbf{k}, E) = \hat{G}_{QQ'}^{\xi\xi'}(\mathbf{k}, E) - \delta_{\xi\xi'} \left[ \Delta t^{-1}(E) \right]_Q^\xi. \quad (2.76)$$

## Evaluating the Phase Shifts

The calculation of the phase shifts, introduced in the section *Single-Site Scattering*, is connected with the logarithmic derivative of the regular solution  $R_l(r, E)$

$$L_l(r, E) := \frac{\frac{dR_l(r, E)}{dr}}{R_l(r, E)} := \frac{R_l'(r, E)}{R_l(r, E)}. \quad (2.77)$$

The evaluation of equation (2.77) at the muffin-tin radius ensures continuity and differentiability of the regular solution being composed of a numerically given part inside the muffin-tin sphere and an analytically known contribution for  $r > R_{\text{MT}}$ . Considering equation (2.44) provides

$$L_l(R_{\text{MT}}, E) = \frac{j_l'(kr) - \tan \delta_l(E) n_l'(kr)}{j_l(kr) - \tan \delta_l(E) n_l(kr)} \Big|_{r=R_{\text{MT}}} \quad (2.78)$$

which finally leads to an equation for the phase shifts  $\delta_l(E)$

$$\tan \delta_l(E) = \frac{L_l^{\text{num}}(R_{\text{MT}}^-, E) j_l(kr) - j_l'(kr)}{L_l^{\text{num}}(R_{\text{MT}}^-, E) n_l(kr) - n_l'(kr)} \Big|_{r=R_{\text{MT}}} \quad (2.79)$$

for which the numerical solution inside the muffin-tin sphere is used.

The calculation of relativistic phase shifts is based on equation (2.13) which delivers the relativistic matching condition [45] for the non-magnetic case

$$\sum_{\kappa\mu} \begin{pmatrix} g_\kappa(r, E) \chi_{\kappa\mu}(\hat{\mathbf{r}}) \\ i f_\kappa(r, E) \chi_{-\kappa\mu}(\hat{\mathbf{r}}) \end{pmatrix} = \sum_{\kappa\mu} \begin{pmatrix} [\cos \delta_\kappa(E) j_l(kr) - \sin \delta_\kappa(E) n_l(kr)] \chi_{\kappa\mu}(\hat{\mathbf{r}}) \\ \frac{ikc\hbar S_\kappa}{W+m_e c^2} [\cos \delta_\kappa(E) j_{\bar{l}}(kr) - \sin \delta_\kappa(E) n_{\bar{l}}(kr)] \chi_{-\kappa\mu}(\hat{\mathbf{r}}) \end{pmatrix} \quad (2.80)$$

that needs to be fulfilled at the muffin-tin radius. According to equation (2.14) the connection between  $\kappa$  and  $l$  is given by

$$l = \begin{cases} \kappa & , \kappa > 0 \\ -\kappa - 1 & , \kappa < 0 \end{cases} \quad (2.81)$$

while  $\bar{l}$  is introduced according to

$$\bar{l} = \begin{cases} \kappa - 1 & , \kappa > 0 \\ -\kappa & , \kappa < 0 \end{cases}. \quad (2.82)$$

Here,  $S_\kappa$  represents the sign of  $\kappa$

$$S_\kappa = \text{sgn}(\kappa) = \frac{\kappa}{|\kappa|} = l - \bar{l}. \quad (2.83)$$

Consequently, the relativistic analogue to equation (2.79) reads [45]

$$\tan \delta_\kappa(E) = \frac{Q_\kappa(r, E) j_l(kr) - \frac{\hbar k c S_\kappa}{W+m_e c^2} j_{\bar{l}}(kr)}{Q_\kappa(r, E) n_l(kr) - \frac{\hbar k c S_\kappa}{W+m_e c^2} n_{\bar{l}}(kr)} \Big|_{r=R_{\text{MT}}} \quad (2.84)$$



with the abbreviation

$$Q_\kappa(r, E) = \frac{f_\kappa(r, E)}{g_\kappa(r, E)}. \quad (2.85)$$

### Fermi Surface and Fermi Velocity

In transport theory, the Fermi energy  $E_F$  plays an important role dividing the occupied from the unoccupied states. Essentially, the electrons with this energy determine the transport phenomena since they can be excited by very small energy supply. The Fermi surface is formed by all points in  $\mathbf{k}$  space where the corresponding state has an energy eigenvalue  $E_{\mathbf{k}} = E_F$ . The determination of these points is executed by a tetrahedron method, which is described explicitly in [53]. Depending on the dimension of the studied system, the irreducible part of the Brillouin zone is either filled by tetrahedra (3D) or triangles (2D). A method of nested intervals is used in order to calculate the intersections with the edges of the tetrahedra or triangles, respectively. If the applied fragmentation is dense enough, the connection of all these points provides the whole Fermi surface. In case of a two-dimensional slab, the Fermi surface takes the form of several Fermi lines, where the number of lines is connected to the related film thickness [60].

An important quantity for the investigation of the considered transport phenomena is the Fermi velocity

$$\mathbf{v}_F = \left. \frac{\partial E_{\mathbf{k}}}{\partial \mathbf{k}} \right|_{E=E_F}, \quad (2.86)$$

which is evaluated over the discussed Fermi surface. Systems with smoothly curved Fermi surfaces as the considered metals Cu, Ag, and Au can be described sufficiently by a numerical  $\mathbf{k}$  derivative. For this purpose, two additional isoenergetic surfaces with  $E^+ = E_F + \delta E$  and  $E^- = E_F - \delta E$  have to be determined, where the energy difference  $\delta E$  should be sufficiently small. The conducted calculations used  $\delta E = 10^{-7}$  Ry. For the linear interpolation, the intersections  $\mathbf{k}_i^\pm$  of the Fermi surface with the tetrahedra or triangles are used to determine the velocity by the system of linear equations

$$(\mathbf{k}_i^+ - \mathbf{k}_i^-) \mathbf{v}_F = 2 \delta E \quad \text{with} \quad i = 1, 2, (3). \quad (2.87)$$

For systems, where the Fermi surface offers regions with large curvature, this approach may not be sufficient due to numerical instabilities. Performing the derivation with respect to  $\mathbf{k}$  analytically by means of the screened KKR matrix can help to improve this issue [36].

### Spin Polarization

The discussion of the spin Hall effect requires knowledge about the spin states of the eigenfunctions. The corresponding relativistic vector spin operator [45]

$$\underline{\beta} \underline{\Sigma} = \begin{pmatrix} \underline{\sigma} & 0 \\ 0 & -\underline{\sigma} \end{pmatrix}, \quad (2.88)$$

which includes the Pauli matrices  $\boldsymbol{\sigma} = (\underline{\sigma}_x, \underline{\sigma}_y, \underline{\sigma}_z)$  from equation (2.10), does not commute with the Dirac Hamiltonian of (2.8). Hence and in contrast to the non-relativistic case, the spin is not conserved in a relativistic treatment. This means that an eigenstate does not carry spin-up or spin-down character only. Consequently, the expectation value of the above defined spin operator

$$\mathbf{s}(\mathbf{k}) = \left\langle \psi_{\mathbf{k}}^{\uparrow} \left| \underline{\beta} \boldsymbol{\Sigma} \right| \psi_{\mathbf{k}}^{\uparrow} \right\rangle \quad (2.89)$$

delivers important information about the spin mixing and is called spin polarization. Especially an evaluation on the Fermi surface is needed for a proper description of the considered transport phenomena. A crucial point in this discussion is the fact that the wave functions are twofold degenerate at every  $\mathbf{k}$  point since time and space inversion symmetry emerge in the non-magnetic systems considered here. According to reference [61], the corresponding orthonormal wave functions are labeled with  $|\psi_{\mathbf{k}}^1\rangle$  and  $|\psi_{\mathbf{k}}^2\rangle$  and have opposite spin

$$\langle \psi_{\mathbf{k}}^1 | \underline{\beta} \boldsymbol{\Sigma} | \psi_{\mathbf{k}}^1 \rangle = -\langle \psi_{\mathbf{k}}^2 | \underline{\beta} \boldsymbol{\Sigma} | \psi_{\mathbf{k}}^2 \rangle. \quad (2.90)$$

Nevertheless, at every  $\mathbf{k}$  point, the spin expectation value can point in any direction since any linear combination of the two states is an eigenstate as well. Therefore, it is useful to apply a gauge, which also gives a proper basement for the definition of spin-flip scattering. Generally, this gauge is a unitary transformation of the form

$$\begin{aligned} |\psi_{\mathbf{k}}^3\rangle &= c_1 |\psi_{\mathbf{k}}^1\rangle + c_2 |\psi_{\mathbf{k}}^2\rangle \\ |\psi_{\mathbf{k}}^4\rangle &= -c_2^* |\psi_{\mathbf{k}}^1\rangle + c_1^* |\psi_{\mathbf{k}}^2\rangle \end{aligned} \quad (2.91)$$

with

$$|c_1|^2 + |c_2|^2 = 1. \quad (2.92)$$

A very intuitive gauge is to choose a global quantization axis, for example, along  $z$  direction [61] with the conditions

$$\begin{aligned} \langle \psi_{\mathbf{k}}^3 | \underline{\beta} \sigma_x | \psi_{\mathbf{k}}^3 \rangle &= \langle \psi_{\mathbf{k}}^4 | \underline{\beta} \sigma_x | \psi_{\mathbf{k}}^4 \rangle = 0 \\ \langle \psi_{\mathbf{k}}^3 | \underline{\beta} \sigma_y | \psi_{\mathbf{k}}^3 \rangle &= \langle \psi_{\mathbf{k}}^4 | \underline{\beta} \sigma_y | \psi_{\mathbf{k}}^4 \rangle = 0 \\ \langle \psi_{\mathbf{k}}^3 | \underline{\beta} \sigma_z | \psi_{\mathbf{k}}^3 \rangle &= -\langle \psi_{\mathbf{k}}^4 | \underline{\beta} \sigma_z | \psi_{\mathbf{k}}^4 \rangle \geq 0. \end{aligned} \quad (2.93)$$

Consequently, the wave functions carry a spin expectation value parallel or antiparallel to the  $z$  direction and are labeled with  $\psi_{\mathbf{k}}^+$  and  $\psi_{\mathbf{k}}^-$ , respectively, depending on the sign of  $\mathbf{s}(\mathbf{k})$  defined by (2.89). In the non-relativistic limit, the  $|+\rangle$  and  $|-\rangle$  states coincide with the spin-up  $|\uparrow\rangle$  and spin-down  $|\downarrow\rangle$  states. The exact form of the parameters  $c_1$  and  $c_2$  that fulfill the conditions (2.93) is not important for a general understanding of the concept but can be found in the appendix of reference [61]. Problems of this gauge occur for so-called spin hot spots [62] with a vanishing spin

polarization. An alternative gauge [63] solving this problem requires the conditions

$$\begin{aligned}\langle \psi_{\mathbf{k}}^3 | \underline{\beta} \sigma_z | \psi_{\mathbf{k}}^4 \rangle &= 0 \\ \langle \psi_{\mathbf{k}}^3 | \underline{\beta} \sigma_z | \psi_{\mathbf{k}}^3 \rangle &= -\langle \psi_{\mathbf{k}}^4 | \underline{\beta} \sigma_z | \psi_{\mathbf{k}}^4 \rangle \geq 0.\end{aligned}\tag{2.94}$$

The essence of this gauge is that finite  $x$  and  $y$  components  $\langle \psi_{\mathbf{k}}^+ | \underline{\beta} \sigma_x | \psi_{\mathbf{k}}^+ \rangle = -\langle \psi_{\mathbf{k}}^- | \underline{\beta} \sigma_x | \psi_{\mathbf{k}}^- \rangle$  and  $\langle \psi_{\mathbf{k}}^+ | \underline{\beta} \sigma_y | \psi_{\mathbf{k}}^+ \rangle = -\langle \psi_{\mathbf{k}}^- | \underline{\beta} \sigma_y | \psi_{\mathbf{k}}^- \rangle$  can appear but  $\langle \psi_{\mathbf{k}}^+ | \underline{\beta} \sigma_z | \psi_{\mathbf{k}}^+ \rangle$  takes its maximal value with respect to all possible gauges [63].

The results obtained in this work rely on the second gauge presented. For the investigated systems, the influence of the chosen gauge is rather small (see appendix A) but for certain systems with avoided crossing near the Fermi surface the choice could have more influence [63].

## 2.2. Semiclassical Electronic Transport

### 2.2.1. Boltzmann Equation

The description of transport phenomena is closely related to the definition of the corresponding currents flowing in the system. Within the semiclassical approach, the electric current density is given by

$$\mathbf{j} = -\frac{e}{V} \sum_{\mathbf{k}} \mathbf{v}_{\mathbf{k}} f_{\mathbf{k}}. \quad (2.95)$$

The electrons contribute to it with their charge  $-e$  (note:  $e > 0$ ) and the group velocity

$$\mathbf{v}_{\mathbf{k}} = \frac{1}{\hbar} \frac{\partial E_{\mathbf{k}}}{\partial \mathbf{k}}. \quad (2.96)$$

The quantity  $f_{\mathbf{k}}$  is the so-called distribution function which represents the density of electrons in state  $\mathbf{k}$  with space coordinate  $\mathbf{r}$  at time  $t$  as  $f(\mathbf{r}, \mathbf{k}, t)$ . It is advantageous to investigate this function since it circumvents the analysis of equations of motion in  $6N$  dimensional phase space for each of the  $N$  electrons. The chosen semiclassical ansatz to describe the changes of the distribution function is the Boltzmann equation [41, 64, 65]

$$\dot{\mathbf{r}} \frac{\partial f}{\partial \mathbf{r}} + \dot{\mathbf{k}} \frac{\partial f}{\partial \mathbf{k}} + \frac{\partial f}{\partial t} = \left( \frac{\partial f}{\partial t} \right)_{\text{scatt}}. \quad (2.97)$$

In particular, it takes into account changes of the distribution function in consequence of diffusion, external fields and an explicit time dependence which in sum are compensated by the change due to occurring scattering processes leading to a system in a steady state. The quantity  $\dot{\mathbf{r}}$  is the group velocity from equation (2.96) while the force term reads

$$\dot{\mathbf{k}} = -\frac{e}{\hbar} \mathbf{E} \quad (2.98)$$

in the investigated case of an applied static electric field  $\mathbf{E}$  and absence of any magnetic fields. In the used approach, the distribution function is divided in its equilibrium and a non-equilibrium part

$$f(\mathbf{r}, \mathbf{k}) = \overset{\circ}{f}(\mathbf{r}, \mathbf{k}) + g(\mathbf{r}, \mathbf{k}) = \frac{1}{e^{\frac{E_{\mathbf{k}} - \mu}{k_B T}} + 1} + g(\mathbf{r}, \mathbf{k}) \quad (2.99)$$

where the former one is given by the Fermi-Dirac distribution function. Introducing equations (2.96), (2.98), and (2.99) into (2.97) leads to the linearized form

$$-e \mathbf{v}_{\mathbf{k}} \cdot \mathbf{E} \frac{\partial \overset{\circ}{f}_{\mathbf{k}}}{\partial E_{\mathbf{k}}} = \left( \frac{\partial f_{\mathbf{k}}}{\partial t} \right)_{\text{scatt}} \quad (2.100)$$

if one considers a homogeneous system and neglects higher order terms in the electric field. Further derivations require an ansatz for the scattering term. An appropriate

approach is given by a connection to the scattering probability [66] via

$$\left(\frac{\partial f_{\mathbf{k}}}{\partial t}\right)_{\text{scatt}} = \sum_{\mathbf{k}'} (P_{\mathbf{k}'\mathbf{k}} g_{\mathbf{k}'} - P_{\mathbf{k}\mathbf{k}'} g_{\mathbf{k}}) \quad (2.101)$$

disregarding the electron-electron interaction [22]. This expression reveals being intuitive considering the following. The first term on the right-hand side of equation (2.101) describes the scattering from an initial state  $\mathbf{k}'$  into a final state  $\mathbf{k}$  which appears with a probability of  $P_{\mathbf{k}'\mathbf{k}} \equiv P_{\mathbf{k}' \rightarrow \mathbf{k}}$ . The second term represents the opposite process with scattering events from an initial state  $\mathbf{k}$  into a final state  $\mathbf{k}'$  appearing with a probability  $P_{\mathbf{k}\mathbf{k}'}$ . This is not equal to  $P_{\mathbf{k}'\mathbf{k}}$  since the conventional microscopic reversibility is not valid in the presence of SOC. In consequence of this approach, the first term on the right-hand side of equation (2.101) is called scattering-in term, whereas the other one is the so-called scattering-out term. The emerging difference of the distribution function from its equilibrium value represented by  $g_{\mathbf{k}}$  can be estimated by the following ansatz. In linear response, the application of an external electric field  $\mathbf{E}$  changes the electron energy by

$$\Delta E = -e \mathbf{E} \cdot \mathbf{\Lambda}_{\mathbf{k}} \quad (2.102)$$

on its mean free path  $\mathbf{\Lambda}_{\mathbf{k}}$  between two scattering events. Perturbing the Fermi-Dirac distribution function  $f(\mathbf{r}, \mathbf{k})$  by this energy difference and expanding the resulting function in a Taylor expansion up to the term linear in  $\mathbf{E}$  leads to

$$g_{\mathbf{k}} = e \mathbf{\Lambda}_{\mathbf{k}} \cdot \mathbf{E} \left( \frac{\partial \dot{f}_{\mathbf{k}}}{\partial E_{\mathbf{k}}} \right). \quad (2.103)$$

The combination of equations (2.100), (2.101), and (2.103) results in the following form of the linearized Boltzmann equation

$$\mathbf{\Lambda}_{\mathbf{k}}^{\nu} = \tau_{\mathbf{k}}^{\nu} \left( \mathbf{v}_{\mathbf{k}}^{\nu} + \sum_{\mathbf{k}'\nu'} P_{\mathbf{k}'\mathbf{k}}^{\nu\nu'} \mathbf{\Lambda}_{\mathbf{k}'}^{\nu'} \right), \quad (2.104)$$

which is actually solved iteratively [65] and utilized for the *ab initio* results presented in sections 3.1 and 3.2. Previously, the band index was omitted for simplicity and is incorporated by  $\nu$  now. The integral equation for the vector mean free path can be written in this form since the momentum relaxation time  $\tau_{\mathbf{k}}^{\nu}$  is connected to the scattering probability via

$$(\tau_{\mathbf{k}}^{\nu})^{-1} = \sum_{\mathbf{k}'\nu'} P_{\mathbf{k}\mathbf{k}'}^{\nu\nu'}. \quad (2.105)$$

In the dilute limit of impurity concentration, which non-interacting scattering centers, Fermi's golden rule [65]

$$P_{\mathbf{k}\mathbf{k}'}^{\nu\nu'} = \frac{2\pi}{\hbar} c_0 N |T_{\mathbf{k}\mathbf{k}'}^{\nu\nu'}|^2 \delta(E_{\mathbf{k}}^{\nu} - E_{\mathbf{k}'}^{\nu'}) \quad (2.106)$$

delivers the remaining suitable representation for the microscopic transition probability. Thus, equations (2.104) - (2.106) provide the connection between the mean

free path as classical quantity and the quantum mechanical transition operator from equation (2.26) in matrix representation. Thus, the used approach is called *semi-classical*. In equation (2.106),  $c_0$  represents the impurity concentration, while  $c_0 N$  can be understood as the system's total number of defects. The energy-dependent Dirac delta function covers the incorporated issue of elastic scattering. The following section deals with two different ways to express the  $T$  matrix, either depending on quantum mechanical wave functions or in terms of scattering phase shifts.

### 2.2.2. Transition Matrix

The results for transport properties presented in this thesis are based on two concepts depending on the way the scattering information is stored in the transition matrix.

On the one hand, the expression for the  $T$  matrix via perturbed and unperturbed wave functions, which are based on the quantum mechanical *ab initio* approach, are used. Its advantageous completeness of scattering information is countered by the computationally very demanding handling. Results using this approach are presented in section 3.1 and references [H1, H5].

On the other hand, it is possible to express the transition matrix in terms of scattering phase shifts obtained from *ab initio* calculations for an impurity atom embedded in the host. The handling of this phase shift approach turns out to be quite simple but is not suitable for an arbitrary kind of host system, as extensively discussed in reference [H4]. Corresponding results are presented in sections 3.2 and 3.3 and references [H2, H3, H4].

#### Transition Matrix for *Ab Initio* Calculations

The transition matrix, the representation of the transition operator of equation (2.26) in terms of wave functions, is given by [55]

$$T_{\mathbf{k}\mathbf{k}'}^{\nu\nu'} = \sum_{n,\xi} \int d^3r \psi_{\mathbf{k}',\nu'}^{\dagger}(\mathbf{R}_\xi^n + \mathbf{r}) \Delta V_\xi^n(r, \xi_0) \psi_{\mathbf{k},\nu}(\mathbf{R}_\xi^n + \mathbf{r}, \xi_0) \quad (2.107)$$

and used for the *ab initio* calculations. Using the perturbed and unperturbed wave functions expanded in radial solutions, as shown in equations (2.65) and (2.66), leads to

$$T_{\mathbf{k}\mathbf{k}'}^{\nu\nu'} = \frac{1}{V} \sum_{n,\xi,Q} \left( \hat{c}_Q^\xi(\mathbf{k}', \nu') \right)^* \Delta_Q^\xi(\xi_0, E) c_Q^\xi(\mathbf{k}, \nu, \xi_0). \quad (2.108)$$

In equation (2.108),  $\Delta_Q^\xi$  abbreviates the integral over the scattering potential and the perturbed as well as the unperturbed radial solutions

$$\Delta_Q^\xi(\xi_0, E) = \int_0^{S_\xi^n} r^2 dr \left( \hat{R}_Q^\xi(r, E) \right)^* \Delta V_\xi^n(r, \xi_0) R_Q^\xi(r, \xi_0, E) \quad (2.109)$$

which is evaluated up to the sphere radius  $S$  of the potential perturbation at  $\mathbf{R}_\xi^n$ . The consideration of the relation between the perturbed and unperturbed wave function in equation (2.68) allows for a  $T$  matrix representation solely depending on unperturbed expansion coefficients

$$T_{\mathbf{k}\mathbf{k}'}^{\nu\nu'} = \frac{1}{V} \sum_{n,\xi,Q} \sum_{n',\xi',Q'} \left( \hat{c}_Q^\xi(\mathbf{k}', \nu') \right)^* \Delta_Q^\xi(\xi_0, E) D_{QQ'}^{\xi\xi'}(\xi_0, E) \hat{c}_{Q'}^{\xi'}(\mathbf{k}, \nu), \quad (2.110)$$

which is quite suitable for practical calculations, where  $D_{QQ'}^{\xi\xi'}(\xi_0, E)$  is defined by equation (2.70).

### Transition Matrix for Non-Relativistic Phase Shift Model

A convenient starting point for a formulation of the transition matrix in terms of non-relativistic phase shifts is the scattering amplitude  $f_{\mathbf{k}\mathbf{k}'}$  appearing in the wave function's representation as a superposition of an incoming plane wave and an outgoing spherical wave

$$\psi(\mathbf{r}) = e^{i\mathbf{k}\cdot\mathbf{r}} + f_{\mathbf{k}\mathbf{k}'} \frac{e^{ikr}}{r}. \quad (2.111)$$

According to equation (28) of reference [67], the scattering amplitude for the spin-conserved scattering process  $\mathbf{k} \rightarrow \mathbf{k}'$  can be written as

$$f_{\mathbf{k}\mathbf{k}'} = \frac{2\pi}{ik_F} \sum_{lm} [e^{2i\eta_l^m} - 1] \left( Y_l^m(\hat{\mathbf{k}}) \right)^* Y_l^m(\hat{\mathbf{k}}') = \frac{4\pi}{k_F} \sum_{lm} \sin \eta_l^m e^{i\eta_l^m} \left( Y_l^m(\hat{\mathbf{k}}) \right)^* Y_l^m(\hat{\mathbf{k}}'), \quad (2.112)$$

with  $\eta_l^m \approx \eta_l - \frac{m}{2} \frac{\lambda_l}{\Delta_l} \sin^2 \eta_l$  (considering spin-up states with spin value  $\sigma = +1$ ). Here, the phase shift's  $m$  dependence is taken into account by a series expansion in  $\frac{\lambda_l}{\Delta_l}$  [68] where  $\Delta_l$  is half of the resonance width and  $\lambda_l$  represents the SOC constant for the corresponding  $l > 0$  impurity level.

The connection between the scattering amplitude and the transition matrix is given by [56]

$$T_{\mathbf{k}\mathbf{k}'} = -\frac{2\pi\hbar^2}{m_e V} f_{\mathbf{k}\mathbf{k}'}. \quad (2.113)$$

Consequently and in accordance with reference [38], the transition matrix for spin-conserving scattering of spin-up states can be written as [H3]

$$T_{\mathbf{k}\mathbf{k}'}^{++} = \frac{4\pi^2\hbar^2}{m_e k_F V} \sum_{lm} \left[ m \frac{\lambda_l}{\Delta_l} e^{i2\eta_l} \sin^2 \eta_l - 2e^{i\eta_l} \sin \eta_l \right] \left( Y_l^m(\hat{\mathbf{k}}) \right)^* Y_l^m(\hat{\mathbf{k}}'). \quad (2.114)$$

### Transition Matrix for Relativistic Phase Shift Model

In order to express the transition matrix in terms of relativistic scattering phase shifts corresponding to  $j = l \pm \frac{1}{2}$ , again the scattering amplitude serves as a suitable

Table 2.1.: The Clebsch-Gordan coefficients  $C(l\frac{1}{2}j; m - m_s, m_s)$  according to reference [45].

$j$	$m_s = -\frac{1}{2}$	$m_s = \frac{1}{2}$
$l - \frac{1}{2}$	$\sqrt{\frac{l+m+\frac{1}{2}}{2l+1}}$	$-\sqrt{\frac{l-m+\frac{1}{2}}{2l+1}}$
$l + \frac{1}{2}$	$\sqrt{\frac{l-m+\frac{1}{2}}{2l+1}}$	$\sqrt{\frac{l+m+\frac{1}{2}}{2l+1}}$

starting point. An appropriate expression for spin-conserving scattering can be obtained in the style of equation (11.72) of reference [45] as

$$f_{\mathbf{k}\mathbf{k}'}^{+++} = \frac{4\pi}{k_F} \sum_j \sum_{m_j=-j}^j \left[ C\left(l\frac{1}{2}j; m_j - \frac{1}{2}, \frac{1}{2}\right) \right]^2 e^{i\delta_j} \sin \delta_j \left( Y_l^{m_j - \frac{1}{2}}(\hat{\mathbf{k}}) \right)^* Y_l^{m_j - \frac{1}{2}}(\hat{\mathbf{k}}'). \quad (2.115)$$

The expansion into spherical harmonics is realized by Clebsch-Gordan coefficients  $C(l\frac{1}{2}j; m - m_s, m_s)$  according to table 2.1. The application of equation (2.113) finally leads to [H2]

$$T_{\mathbf{k}\mathbf{k}'}^{+++} = -\frac{8\pi^2 \hbar^2}{m_e k_F V} \sum_{lm} \left( Y_l^m(\hat{\mathbf{k}}) \right)^* Y_l^m(\hat{\mathbf{k}}') \times \left[ \left( \frac{l+m+1}{2l+1} \right) e^{i\delta_{l+\frac{1}{2}}} \sin \delta_{l+\frac{1}{2}} + \left( \frac{l-m}{2l+1} \right) e^{i\delta_{l-\frac{1}{2}}} \sin \delta_{l-\frac{1}{2}} \right]. \quad (2.116)$$

Accordingly, it is possible to start from

$$f_{\mathbf{k}\mathbf{k}'}^{+-} = \frac{4\pi}{k_F} \sum_j \sum_{m_j=-j}^j \left( Y_l^{m_j - \frac{1}{2}}(\hat{\mathbf{k}}) \right)^* Y_l^{m_j + \frac{1}{2}}(\hat{\mathbf{k}}') \times C\left(l\frac{1}{2}j; m_j - \frac{1}{2}, \frac{1}{2}\right) e^{i\delta_j} \sin \delta_j C\left(l\frac{1}{2}j; m_j + \frac{1}{2}, \frac{1}{2}\right). \quad (2.117)$$

for the spin-flip case which finally leads to

$$T_{\mathbf{k}\mathbf{k}'}^{+-} = -\frac{8\pi^2 \hbar^2}{m_e k_F V} \sum_{lm} \left( Y_l^m(\hat{\mathbf{k}}) \right)^* Y_l^{m+1}(\hat{\mathbf{k}}') \frac{\sqrt{(l-m)(l+m+1)}}{2l+1} \times \left[ e^{i\delta_{l+\frac{1}{2}}} \sin \delta_{l+\frac{1}{2}} - e^{i\delta_{l-\frac{1}{2}}} \sin \delta_{l-\frac{1}{2}} \right]. \quad (2.118)$$



## 2.3. Contributions to the Spin Hall Effect

This section is devoted to a closer look at the single contributions to the spin Hall effect. While the introduction provided just a brief overview of the contributing mechanisms, this shall be intensified now. Especially the way how these mechanisms can be connected to the above introduced quantities will be of interest. For the SHE, the underlying mechanisms are the same as for the anomalous Hall effect, for which they are discussed much more intensively in literature [22, 29, 69].

A discussion according to a fundamental separation of corresponding contributions can start with the electric current density from equation (2.95). Beyond the group velocity (2.96), which I will denote as  $\mathbf{v}_{\mathbf{k}}^g$  in the following, the electron velocity also contains anomalous components  $\tilde{\mathbf{v}}_{\mathbf{k}}^a$ , where the tilde represents the fact that several of such anomalous terms exist. According to equation (2.99), the distribution function consists of an equilibrium and a non-equilibrium part. Consequently, it is possible to write

$$\begin{aligned} j_y^s &= -\frac{e}{V} \sum_{\mathbf{k}} s_{\mathbf{k},z} \left( v_{\mathbf{k},y}^g + \tilde{v}_{\mathbf{k},y}^a \right) \left( \dot{f}_{\mathbf{k}} + g_{\mathbf{k}} \right) \\ &= -\frac{e}{V} \sum_{\mathbf{k}} s_{\mathbf{k},z} \left[ v_{\mathbf{k},y}^g \dot{f}_{\mathbf{k}} + \tilde{v}_{\mathbf{k},y}^a \dot{f}_{\mathbf{k}} + v_{\mathbf{k},y}^g g_{\mathbf{k}} + \tilde{v}_{\mathbf{k},y}^a g_{\mathbf{k}} \right] \end{aligned} \quad (2.119)$$

for the transverse component of the spin current density in a system with applied electric field along  $x$  direction and spin quantization axis in  $z$  direction. The first term on the right hand side of equation (2.119) vanishes due to the symmetries  $\mathbf{v}_{\mathbf{k}}^g = -\mathbf{v}_{-\mathbf{k}}^g$  for the group velocity and  $\dot{f}_{\mathbf{k}} = \dot{f}_{-\mathbf{k}}$  for the Fermi-Dirac distribution function. The second term will be related to the *intrinsic* contribution, while the last two terms emerge in perturbed systems, which becomes evident due to the appearance of the non-equilibrium distribution function  $g_{\mathbf{k}}$ . The third term will be identified with the so-called *skew-scattering* contribution, whereas the fourth term will be related to the *side-jump* mechanism [29].

### 2.3.1. Intrinsic Contribution

The intrinsic contribution, clearly formulated for the AHE by Karplus and Luttinger [23], shows up via an anomalous velocity transverse to the electric field [29]

$$\mathbf{v}_{\mathbf{k}}^{a,\nu} = \frac{e}{\hbar} \mathbf{E} \times \boldsymbol{\Omega}_{\mathbf{k}}^{\nu}. \quad (2.120)$$

Here,  $\boldsymbol{\Omega}_{\mathbf{k}}^{\nu}$  is the so-called Berry curvature [70] which arises out of the periodic part  $u_{\mathbf{k}}(\mathbf{r})$  of the Bloch wave  $\psi_{\mathbf{k}}^{\nu} = u_{\mathbf{k}}^{\nu}(\mathbf{r})e^{i\mathbf{k}\cdot\mathbf{r}}$  and can be obtained as

$$\boldsymbol{\Omega}_{\mathbf{k}}^{\nu} = i \int_{V_{\text{EC}}} d^3r \nabla_{\mathbf{k}} (u_{\mathbf{k}}^{\nu}(\mathbf{r}))^* \times \nabla_{\mathbf{k}} u_{\mathbf{k}}^{\nu}(\mathbf{r}) = i \langle \nabla_{\mathbf{k}} u_{\mathbf{k}}^{\nu} | \times | \nabla_{\mathbf{k}} u_{\mathbf{k}}^{\nu} \rangle. \quad (2.121)$$

For the evaluation of equation (2.121), the completeness relation  $\sum_{\nu'} |u_{\mathbf{k}}^{\nu'}\rangle \langle u_{\mathbf{k}}^{\nu'}| = \mathbb{1}$  between all bands of the system needs to be taken into account. Additionally, the

identity

$$\langle \nabla_{\mathbf{k}} u_{\mathbf{k}}^{\nu} | u_{\mathbf{k}}^{\nu'} \rangle = \frac{\langle u_{\mathbf{k}}^{\nu} | \nabla_{\mathbf{k}} H(\mathbf{k}) | u_{\mathbf{k}}^{\nu'} \rangle}{E_{\mathbf{k}}^{\nu} - E_{\mathbf{k}}^{\nu'}}, \quad (2.122)$$

according to Schrödinger's equation (2.1), is needed. Combining the above equations finally leads to a representation of the Berry curvature

$$\Omega_{\mathbf{k}}^{\nu} = i \sum_{\nu' \neq \nu} \frac{\langle u_{\mathbf{k}}^{\nu} | \nabla_{\mathbf{k}} H(\mathbf{k}) | u_{\mathbf{k}}^{\nu'} \rangle \times \langle u_{\mathbf{k}}^{\nu'} | \nabla_{\mathbf{k}} H(\mathbf{k}) | u_{\mathbf{k}}^{\nu} \rangle}{(E_{\mathbf{k}}^{\nu} - E_{\mathbf{k}}^{\nu'})^2} \quad (2.123)$$

which supports its physical interpretation. In particular, it incorporates the influences of all bands of the system by so-called virtual interband transitions when the theoretical treatment is based on an effective one-band model. Especially for  $\mathbf{k}$  points where another band comes close to the considered one, the absolute value of the Berry curvature becomes large. In presence of degenerate bands, the Berry curvature cannot be treated in its Abelian form considered above but needs to be expressed in a non-Abelian way [71, 72]. For a twofold degenerate band, the curvature is not a vector anymore but becomes a vector-valued matrix  $\Omega_{ij}(\mathbf{k})$  instead. Since this thesis is rather focused on the spin-dependent transport than the mathematical and computational treatment of the Berry curvature, interested readers are referred to the paper of Gradhand et al. [72], which treats these points in detail.

In order to find the intrinsic contribution to the current density, one has to combine equation (2.120) with the corresponding term of equation (2.119), which leads to

$$\mathbf{j}^{\text{intr}} = -\frac{e^2}{\hbar V} \sum_{\mathbf{k}, \nu} (\mathbf{E} \times \Omega_{\mathbf{k}}^{\nu}) f_{\mathbf{k}}^{\nu}. \quad (2.124)$$

Further derivations use that the sum over  $\mathbf{k}$  can be written in an integral form according to  $\sum_{\mathbf{k}} \rightarrow \frac{V}{(2\pi)^3} \int d^3k$ , where the volume element can be reformulated as  $d^3k = dS dk_{\perp}$  and  $dk_{\perp} = \frac{1}{\hbar} \frac{dE_{\mathbf{k}}^{\nu}}{|\mathbf{v}_{\mathbf{k}}^{\nu}|}$  holds. Using Ohm's law (1.4) and assuming a spin polarization in  $z$  direction according to [72, 73] one can obtain the Hall component of the conductivity tensor due to the intrinsic mechanism by integrations over the Berry curvature as

$$\sigma_{yx}^z = \frac{e^2}{\hbar(2\pi)^3} \int_{E_F}^{\infty} dE \Omega_z(E) \quad (2.125)$$

with

$$\Omega_z(E) = \sum_{\nu} \oint_{\text{IS}(E)} \frac{d^2k}{\hbar |\mathbf{v}_F^{\nu}(\mathbf{k})|} s_z(\mathbf{k}) \Omega_z^{\nu}(\mathbf{k}). \quad (2.126)$$

Thus, a numerical calculation of the intrinsic spin Hall conductivity requires two steps. Firstly, for several densely distributed energies on a quite large energy interval, the  $\mathbf{k}$ -dependent Berry curvature needs to be evaluated and integrated over the respective iso-surface  $\text{IS}(E)$  which possibly consists of several bands  $\nu$ . The subsequent integration process for this energy-resolved Berry curvature ranges from the band energy bottom up to the Fermi level and finally provides the intrinsic spin Hall conductivity (SHC).

The actual problem occurring during this procedure is the Brillouin-zone integra-

tion of the Berry curvature [72, 74, 75]. Precisely, the computational demanding issue is related to the fact that  $\mathbf{\Omega}(\mathbf{k})$  is a very spiky function. The most problematic regions are those around avoided crossings which often arise due to spin-orbit coupling. Especially for light elements with a weak SOC, the Berry curvature around avoided crossings behaves similarly to a  $\delta$  function, whereas it is smeared for heavy elements. Hence, it is easier to calculate the intrinsic contribution to the SHE for crystals composed of heavy elements like gold or platinum than for lighter ones such as copper.

### 2.3.2. Extrinsic Contributions

In contrast to the previously investigated intrinsic contribution to the SHE, which is solely determined by the electronic band structure of the ideal host material and is independent of any scattering processes, the so-called extrinsic mechanisms arise from such scattering events caused by imperfections of the otherwise translationally invariant crystal. In the present work, substitutional impurities play the role of these defects.

In order to derive a general expression for the spin Hall conductivity arising from extrinsic mechanisms, one can start from the current density

$$\mathbf{j} = -\frac{e}{V} \sum_{\mathbf{k}} \mathbf{v}_{\mathbf{k}} g_{\mathbf{k}} \quad (2.127)$$

which can be written as

$$\mathbf{j} = -\frac{e^2}{V} \sum_{\mathbf{k}} \left( \frac{\partial \dot{f}_{\mathbf{k}}}{\partial E_{\mathbf{k}}} \right) \mathbf{v}_{\mathbf{k}} (\mathbf{\Lambda}_{\mathbf{k}} \cdot \mathbf{E}) \quad (2.128)$$

with the help of equation (2.103). Here,  $\mathbf{v}_{\mathbf{k}}$  represents a velocity that has to be specified when the final formula is employed. According to equation (2.119) it is the group velocity for skew scattering and an anomalous velocity in case of side jump (SJ). A transformation into a form including a dyadic product as well as a comparison with Ohm's law reveals an expression for the conductivity tensor

$$\underline{\sigma} = \frac{e^2}{V} \sum_{\mathbf{k}} \left( -\frac{\partial \dot{f}_{\mathbf{k}}}{\partial E_{\mathbf{k}}} \right) \mathbf{v}_{\mathbf{k}} \circ \mathbf{\Lambda}_{\mathbf{k}} \quad (2.129)$$

which includes the necessary information to quantify the spin Hall effect. The derivative of the incorporated Fermi-Dirac distribution function at  $T = 0$  is a negative  $\delta$  function in energy. Hence, the conductivity tensor takes the form

$$\underline{\sigma} = \frac{e^2}{(2\pi)^3} \int d^3k \delta(E_{\mathbf{k}} - E_F) \mathbf{v}_{\mathbf{k}} \circ \mathbf{\Lambda}_{\mathbf{k}}. \quad (2.130)$$

The appearance of the energy  $\delta$  function implying elastic scattering restricts the integral to the Fermi surface. The reformulation of the volume integral similar to

the case of the intrinsic contribution finally leads to

$$\underline{\sigma} = \frac{e^2}{\hbar(2\pi)^3} \sum_{\nu} \oint_{E_{\mathbf{k}}=E_F} \frac{dS_{\nu}}{|\mathbf{v}_{\mathbf{k}}^{\nu}|} \mathbf{v}_{\mathbf{k}}^{\nu} \circ \mathbf{\Lambda}_{\mathbf{k}}^{\nu}, \quad (2.131)$$

where  $\nu$  sums over all bands appearing at the Fermi energy. While for bulk systems exactly equation (2.131) can be utilized, the likewise considered free-standing films are treated as two-dimensional systems and need to be discussed differently. As outlined in references [60, H1], the corresponding Fermi surfaces are formed by separate Fermi lines. Accordingly, the surface integration resolves into a line integration which leads to

$$\underline{\sigma}^{2D} = \frac{e^2}{\hbar(2\pi)^2 d} \sum_{\nu} \oint_{E_{\mathbf{k}}=E_F} \frac{dl_{\nu}}{|\mathbf{v}_{\mathbf{k}}^{\nu}|} \mathbf{v}_{\mathbf{k}}^{\nu} \circ \mathbf{\Lambda}_{\mathbf{k}}^{\nu}. \quad (2.132)$$

One has to pay attention that the transformation of a two-dimensional  $\mathbf{k}$  sum into an integration is given by  $\sum_{\mathbf{k}} \rightarrow \frac{A}{(2\pi)^2} \int d^2k$  where  $A$  is the system's surface area. Consequently, the film thickness  $d$  remains in the final formula (2.132).

The proper description of spin transport phenomena requires inclusion of information about the electron spin states. Within the semiclassical approach, the spin polarization from equation (2.89) can be simply included in the conductivity tensors (2.131) and (2.132) which leads to the so-called spin-conductivity tensors for three and two dimensions

$$\underline{\sigma}^{s,3D} = \frac{e^2}{\hbar(2\pi)^3} \sum_{\nu} \oint_{E_{\mathbf{k}}=E_F} \frac{dS_{\nu}}{|\mathbf{v}_{\mathbf{k}}^{\nu}|} s_z^{\nu}(\mathbf{k}) \mathbf{v}_{\mathbf{k}}^{\nu} \circ \mathbf{\Lambda}_{\mathbf{k}}^{\nu} \quad (2.133)$$

and

$$\underline{\sigma}^{s,2D} = \frac{e^2}{\hbar(2\pi)^2 d} \sum_{\nu} \oint_{E_{\mathbf{k}}=E_F} \frac{dl_{\nu}}{|\mathbf{v}_{\mathbf{k}}^{\nu}|} s_z^{\nu}(\mathbf{k}) \mathbf{v}_{\mathbf{k}}^{\nu} \circ \mathbf{\Lambda}_{\mathbf{k}}^{\nu}, \quad (2.134)$$

respectively. These equations provide explicit expressions for the description of the extrinsic spin Hall mechanisms when the corresponding electron velocities are used and the mean free path, for which equation (2.104) can be applied, is known. In the following, the physical interpretation of these mechanisms will be discussed.

Firstly, the scattering angle between the incoming and outgoing direction (compare figures 1.3 and 2.4) is different for spin-up and spin-down electrons which is ascribed to skew scattering [25]. Equation (2.104) is closely related to the microscopic interpretation of this mechanism. Due to occurring scattering events, the transition probability is apparently nonzero. Consequently, the scattering-in term of equation (2.104), including  $P_{\mathbf{k}'\mathbf{k}}^{\nu'\nu}$ , rotates  $\mathbf{\Lambda}_{\mathbf{k}}^{\nu}$  which results in a certain scattering angle. The crux of the matter is that in presence of spin-orbit interaction, the conventional (non-relativistic) microscopic reversibility ( $P_{\mathbf{k}\mathbf{k}'}^{\nu\nu'} = P_{\mathbf{k}'\mathbf{k}}^{\nu'\nu}$ ) is not valid. Taking additionally into account that for non-magnetic systems with inversion symmetry ( $\hat{i}$ ) the time-reversal symmetry ( $\hat{t}$ ) influences the transition probability as

$$P_{\mathbf{k}\mathbf{k}'}^{\uparrow\uparrow} \stackrel{\hat{i}}{=} P_{-\mathbf{k}-\mathbf{k}'}^{\uparrow\uparrow} \stackrel{\hat{t}}{=} P_{\mathbf{k}'\mathbf{k}}^{\downarrow\downarrow} \neq P_{\mathbf{k}\mathbf{k}'}^{\downarrow\downarrow}, \quad (2.135)$$

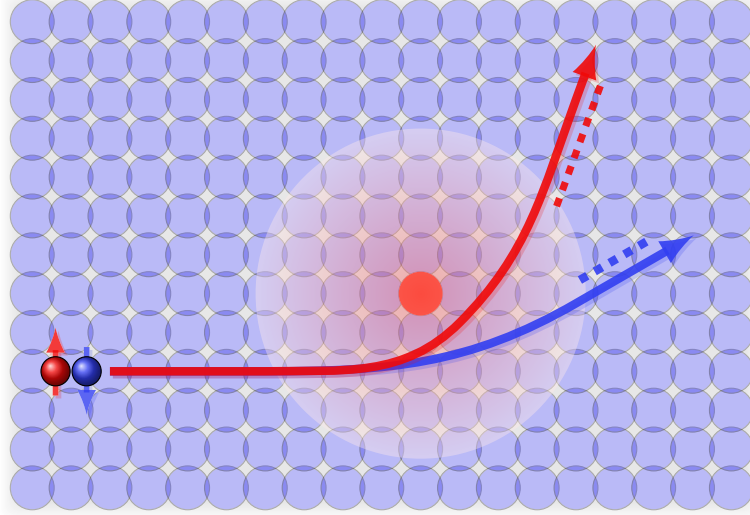


Figure 2.4.: Classical electron trajectories schematically illustrate the extrinsic contributions to the spin Hall effect due to spin-dependent scattering at an attractive impurity potential. In contrast to figure 1.3, the incident direction and the impurity center are not aligned. Consequently, also the absolute values of the scattering angles for spin-up and spin-down electrons can differ, which, nonetheless, reflects the skew-scattering contribution. The side-jump effect expresses itself in a spatial displacement (dashed lines). The figure is adapted from reference [76].

the scattering asymmetry between both spin states becomes apparent.

Secondly, considering electrons as wave packets, a shift of the center of mass before and after the scattering event can be identified (compare figures 1.3 and 2.4). Accordingly, this mechanism is named side jump [77]. Although the coordinate shifts [39] appear in all directions, only those along the  $y$  direction account for the side-jump contribution to the SHE in systems with charge current along  $x$  and spin quantization axis along  $z$  axis.

A possible and illustrative treatment is based on the transverse velocity component [22, 39]

$$v_y^{\text{sj}}(\mathbf{k}) = \sum_{\mathbf{k}'} P_{\mathbf{k}\mathbf{k}'} (\delta \mathbf{r}_{\mathbf{k}\mathbf{k}'})_y. \quad (2.136)$$

It combines the real space coordinate shift with the corresponding scattering probability where the information about the side-jump effect itself is stored in  $\delta \mathbf{r}$ . The actual problem is to find an appropriate description for this quantity.

According to a proposal from Sinitsyn et al. [78], side jump originates from the anomalous velocity (2.120). Considering this together with the force term (2.98) allows to write

$$\dot{\mathbf{r}} = \frac{1}{\hbar} \frac{\partial E_{\mathbf{k}}}{\partial \mathbf{k}} - \dot{\mathbf{k}} \times \boldsymbol{\Omega}_{\mathbf{k}}. \quad (2.137)$$

The integration of equation (2.137) over the time interval at which the electron feels the impurity potential during a single scattering event leads to

$$\delta \mathbf{r}_{\mathbf{k}\mathbf{k}'} = \frac{1}{\hbar} \int_{t_1}^{t_2} dt \frac{\partial E_{\mathbf{k}}}{\partial \mathbf{k}} + \boldsymbol{\Omega}_{\mathbf{k}} \times (\mathbf{k}' - \mathbf{k}), \quad (2.138)$$

where  $\mathbf{k}$  and  $\mathbf{k}'$  are the momenta before and after scattering, respectively, and a constant Berry curvature is assumed. The times  $t_1$  and  $t_2$  indicate the instants when the electron enters or leaves the impurity in a semiclassical picture. Due to the random character of the scattering events from the first term of equation (2.138), these contributions vanish during the averaging process of equation (2.136) [78]. On the contrary, the second term does not disappear by reason of the present Berry curvature. Accordingly, one can write

$$\delta \mathbf{r}_{\mathbf{k}\mathbf{k}'}^{\text{sj}} = \boldsymbol{\Omega}_{\mathbf{k}} \times (\mathbf{k}' - \mathbf{k}) \quad (2.139)$$

as the electron's microscopic displacement which contributes to the entire spin Hall conductivity

$$\sigma_{yx}^{\text{sj}} = \frac{e^2}{\hbar(2\pi)^3} \sum_{\nu, \mathbf{k}'} \oint_{E_{\mathbf{k}}=E_F} \frac{dS_{\nu}}{|\mathbf{v}_{\mathbf{k}}'|} s_z^{\nu}(\mathbf{k}) P_{\mathbf{k}\mathbf{k}'} (\boldsymbol{\Omega}_{\mathbf{k}} \times (\mathbf{k}' - \mathbf{k}))_y \Lambda_x^{\nu}(\mathbf{k}). \quad (2.140)$$

Sinitsyn et al. [39] presented another route to derive equation (2.139) by far extensive derivation steps. The approach relies on the explicit expression of incoming and outgoing wave packets in terms of eigenstates of the unperturbed Hamiltonian and a Gaussian envelope function. Accordingly, the charge centers before and after the scattering event can be calculated. Their difference in the lowest nonzero Born approximation is given by [39]

$$\delta \mathbf{r}_{\mathbf{k}\mathbf{k}'} = \left\langle u_{\mathbf{k}'} \left| i \frac{\partial}{\partial \mathbf{k}'} u_{\mathbf{k}'} \right. \right\rangle - \left\langle u_{\mathbf{k}} \left| i \frac{\partial}{\partial \mathbf{k}} u_{\mathbf{k}} \right. \right\rangle - \left( \frac{\partial}{\partial \mathbf{k}'} + \frac{\partial}{\partial \mathbf{k}} \right) \arg(V_{\mathbf{k}\mathbf{k}'}), \quad (2.141)$$

where  $|u_{\mathbf{k}}\rangle$  is the Bloch state's momentum-dependent periodic spinor and  $V_{\mathbf{k}\mathbf{k}'}$  represents the disorder potential matrix. Equation (2.141) delivers a gauge invariant expression for the electron's coordinate shift due to side jump with a clear semiclassical interpretation. Further assumptions of a radial spin-independent impurity potential implying  $V_{\mathbf{k}\mathbf{k}'} \propto \langle u_{\mathbf{k}'} | u_{\mathbf{k}} \rangle$  and a small scattering angle ( $|\mathbf{k}' - \mathbf{k}| \ll |\mathbf{k}|$ ) leading to  $|u_{\mathbf{k}'}\rangle \approx |u_{\mathbf{k}}\rangle + (\mathbf{k}' - \mathbf{k}) |\partial u_{\mathbf{k}} / \partial \mathbf{k}\rangle$  result in equation (2.139) [39].

In the considered case of a spin-independent impurity potential, the above approach does not explicitly depend on the impurity potential itself but relies on the electronic structure of the host contributing to equation (2.139) via the Berry curvature.

Another way to derive a side-jump velocity which includes the influence of the impurity potential follows a derivation of Peter Levy [79]. Accordingly, a suitable starting point is the Hamiltonian

$$\hat{H} = \frac{p^2}{2m} + N_i \hat{V} \quad (2.142)$$

consisting of the usual kinetic energy and the perturbation due to external impurity potentials, where  $N_i$  represents the number of such impurities. In the framework of a semiclassical approach, the application of the Ehrenfest theorem is suitable. As well known, it relates the time derivative of the expectation value of any quantum mechanical operator to the commutator of that operator with the system's Hamil-

tonian. Hence, the electron velocity can be obtained as

$$\dot{\mathbf{r}}_{\mathbf{k}} = \mathbf{v}_{\mathbf{k}} = \left\langle \tilde{\mathbf{k}} \left| \frac{i}{\hbar} [\hat{H}, \mathbf{r}] \right| \tilde{\mathbf{k}} \right\rangle = \frac{\mathbf{p}_{\mathbf{k}}}{m} + \mathbf{v}^a(\mathbf{k}), \quad (2.143)$$

where the contribution

$$\mathbf{v}^a(\mathbf{k}) = N_i \left\langle \tilde{\mathbf{k}} \left| \frac{[\mathbf{r}, \hat{V}]}{i\hbar} \right| \tilde{\mathbf{k}} \right\rangle \quad (2.144)$$

represents the anomalous velocity whose components transverse to the applied electric field will be identified with the side-jump contribution. With the help of the Lippmann-Schwinger equation (2.29)

$$|\tilde{\mathbf{k}}\rangle = \left[ 1 + \hat{G}(E_{\mathbf{k}}) \hat{T} \right] |\mathbf{k}\rangle \quad (2.145)$$

it is possible to express the perturbed state  $|\tilde{\mathbf{k}}\rangle$  via the unperturbed state  $|\mathbf{k}\rangle$ , the Green function of the ideal system and the corresponding transition operator. For the evaluation of equation (2.144) it will be helpful to rewrite the commutator as

$$\left\langle \tilde{\mathbf{k}} \left| [\mathbf{r}, \hat{V}] \right| \tilde{\mathbf{k}} \right\rangle = 2i \operatorname{Im} \left\langle \tilde{\mathbf{k}} \left| \mathbf{r} \hat{V} \right| \tilde{\mathbf{k}} \right\rangle. \quad (2.146)$$

As known from equations (2.26) and (2.29), the connection between external potential and transition operator can be used to formulate

$$\left\langle \tilde{\mathbf{k}} \left| \mathbf{r} \hat{V} \right| \tilde{\mathbf{k}} \right\rangle = \left\langle \tilde{\mathbf{k}} \left| \mathbf{r} \hat{T} \right| \mathbf{k} \right\rangle. \quad (2.147)$$

Additionally, it is helpful to take into account the completeness

$$\mathbb{1} = \sum_{\mathbf{k}'} |\mathbf{k}'\rangle \langle \mathbf{k}'| \quad (2.148)$$

of the eigenstates. Based on the  $\mathbf{k}$  state's real-space representation  $\langle \mathbf{r} | \mathbf{k}' \rangle = e^{i\mathbf{k}' \cdot \mathbf{r}}$ , the reformulation

$$\langle \tilde{\mathbf{k}} | \mathbf{r} | \mathbf{k}' \rangle = -i \nabla_{\mathbf{k}'} \langle \tilde{\mathbf{k}} | \mathbf{k}' \rangle \quad (2.149)$$

can be found. The combination of the above equations leads to

$$\begin{aligned} \left\langle \tilde{\mathbf{k}} \left| \mathbf{r} \hat{V} \right| \tilde{\mathbf{k}} \right\rangle &= \sum_{\mathbf{k}'} \langle \tilde{\mathbf{k}} | \mathbf{r} | \mathbf{k}' \rangle \langle \mathbf{k}' | \hat{T} | \mathbf{k} \rangle \\ &= -i \sum_{\mathbf{k}'} \left[ \nabla_{\mathbf{k}'} \langle \tilde{\mathbf{k}} | \mathbf{k}' \rangle \right] \langle \mathbf{k}' | \hat{T} | \mathbf{k} \rangle \\ &= i \sum_{\mathbf{k}'} \langle \tilde{\mathbf{k}} | \mathbf{k}' \rangle \nabla_{\mathbf{k}'} \langle \mathbf{k}' | \hat{T} | \mathbf{k} \rangle - i \sum_{\mathbf{k}'} \nabla_{\mathbf{k}'} \left[ \langle \tilde{\mathbf{k}} | \mathbf{k}' \rangle \langle \mathbf{k}' | \hat{T} | \mathbf{k} \rangle \right]. \end{aligned} \quad (2.150)$$

The second term in the last line of equation (2.150) vanishes. This becomes obvious when it is written in integral form and the limit [79]

$$\lim_{k' \rightarrow \infty} \langle \tilde{\mathbf{k}} | \mathbf{k}' \rangle = 0 \quad (2.151)$$

is taken into account. The adjoint expression of equation (2.145) allows to reformulate

$$\langle \tilde{\mathbf{k}} | \mathbf{k}' \rangle = \langle \mathbf{k} | \mathbf{k}' \rangle + \langle \mathbf{k} | \hat{T}^\dagger | \mathbf{k}' \rangle \hat{G}^\dagger(E_{\mathbf{k}}). \quad (2.152)$$

Using this result for equation (2.150) and taking into account the orthogonality of the states, it is possible to write

$$\begin{aligned} \langle \tilde{\mathbf{k}} | \mathbf{r} \hat{V} | \tilde{\mathbf{k}} \rangle &= i \sum_{\mathbf{k}'} \langle \tilde{\mathbf{k}} | \mathbf{k}' \rangle \nabla_{\mathbf{k}'} \langle \mathbf{k}' | \hat{T} | \mathbf{k} \rangle \\ &= i \nabla_{\mathbf{k}} \langle \mathbf{k} | \hat{T} | \mathbf{k} \rangle + i \sum_{\mathbf{k}'} \langle \mathbf{k} | \hat{T}^\dagger | \mathbf{k}' \rangle \hat{G}^\dagger(E_{\mathbf{k}}) \nabla_{\mathbf{k}'} \langle \mathbf{k}' | \hat{T} | \mathbf{k} \rangle. \end{aligned} \quad (2.153)$$

The combination of equations (2.144), (2.146), and (2.153) leads to

$$\begin{aligned} \mathbf{v}^a(\mathbf{k}) &= \frac{2N_i}{\hbar} \text{Im} \langle \tilde{\mathbf{k}} | \mathbf{r} \hat{V} | \tilde{\mathbf{k}} \rangle \\ &= \frac{2N_i}{\hbar} \left[ \text{Re} \nabla_{\mathbf{k}} T_{\mathbf{k}\mathbf{k}} + \text{Re} \sum_{\mathbf{k}'} T_{\mathbf{k}'\mathbf{k}}^\dagger \hat{G}^\dagger(E_{\mathbf{k}}) \nabla_{\mathbf{k}'} T_{\mathbf{k}\mathbf{k}'} \right] \end{aligned} \quad (2.154)$$

for the anomalous velocity. In a further step, the spectral representation of the Green function (2.19) as well as the Dirac identity (2.20) lead to

$$\begin{aligned} \mathbf{v}_a(\mathbf{k}) &= \frac{2N_i}{\hbar} \left[ \text{Re} \nabla_{\mathbf{k}} T_{\mathbf{k}\mathbf{k}} + \sum_{\mathbf{k}'} \mathcal{P} \left( \frac{1}{E_{\mathbf{k}} - E_{\mathbf{k}'}} \right) \text{Re} \left\{ T_{\mathbf{k}'\mathbf{k}}^\dagger \nabla_{\mathbf{k}'} T_{\mathbf{k}\mathbf{k}'} \right\} \right. \\ &\quad \left. - \pi \sum_{\mathbf{k}'} \delta(E_{\mathbf{k}} - E_{\mathbf{k}'}) \text{Im} \left\{ T_{\mathbf{k}'\mathbf{k}}^\dagger \nabla_{\mathbf{k}'} T_{\mathbf{k}\mathbf{k}'} \right\} \right] \end{aligned} \quad (2.155)$$

as the expression, which was already used by Fert and Levy [38] for material-specific calculations of the side-jump effect. As stated in this paper and shown explicitly by Levy [79] by means of a long and elaborate derivation, only the last term in equation (2.155) contributes to the Hall effect. Accordingly, one has to insert

$$\mathbf{v}^{\text{sj}}(\mathbf{k}) = -\frac{2\pi N_i}{\hbar} \sum_{\mathbf{k}'} \delta(E_{\mathbf{k}} - E_{\mathbf{k}'}) \text{Im} \left\{ T_{\mathbf{k}'\mathbf{k}}^\dagger \nabla_{\mathbf{k}'} T_{\mathbf{k}\mathbf{k}'} \right\} \quad (2.156)$$

into equation (2.133) in order to find the corresponding side-jump conductivity.

An important point to be discussed is the different dependence of the skew-scattering and side-jump mechanisms on the impurity concentration in the system [22]. While it is quite obvious that the intrinsic contribution to the SHC does not depend on the impurity concentration, a closer look for the extrinsic mechanisms is required. It is most precise to compare the corresponding current densities according to equation (2.127) caused by the two extrinsic effects. As can be understood following equations (2.103) - (2.106), the non-equilibrium part of the distribution function  $g_{\mathbf{k}}$  is inversely proportional to the impurity concentration

$$g_{\mathbf{k}} \propto (c_0)^{-1}. \quad (2.157)$$



The information on the skew-scattering mechanism is stored in the mean-free path  $\Lambda_{\mathbf{k}}$  which directly enters the distribution function  $g_{\mathbf{k}}$ . Due to the independence of the Fermi velocity on the impurity concentration in equation (2.127), the current density arising from skew scattering is inversely proportional to  $c_0$

$$\mathbf{j}^{\text{skew}} \propto (c_0)^{-1}. \quad (2.158)$$

On the contrary, the information about side jump is stored in the side-jump velocity  $v_{\mathbf{k}}^{\text{sj}}$  of equation (2.136) where the spacial shift according to a unique scattering event  $\delta\mathbf{r}_{\mathbf{k}\mathbf{k}'}$  is obviously independent of impurity concentration. Considering the linear concentration dependence of the transition probability due to equation (2.106), the side-jump current density (and consequently the side-jump conductivity) becomes independent of the impurity concentration

$$\mathbf{j}^{\text{sj}} \propto (c_0)^0. \quad (2.159)$$

The same discussion is valid considering the side-jump velocity from equation (2.156) which is linear in the total number of impurities and consequently linear dependent on the impurity concentration. According to this discussion, the skew-scattering mechanism dominates over side jump in the dilute limit of impurity concentration. In order to circumvent any possible confusions I want to highlight once more that the above given statements hold for current densities and conductivities only. Obviously, the situation is different for the spin Hall angle which is concentration independent for skew scattering but depends linearly on  $c_0$  for the side-jump mechanism.

Another point worth mentioning in the framework of this discussion is the occasionally discussed *intrinsic skew scattering* associated with the so-called ladder diagram corrections of the microscopic Kubo-Středa theory [80]. Although this contribution, which is not considered in the present work, also arises from the antisymmetric scattering rate, the corresponding spin Hall conductivity is independent of the impurity concentration [22] similar to the side-jump contribution. Consequently and in agreement with reference [81], it is also possible to ascribe this contribution to the side-jump mechanism when decomposing the SHE according to equation (1.10).

## 2.4. Phase Shift Models for the Spin Hall Effect

During the presentation of various expressions for the transition matrix in section 2.2.2, it was shown, that spin-orbit coupling can be incorporated by a series expansion in the SOC constant  $\lambda_l$ . In this case, spin-orbit coupling effects, which are mandatory for the description of the spin Hall effect, are taken into account in a perturbative way. An additional assumption is related to spin-flip scattering events. As it is known from reference [82], the results for bulk systems do not drastically change incorporating spin-flip scattering. Therefore, spin-flip contributions will be neglected, in order to simplify the corresponding consideration.

An appropriate starting point for a formulation of the conductivity tensor in terms of scattering phase shifts is given by equation (2.131). The used approach for an analytical evaluation of the emerging integrals is the consideration of the spherical band approximation

$$E_{\mathbf{k}} = \frac{\hbar^2 k^2}{2m_e}, \quad \mathbf{v}_{\mathbf{k}} = \frac{\hbar \mathbf{k}}{m_e}, \quad \oint_{E_{\mathbf{k}}=E_F} dS_{\mathbf{k}} = k_F^2 \int d\Omega_{\mathbf{k}} = k_F^2 \int_0^{2\pi} d\phi_{\mathbf{k}} \int_0^{\pi} d\theta_{\mathbf{k}} \sin \theta_{\mathbf{k}} \quad (2.160)$$

which leads to

$$\underline{\sigma} = \frac{e^2 m_e k_F}{\hbar^2 (2\pi)^3} \int d\Omega_{\mathbf{k}} \mathbf{v}_{\mathbf{k}} \circ \mathbf{\Lambda}_{\mathbf{k}} \quad (2.161)$$

with the vector mean free path  $\mathbf{\Lambda}_{\mathbf{k}}$  given by equation (2.104).

### 2.4.1. Longitudinal Conductivity

Prior to the formulation of contributions to the spin Hall effect, it is worth to consider a conventional quantity such as the charge conductivity in the framework of scattering phase shifts. As shown in the introduction (equation (1.6)), the conductivity tensor is composed of the respective terms for each spin component. Thus, in presence of time and space inversion symmetry, the longitudinal conductivity is given by  $\sigma_{xx} = 2\sigma_{xx}^+$ . In order to get  $\sigma_{xx}^+$ , we include the Fermi velocity in spherical band approximation from equation (2.160), the mean free path  $\mathbf{\Lambda}_{\mathbf{k}}$  from equation (2.104) restricting the consideration to the scattering-out term here<sup>1</sup>, as well as the transition probability from equation (2.106) into equation (2.161) which leads to

$$\sigma_{xx}^+ = \frac{e^2 m_e k_F \tau_0}{\hbar^2 (2\pi)^3} \int d\Omega_{\mathbf{k}} v_{\mathbf{k}}^x v_{\mathbf{k}}^x = \frac{e^2 k_F \tau_0}{m_e (2\pi)^3} \int d\Omega_{\mathbf{k}} k_x^2, \quad (2.162)$$

where the assumption of an isotropic momentum relaxation time  $\tau_{\mathbf{k}} \approx \tau_0$  was used according to reference [38]. Taking into account that

$$\int d\Omega_{\mathbf{k}} k_x^2 = \frac{k_F^2}{3} \int d\Omega_{\mathbf{k}} = \frac{4\pi k_F^2}{3}, \quad (2.163)$$

---

<sup>1</sup>An additional investigation on the extended case can be found in appendix B.

the longitudinal conductivity

$$\sigma_{xx}^+ = \frac{e^2 k_F^3}{6\pi^2 m_e} \tau_0 \quad (2.164)$$

can be expressed in terms of the isotropic momentum relaxation time. The actual form of  $\tau_0$  will be determined in the following sections depending on whether non-relativistic or relativistic scattering phase shifts are used.

### 2.4.2. Skew Scattering

As was already mentioned in the introduction, the spin Hall effect manifests itself via an off-diagonal component in the conductivity tensor. Similar to the charge conductivity, the starting point for the following consideration is equation (2.161) where a crucial quantity is the mean free path. For the consideration of skew scattering in cubic systems, only the scattering-in term needs to be incorporated [22, 33, 36, 82]. Similar to the charge conductivity, the spin Hall conductivity  $\sigma_{yx}^s = 2\sigma_{yx}^+$  is composed of the respective terms for each spin component. Following the steps outlined above,  $\sigma_{yx}^+$  can be obtained as

$$\sigma_{yx}^+ = \frac{c_0 N V e^2 k_F^2 \tau_0^2}{\hbar^3 (2\pi)^5} \int d\Omega_{\mathbf{k}} \int d\Omega_{\mathbf{k}'} k_y k'_x |T_{\mathbf{k}'\mathbf{k}}^{++}|^2. \quad (2.165)$$

A reasonable approximation used during this derivation is the restriction  $\mathbf{\Lambda}_{\mathbf{k}'} = \tau_0 \frac{\hbar \mathbf{k}'}{m_e}$  which, apart from  $\tau_{\mathbf{k}} \approx \tau_0$ , is identical to the first iteration within the iterative procedure for  $\mathbf{\Lambda}_{\mathbf{k}}$  in equation (2.104).

Depending on the phase shifts to be used, the transition matrices from equations (2.114) or (2.116) can be inserted into (2.165). Nonetheless, the analytical derivation can be simplified taking into account that only the antisymmetric part of the microscopic transition probability

$$P_{\mathbf{k}'\mathbf{k}}^{\text{antisym}} = \frac{P_{\mathbf{k}'\mathbf{k}} - P_{\mathbf{k}\mathbf{k}'}}{2} \quad (2.166)$$

contributes to the skew-scattering mechanism [38, 67]. According to this, one can write

$$\sigma_{yx}^+ = \frac{c_0 N V e^2 k_F^2 \tau_0^2}{\hbar^3 (2\pi)^5} \int d\Omega_{\mathbf{k}} \int d\Omega_{\mathbf{k}'} k_y k'_x |T_{\mathbf{k}'\mathbf{k}}^{++}|_{\text{antisym}}^2, \quad (2.167)$$

where  $|T_{\mathbf{k}'\mathbf{k}}^{++}|_{\text{antisym}}^2$  is to be understood in the style of equation (2.166) as

$$|T_{\mathbf{k}'\mathbf{k}}^{++}|_{\text{antisym}}^2 = \frac{|T_{\mathbf{k}'\mathbf{k}}|^2 - |T_{\mathbf{k}\mathbf{k}'}|^2}{2} = -|T_{\mathbf{k}\mathbf{k}'}^+|^2_{\text{antisym}}. \quad (2.168)$$

### Phase Shift Model in Terms of Non-Relativistic Phase Shifts

Considering equation (2.114) one can find that the first term on the right-hand side is antisymmetric when interchanging  $\mathbf{k}$  and  $\mathbf{k}'$  since the factor  $m$  changes sign in

the corresponding sum. In contrast, the second term is symmetric in this respect. Accordingly, only the cross terms contribute to  $|T_{\mathbf{k}\mathbf{k}'}^{++}|_{\text{antisym}}^2$  which leads to

$$|T_{\mathbf{k}\mathbf{k}'}^{++}|_{\text{antisym}}^2 = \frac{64\pi^4\hbar^4}{V^2m_e^2k_F^2}i \sum_{lm} \sum_{l'm'} m \frac{\lambda_l}{\Delta_l} \sin(2\eta_l - \eta_{l'}) \sin^2 \eta_l \sin \eta_{l'} \times \\ Y_l^m(\hat{\mathbf{k}}) \left(Y_l^m(\hat{\mathbf{k}}')\right)^* \left(Y_{l'}^{m'}(\hat{\mathbf{k}})\right)^* Y_{l'}^{m'}(\hat{\mathbf{k}}'). \quad (2.169)$$

To derive the Hall component of the conductivity tensor  $\underline{\sigma}^+$ , one can interchange  $\mathbf{k}$  and  $\mathbf{k}'$  in equation (2.167) and use equation (2.169) directly. The representation of  $k_x$  and  $k'_y$  in terms of spherical harmonics by

$$k_x = \sqrt{\frac{2\pi}{3}}k_F \left[Y_1^{-1}(\hat{\mathbf{k}}) - Y_1^1(\hat{\mathbf{k}})\right] \quad \text{and} \quad k'_y = i\sqrt{\frac{2\pi}{3}}k_F \left[Y_1^{-1}(\hat{\mathbf{k}}') + Y_1^1(\hat{\mathbf{k}}')\right] \quad (2.170)$$

leads to integrals over the angular parts  $\Omega_{\mathbf{k}}$  and  $\Omega_{\mathbf{k}'}$  incorporating three spherical harmonics. The evaluation of those is outlined in appendix C. Accordingly, it is possible to obtain

$$\sigma_{yx}^+ = -\frac{e^2\hbar k_F^2 c_0}{2\pi m_e^2 V_0} \tau_0^2 \sum_{lm} \sum_{l'm'} m \frac{\lambda_l}{\Delta_l} \sin(2\eta_l - \eta_{l'}) \sin^2 \eta_l \sin \eta_{l'} \times \\ \left\{ \delta_{l',l+1} \left[ \delta_{m',m+1} \frac{(l+m+1)(l+m+2)}{(2l+1)(2l+3)} - \delta_{m',m-1} \frac{(l-m+1)(l-m+2)}{(2l+1)(2l+3)} \right] \right. \\ \left. + \delta_{l',l-1} \left[ \delta_{m',m+1} \frac{(l-m)(l-m-1)}{(2l-1)(2l+1)} - \delta_{m',m-1} \frac{(l+m)(l+m-1)}{(2l-1)(2l+1)} \right] \right\} \quad (2.171)$$

as the Hall component of the conductivity tensor for the spin-up channel expressed in terms of non-relativistic phase shifts with  $V_0 = V/N$  as the unit-cell volume. Finally, the reasonable restriction to  $\{l, l'\} \leq 3$  which considers the important scattering contributions between  $s, p, d$ , and  $f$  states leads to

$$\sigma_{yx}^+ = \left(\frac{e^2}{\hbar}\right) \left(\frac{2\hbar^2 k_F^2 c_0}{\pi m_e^2 V_0}\right) \tau_0^2 \left\{ \frac{1}{3} \frac{\lambda_1 \sin^2 \eta_1}{\Delta_1} [\sin(2\eta_1 - \eta_0) \sin \eta_0 - \sin(2\eta_1 - \eta_2) \sin \eta_2] \right. \\ \left. + \frac{\lambda_2 \sin^2 \eta_2}{\Delta_2} [\sin(2\eta_2 - \eta_1) \sin \eta_1 - \sin(2\eta_2 - \eta_3) \sin \eta_3] \right. \\ \left. + 2 \frac{\lambda_3 \sin^2 \eta_3}{\Delta_3} \sin(2\eta_3 - \eta_2) \sin \eta_2 \right\}. \quad (2.172)$$

Multiplying with a factor of 2 considers the second spin channel and delivers the total SHC. In order to express the spin Hall conductivity of equation (2.172) solely in terms of the phase shifts it is necessary to evaluate the isotropic relaxation time  $\tau_0$ . Starting from equations (2.105) and (2.106) and inserting the  $T$  matrix from equation (2.114) provides

$$\frac{1}{\tau_{\mathbf{k}}} = \frac{4\pi^2 \hbar c_0 N}{m_e k_F V} \int d\Omega_{\mathbf{k}'} \left| \sum_{lm} \left(Y_l^m(\hat{\mathbf{k}})\right)^* Y_l^m(\hat{\mathbf{k}}') e^{im} \sin \eta_l \left(m \frac{\lambda_l}{\Delta_l} e^{im} \sin \eta_l - 2\right) \right|^2. \quad (2.173)$$

With the help of the relations

$$\sum_{m=-l}^l mf(l) = 0, \quad \sum_{m=-l}^l f(l) = (2l+1)f(l), \quad \sum_{m=-l}^l m^2 = \frac{l(l+1)(2l+1)}{3} \quad (2.174)$$

as well as the consideration that the averaged (or isotropic) momentum relaxation time is given by

$$\frac{1}{\tau_0} = \frac{1}{4\pi} \int d\Omega_{\mathbf{k}} \frac{1}{\tau_{\mathbf{k}}} \quad (2.175)$$

one can easily find

$$\frac{1}{\tau_0} = \frac{4\pi\hbar c_0}{m_e k_F V_0} \sum_l (2l+1) \sin^2 \eta_l \left[ 1 + \frac{l(l+1)}{12} \frac{\lambda_l^2}{\Delta_l^2} \sin^2 \eta_l \right]. \quad (2.176)$$

Another possible route to execute the isotropic relaxation time approximation is to assume that  $\tau_{\mathbf{k}}$  does not change drastically with  $\mathbf{k}$  on the Fermi surface. Consequently, one can suppose  $\tau_0 = \tau_{\mathbf{k}_0}$  with  $\mathbf{k}_0 = (0, 0, k_F)$ . Starting from equation (2.173) and incorporating  $Y_l^m(\hat{\mathbf{z}}) = \sqrt{\frac{2l+1}{4\pi}} \delta_{m,0}$  provides the commonly used (non-relativistic) form [55]

$$\frac{1}{\tau_0} = \frac{4\pi\hbar c_0}{m_e k_F V_0} \sum_l (2l+1) \sin^2 \eta_l. \quad (2.177)$$

This approach neglects the second order term with respect to the SOC strength in equation (2.176). Therefore, it is a good approximation if the SOC constant is smaller than the resonance width [67].

Besides the relaxation time, it is the SOC constant for the impurity atom in the considered host that has to be expressed in terms of scattering phase shifts. Often, it is approximated by the corresponding atomic SOC constant [38,83]. Nevertheless, the value for an isolated atom can differ significantly from  $\lambda_l$  for an impurity atom embedded in a host [84,85]. Additionally, the resonance width often approximated by a fixed value [38] needs to be clarified. It is worthwhile to use an expression for  $\lambda_l$  and  $\Delta_l$  in terms of phase shifts which can be obtained by means of *ab initio* calculations performed for a real impurity system [85]. In this way, one can generalize equation (2.172) using the relations [86]

$$\frac{\lambda_l \sin^2 \eta_l}{\Delta_l} = \frac{2(\delta_{l-\frac{1}{2}} - \delta_{l+\frac{1}{2}})}{2l+1}, \quad (2.178)$$

$$\eta_l = \frac{l\delta_{l-\frac{1}{2}} + (l+1)\delta_{l+\frac{1}{2}}}{2l+1} \quad (2.179)$$

based on the phase shifts related to the relativistic quantum number  $j = l \pm \frac{1}{2}$ . Consequently, it is possible to apply equation (2.172) for any impurity system beyond the special case of resonance scattering since no special assumptions for the impurity states are made.

### Phase Shift Model in Terms of Relativistic Phase Shifts

The derivation of an expression for the spin Hall conductivity in terms of relativistic phase shifts is carried out following the steps described for non-relativistic phase shifts, above. A suitable starting point is to rewrite equation (2.116) as

$$T_{\mathbf{k}\mathbf{k}'}^{++} = -\frac{8\pi^2\hbar^2}{m_e k_F V} \sum_{lm} \frac{\left(Y_l^m(\hat{\mathbf{k}})\right)^* Y_l^m(\hat{\mathbf{k}}')}{2l+1} \left\{ m \left[ e^{i\delta_{l+1/2}} \sin \delta_{l+1/2} - e^{i\delta_{l-1/2}} \sin \delta_{l-1/2} \right] \right. \\ \left. + (l+1)e^{i\delta_{l+1/2}} \sin \delta_{l+1/2} + le^{i\delta_{l-1/2}} \sin \delta_{l-1/2} \right\}. \quad (2.180)$$

As was already pointed out in the previous section, the term  $\sum_m m(Y_l^m(\hat{\mathbf{k}}))^* Y_l^m(\hat{\mathbf{k}}')$  is antisymmetric with respect to an exchange of  $\mathbf{k}$  and  $\mathbf{k}'$  while  $\sum_m (Y_l^m(\hat{\mathbf{k}}))^* Y_l^m(\hat{\mathbf{k}}')$  is symmetric. Consequently, it is possible to show that

$$|T_{\mathbf{k}\mathbf{k}'}^{++}|_{\text{antisym}}^2 = \frac{128\pi^4\hbar^4}{V^2 m_e^2 k_F^2} i \sum_{lm} \sum_{l'm'} m \frac{Y_l^m(\hat{\mathbf{k}}) \left(Y_l^m(\hat{\mathbf{k}}')\right)^* \left(Y_{l'}^{m'}(\hat{\mathbf{k}})\right)^* Y_{l'}^{m'}(\hat{\mathbf{k}}')}{2l+1} f_{ll'} \quad (2.181)$$

with

$$f_{ll'} = \frac{1}{2l'+1} \left\{ (l'+1) \sin(\delta_{l'+1/2} - \delta_{l+1/2}) \sin \delta_{l+1/2} \sin \delta_{l'+1/2} \right. \\ \left. + l' \sin(\delta_{l'-1/2} - \delta_{l+1/2}) \sin \delta_{l+1/2} \sin \delta_{l'-1/2} \right. \\ \left. - (l'+1) \sin(\delta_{l'+1/2} - \delta_{l-1/2}) \sin \delta_{l-1/2} \sin \delta_{l'+1/2} \right. \\ \left. - l' \sin(\delta_{l'-1/2} - \delta_{l-1/2}) \sin \delta_{l-1/2} \sin \delta_{l'-1/2} \right\}. \quad (2.182)$$

In order to derive the Hall component of the conductivity tensor  $\underline{\sigma}^+$ , one can execute the steps presented in the previous section. This leads to

$$\sigma_{yx}^+ = \left(\frac{e^2}{\hbar}\right) \left(\frac{2\hbar^2 k_F^2 c_0}{\pi m_e^2 V_0}\right) \tau_0^2 \sum_{lm} \sum_{l'm'} \frac{m f_{ll'}}{2l+1} \times \\ \left\{ \delta_{l',l+1} \left[ \delta_{m',m-1} \frac{(l-m+1)(l-m+2)}{(2l+1)(2l+3)} - \delta_{m',m+1} \frac{(l+m+1)(l+m+2)}{(2l+1)(2l+3)} \right] \right. \\ \left. + \delta_{l',l-1} \left[ \delta_{m',m-1} \frac{(l+m)(l+m-1)}{(2l-1)(2l+1)} - \delta_{m',m+1} \frac{(l-m)(l-m-1)}{(2l-1)(2l+1)} \right] \right\} \quad (2.183)$$

or

$$\sigma_{yx}^+ = \left(\frac{e^2}{\hbar}\right) \left(\frac{4\hbar^2 k_F^2 c_0}{\pi m_e^2 V_0}\right) \tau_0^2 \left\{ \frac{1}{9}(f_{10} - f_{12}) + \frac{1}{5}(f_{21} - f_{23}) + \frac{2}{7}f_{32} \right\} \quad (2.184)$$

if the restriction to  $s, p, d$ , and  $f$  states is made again and  $f_{10}, \dots, f_{32}$  are defined by equation (2.182).

The derivation of the isotropic relaxation time can be executed similarly to the

previous section when  $\tau_0 = \tau_{\mathbf{k}_0}$  with  $\mathbf{k}_0 = (0, 0, k_F)$  was assumed. Accordingly,

$$\frac{1}{\tau_0^{++}} = \frac{4\pi\hbar c_0}{m_e k_F V_0} \sum_l \left\{ \frac{(l+1)^2}{2l+1} \sin^2 \delta_{l+\frac{1}{2}} + \frac{l^2}{2l+1} \sin^2 \delta_{l-\frac{1}{2}} + \frac{2l(l+1)}{2l+1} \cos(\delta_{l+\frac{1}{2}} - \delta_{l-\frac{1}{2}}) \sin \delta_{l+\frac{1}{2}} \sin \delta_{l-\frac{1}{2}} \right\} \quad (2.185)$$

can be found, where the absence of spin-flip contributions is highlighted explicitly since it is possible to simplify the expression for  $\tau_0$  by incorporating those. Namely, one can use equation (2.118) to obtain

$$\frac{1}{\tau_0^{+-}} = \frac{4\pi\hbar c_0}{m_e k_F V_0} \sum_l \frac{l(l+1)}{2l+1} \left\{ \sin^2 \delta_{l+\frac{1}{2}} + \sin^2 \delta_{l-\frac{1}{2}} - 2 \cos(\delta_{l+\frac{1}{2}} - \delta_{l-\frac{1}{2}}) \sin \delta_{l+\frac{1}{2}} \sin \delta_{l-\frac{1}{2}} \right\}. \quad (2.186)$$

Finally, the sum of the inverse relaxation times for spin-conserving and spin-flip scattering events gives

$$\frac{1}{\tau_0} = \frac{4\pi\hbar c_0}{m_e k_F V_0} \sum_l \left[ (l+1) \sin^2 \delta_{l+\frac{1}{2}} + l \sin^2 \delta_{l-\frac{1}{2}} \right]. \quad (2.187)$$

This expression is consistent with the well-known term for the relativistic scattering cross section [45]

$$\sigma_{\text{cs}} = \frac{4\pi}{k_F^2} \sum_l \left[ (l+1) \sin^2 \delta_{l+\frac{1}{2}} + l \sin^2 \delta_{l-\frac{1}{2}} \right] \quad (2.188)$$

which is related to  $\tau_0$  via [83]

$$\sigma_{\text{cs}} = \frac{V_0}{v_F c_0 \tau_0}. \quad (2.189)$$

### 2.4.3. Side Jump

In order to find a phase-shift representation for the side-jump conductivity, a combination of equations (2.156) and (2.161) leads to the spin-up channel contribution

$$\underline{\sigma}^{+, \text{sj}} = - \left( \frac{e^2}{\hbar} \right) \frac{c_0}{V_0} \frac{m_e^2 k_F^2}{(2\pi)^5 \hbar^4} \int d\Omega_{\mathbf{k}} \int d\Omega_{\mathbf{k}'} \text{Im} \left\{ \tilde{T}_{\mathbf{k}\mathbf{k}'}^* \nabla_{\mathbf{k}'} \tilde{T}_{\mathbf{k}\mathbf{k}'} \right\} \circ \mathbf{\Lambda}_{\mathbf{k}}, \quad (2.190)$$

where the sum over  $\mathbf{k}'$  states stemming from the side-jump velocity was rewritten into the corresponding integral as for equations (2.130) and (2.131). Additionally, the abbreviation  $\tilde{T}_{\mathbf{k}\mathbf{k}'} = VT_{\mathbf{k}\mathbf{k}'}$  is used. According to equation (2.104), the side-jump conductivity can be split into two parts  $\sigma^{\text{sj}} = \sigma^{\text{sj,I}} + \sigma^{\text{sj,II}}$  with

$$\sigma_{yx}^{+, \text{sj,I}} = - \left( \frac{e^2}{\hbar} \right) \frac{c_0}{V_0} \frac{m_e k_F^2}{(2\pi)^5 \hbar^3} \tau_0 \int d\Omega_{\mathbf{k}} \int d\Omega_{\mathbf{k}'} \text{Im} \left\{ \tilde{T}_{\mathbf{k}\mathbf{k}'}^* \frac{\partial \tilde{T}_{\mathbf{k}\mathbf{k}'}}{\partial k'_y} \right\} k_x \quad (2.191)$$

and

$$\sigma_{yx}^{+,sj,\text{II}} = - \left( \frac{e^2}{\hbar} \right) \frac{c_0}{V_0} \frac{m_e^2 k_F^2}{(2\pi)^5 \hbar^4} \frac{\hbar}{m_e} \tau_0^2 \int d\Omega_{\mathbf{k}} \int d\Omega_{\mathbf{k}''} \text{Im} \left\{ \tilde{T}_{\mathbf{k}\mathbf{k}''}^* \frac{\partial \tilde{T}_{\mathbf{k}\mathbf{k}''}}{\partial k_y''} \right\} \sum_{\mathbf{k}'} P_{\mathbf{k}'\mathbf{k}k'_x}. \quad (2.192)$$

Here, the consideration of the second part is restricted to the first iteration of the scattering-in term in order to attain an analytical expression for this contribution at reasonable expense. For the further derivation of the side-jump conductivity, the  $T$  matrix will be used as

$$T_{\mathbf{k}\mathbf{k}'} = - \frac{8\pi^2 \hbar^3}{V m_e \sqrt{2m_e E_F}} \sum_{lm} \left( Y_l^m(\hat{\mathbf{k}}) \right)^* Y_l^m(\hat{\mathbf{k}}') \times \left[ \left( \frac{l+m+1}{2l+1} \right) e^{i\delta_{l+\frac{1}{2}}} \sin \delta_{l+\frac{1}{2}} + \left( \frac{l-m}{2l+1} \right) e^{i\delta_{l-\frac{1}{2}}} \sin \delta_{l-\frac{1}{2}} \right], \quad (2.193)$$

where the Fermi wave vector was expressed in terms of the Fermi energy  $E_F$ . Again, the spherical band approximation is used in order to simplify the corresponding terms. With an appropriate expression for the  $\mathbf{k}$  derivative of the  $T$  matrix, which is presented in detail in appendix D, and by using the abbreviations

$$A_{lm} = 2E_F \left[ \left( \frac{l+m+1}{2l+1} \right) e^{2i\delta_{l+\frac{1}{2}}} \frac{\partial \delta_{l+\frac{1}{2}}}{\partial E} \Big|_{E=E_F} + \left( \frac{l-m}{2l+1} \right) e^{2i\delta_{l-\frac{1}{2}}} \frac{\partial \delta_{l-\frac{1}{2}}}{\partial E} \Big|_{E=E_F} \right] - (l+1) \left[ \left( \frac{l+m+1}{2l+1} \right) e^{i\delta_{l+\frac{1}{2}}} \sin \delta_{l+\frac{1}{2}} + \left( \frac{l-m}{2l+1} \right) e^{i\delta_{l-\frac{1}{2}}} \sin \delta_{l-\frac{1}{2}} \right], \quad (2.194)$$

$$B_{lm} = 2E_F \left[ \left( \frac{l+m+1}{2l+1} \right) e^{2i\delta_{l+\frac{1}{2}}} \frac{\partial \delta_{l+\frac{1}{2}}}{\partial E} \Big|_{E=E_F} + \left( \frac{l-m}{2l+1} \right) e^{2i\delta_{l-\frac{1}{2}}} \frac{\partial \delta_{l-\frac{1}{2}}}{\partial E} \Big|_{E=E_F} \right] + l \left[ \left( \frac{l+m+1}{2l+1} \right) e^{i\delta_{l+\frac{1}{2}}} \sin \delta_{l+\frac{1}{2}} + \left( \frac{l-m}{2l+1} \right) e^{i\delta_{l-\frac{1}{2}}} \sin \delta_{l-\frac{1}{2}} \right], \quad (2.195)$$



the first contribution to the side-jump conductivity, which includes solely the scattering-out term in the mean free path, can be written as

$$\begin{aligned}
\sigma_{yx}^{+,sj,I} = & - \left( \frac{e^2}{\hbar} \right) \frac{c_0}{V_0} \frac{\hbar}{2\pi m_e} \tau_0 \sum_{lm} \\
& \text{Re} \left\{ A_{lm} \left[ \frac{(l-m+1)(l-m+2)(l+m+1)}{(2l+1)(2l+3)^2} \right. \right. \\
& \quad \left. \left. - \frac{(l+m+1)(l+m+2)(l+m+3)}{(2l+1)(2l+3)^2} \right] e^{-i\delta_{(l+1)+\frac{1}{2}}} \sin \delta_{(l+1)+\frac{1}{2}} \right. \\
& + A_{lm} \left[ \frac{(l-m+1)(l-m+2)^2}{(2l+1)(2l+3)^2} \right. \\
& \quad \left. - \frac{(l+m+1)(l+m+2)(l-m)}{(2l+1)(2l+3)^2} \right] e^{-i\delta_{(l+1)-\frac{1}{2}}} \sin \delta_{(l+1)-\frac{1}{2}} \\
& + B_{lm} \left[ \frac{(l+m)(l+m-1)^2}{(2l+1)(2l-1)^2} \right. \\
& \quad \left. - \frac{(l-m)(l-m-1)(l+m+1)}{(2l+1)(2l-1)^2} \right] e^{-i\delta_{(l-1)+\frac{1}{2}}} \sin \delta_{(l-1)+\frac{1}{2}} \\
& \left. + B_{lm} \left[ \frac{(l+m)(l+m-1)(l-m)}{(2l+1)(2l-1)^2} \right. \right. \\
& \quad \left. \left. - \frac{(l-m)(l-m-1)(l-m-2)}{(2l+1)(2l-1)^2} \right] e^{-i\delta_{(l-1)-\frac{1}{2}}} \sin \delta_{(l-1)-\frac{1}{2}} \right\}. \tag{2.196}
\end{aligned}$$

Here, the relaxation time  $\tau_0$  is given by equation (2.187). As written explicitly in equation (2.184), only transitions between adjacent  $l$  channels contribute to the skew-scattering conductivity. The same feature remains for the first side-jump contribution.

The second part of the side-jump conductivity, which takes into account the first contribution to the scattering-in term of the mean free path, can be calculated similar to the first derivation. Due to the incorporation of the scattering probability  $P_{\mathbf{k}'\mathbf{k}}$ , the derivation is more complicated in comparison to the one executed for  $\sigma^{sj,I}$ .

Its detailed consideration is outlined in appendix D, which provides the following final expression

$$\begin{aligned}
\sigma_{yx}^{+,sj,\text{II}} = & \left( \frac{e^2}{\hbar} \right) \left( \frac{c_0}{V_0} \right)^2 \frac{8\pi\hbar^2}{m_e^2 k_F} \tau_0^2 \sum_{lm} \sum_{l_1 m_1} \sum_{l_2 m_2} \sum_{l_3 m_3} \sum_{LM} \text{Re} \\
& \left\{ (-1)^{m_2} \sqrt{\frac{(2l_1+1)(2l_2+1)(2l_3+1)}{(4\pi)^2(2l+1)}} C_{l_1 0, l_2 0}^{L0} C_{L 0, l_3 0}^{l0} C_{l_1 m_1, l_2 -m_2}^{LM} C_{LM, l_3 m_3}^{lm} \times \right. \\
& \left[ A_{lm} \left( \sqrt{\frac{(l-m+1)(l-m+2)}{(2l+1)(2l+3)}} \delta_{l_1, l+1} \delta_{m_1, m-1} + \sqrt{\frac{(l+m+1)(l+m+2)}{(2l+1)(2l+3)}} \delta_{l_1, l+1} \delta_{m_1, m+1} \right) \right. \\
& \left. - B_{lm} \left( \sqrt{\frac{(l+m-1)(l+m)}{(2l-1)(2l+1)}} \delta_{l_1, l-1} \delta_{m_1, m-1} + \sqrt{\frac{(l-m-1)(l-m)}{(2l-1)(2l+1)}} \delta_{l_1, l-1} \delta_{m_1, m+1} \right) \right] \times \\
& \left[ \left( \frac{l_1+m_1+1}{2l_1+1} \right) e^{-i\delta_{l_1+\frac{1}{2}}} \sin \delta_{l_1+\frac{1}{2}} + \left( \frac{l_1-m_1}{2l_1+1} \right) e^{-i\delta_{l_1-\frac{1}{2}}} \sin \delta_{l_1-\frac{1}{2}} \right] \times \\
& \left[ \left( \frac{l_2+m_2+1}{2l_2+1} \right) e^{-i\delta_{l_2+\frac{1}{2}}} \sin \delta_{l_2+\frac{1}{2}} + \left( \frac{l_2-m_2}{2l_2+1} \right) e^{-i\delta_{l_2-\frac{1}{2}}} \sin \delta_{l_2-\frac{1}{2}} \right] \times \\
& \left[ \left( \frac{l_3+m_3+1}{2l_3+1} \right) e^{i\delta_{l_3+\frac{1}{2}}} \sin \delta_{l_3+\frac{1}{2}} + \left( \frac{l_3-m_3}{2l_3+1} \right) e^{i\delta_{l_3-\frac{1}{2}}} \sin \delta_{l_3-\frac{1}{2}} \right] \times \\
& \left[ \delta_{l_3, l_2+1} \left( \delta_{m_3, m_2+1} \sqrt{\frac{(l_2+m_2+1)(l_2+m_2+2)}{(2l_2+1)(2l_2+3)}} - \delta_{m_3, m_2-1} \sqrt{\frac{(l_2-m_2+1)(l_2-m_2+2)}{(2l_2+1)(2l_2+3)}} \right) \right. \\
& \left. - \delta_{l_3, l_2-1} \left( \delta_{m_3, m_2+1} \sqrt{\frac{(l_2-m_2)(l_2-m_2-1)}{(2l_2+1)(2l_2-1)}} - \delta_{m_3, m_2-1} \sqrt{\frac{(l_2+m_2)(l_2+m_2-1)}{(2l_2+1)(2l_2-1)}} \right) \right] \left. \right\} \\
& \tag{2.197}
\end{aligned}$$

with  $A_{lm}$  and  $B_{lm}$  from equations (2.194) and (2.195) as well as the Clebsch-Gordon coefficients  $C_{l_1 m_1, l_2 m_2}^{LM}$  stemming from the representation of the angular integral over four spherical harmonics [87].

---

*“Make things as simple as possible, but not simpler.”*

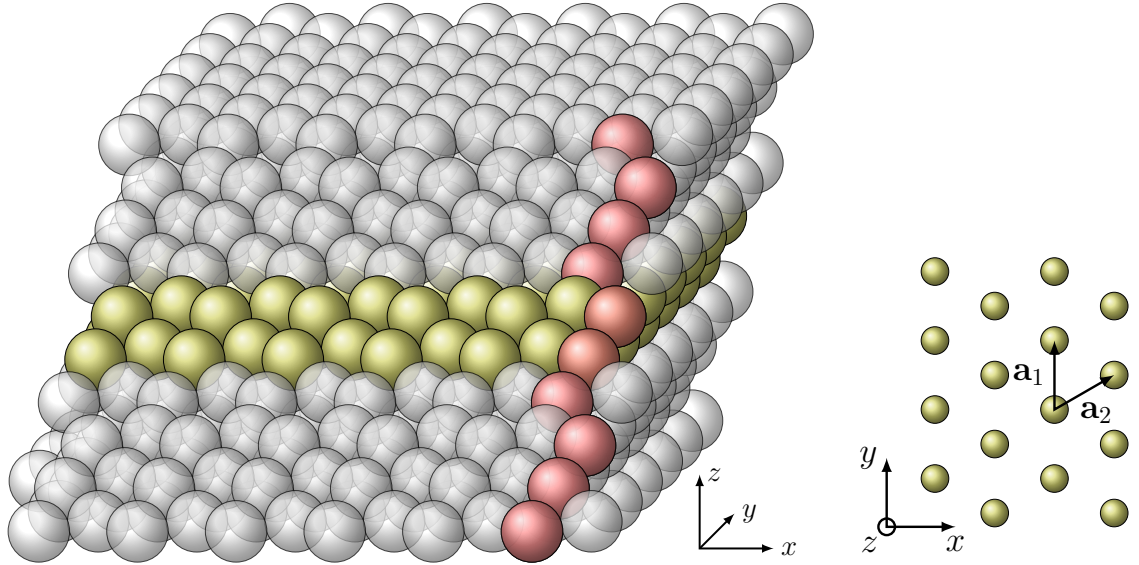
— Albert Einstein

### 3.1. Bismuth Impurities in Noble Metal Films - Colossal Spin Hall Effect

The first part of the results is dedicated to the investigation of the skew-scattering contribution to the spin Hall effect generated by bismuth impurities in thin noble metal films. *Ab initio* methods are used to describe the electronic structure and transport within the semiclassical approach based on the linearized Boltzmann equation. The main ingredients leading to the examination of these systems are the following. On the one hand, the giant spin Hall effect was theoretically predicted [34] and experimentally confirmed [35] for Bi impurities in bulk-like copper systems. On the other hand, experiments [37] and theoretical investigations [H1] showed that the reduced sample thickness can have tremendous influence on the SHE.

Prior to the presentation of the results, I want to substantiate the reliability of the used numerical parameters. It is an important point to find a good balance between a preferably short computation time and well converged results. Based on previous calculations [36] that used the same scheme, I chose to sample the Fermi surface by 420  $\mathbf{k}$  points in the relativistic irreducible part of the two-dimensional Brillouin zone and considered a real space cluster consisting of 55 atoms to simulate the electronic structure of the perturbed (by a bismuth impurity) system. As several test calculations ensured, these parameters lead to considerably converged results. Special attention needs to be paid to the transport Green function since, normally, the imaginary part of the energy, introduced in the context of equation (2.18), has to vanish for its determination. However, this situation would prevent a numerical integration due to emergent poles caused by the host states. Those poles are broadened by a non-vanishing (but desirably small) imaginary part of the energy. Well converged transport results for two-dimensional systems were obtained by a computation of the Green function on a  $3200 \times 3200$   $\mathbf{k}$ -points mesh (3200  $\mathbf{k}$  points along  $\bar{\Gamma} - \bar{M}$  or  $\bar{\Gamma} - \bar{X}$  for (111) or (001) films, respectively) and an imaginary part of the energy of 5.4 meV.

First calculations revealed that it is sufficient to consider systems consisting of 32 monolayers (ML) in order to reliably describe the behavior of thick films. This corresponds to a unit cell composed of 32 host atoms and 8 empty spheres to account for the adjacent vacuum. The impurity density chosen for the films corresponds to



(a) Illustration of a 2 ML fcc (111) film with 4 adjacent layers of empty spheres at top and bottom side. The unit cell consisting of 10 spheres (representing 2 host atoms and 8 vacuum spheres), which is translated on a 2D lattice in the  $x$ - $y$  plane, is shown in red. For simplicity, muffin-tin spheres are displayed.

(b) 2D hexagonal lattice used for the infinite continuation of the unit cell of fcc (111) films in the  $x$ - $y$  plane.

Figure 3.1.: Schematic representation of the construction of the considered ultrathin films.

1 at.% impurity concentration used for bulk crystals that serve as references.

The pictures in figure 3.1 show how the systems under consideration are constructed. The way the metallic film is embedded in the adjacent vacuum spheres in order to take into account charge relaxation, is demonstrated by figure 3.1(a) for a two-monolayer fcc (111) film. Computationally, this structure is formed by the specially reddish marked unit cell which is continued on the corresponding hexagonal 2D lattice formed by the Bravais vectors

$$\mathbf{a}_1 = a \begin{pmatrix} 0 \\ 1 \end{pmatrix} \quad \text{and} \quad \mathbf{a}_2 = \frac{a}{2} \begin{pmatrix} \sqrt{3} \\ 1 \end{pmatrix} \quad (3.1)$$

as depicted in figure 3.1(b). The likewise investigated fcc (001) films are formed by an appropriate unit cell continued on the 2D square lattice built by

$$\mathbf{a}_1 = a \begin{pmatrix} 1 \\ 0 \end{pmatrix} \quad \text{and} \quad \mathbf{a}_2 = a \begin{pmatrix} 0 \\ 1 \end{pmatrix}. \quad (3.2)$$

The first systems investigated during this study were Cu films with (111) surface orientation doped with Bi impurities. For the copper lattice constant the experimental value  $a = 6.8309 \text{ a.u.} = 3.6148 \text{ \AA}$  was chosen. Figure 3.2 shows the results of the evaluated spin Hall angle  $\alpha$  caused by Bi impurities at various positions in the 1, 2, 3, 4, 11, and 32 ML films. The chosen representation requires some comments for a better understanding. First of all, the results related to one and the same film thickness are depicted in the same color. Furthermore, the  $x$ -axis which represents the defect position within the film is normalized to 3 special impurity positions. They are the adatom position (a), where the impurity is located on top

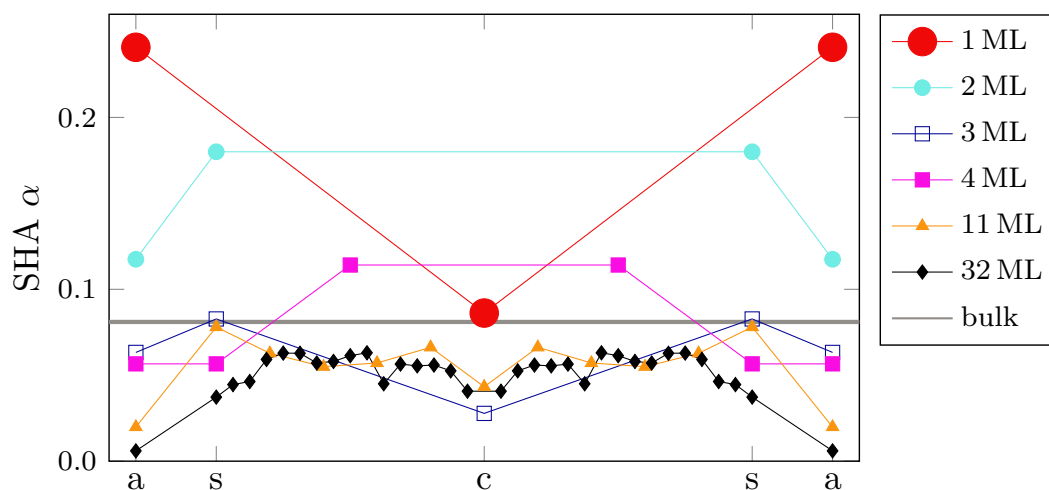


Figure 3.2.: Spin Hall angle  $\alpha$  due to the skew-scattering mechanism induced by Bi impurities at various positions in and on free-standing Cu(111) films consisting of different number of monolayers (ML). The  $x$ -axis is normalized to the adatom (a), surface (s), and central (c) impurity position to facilitate comparisons. Additionally, the value obtained for the corresponding bulk system [34] is included. The lines are to guide the eyes.

of the film, the surface position (s), for which the Bi atom is within the first film layer, and the central position (c), which is uniquely defined for odd-numbered films only. For slabs consisting of an even number of monolayers, both central layers are related to the “c” position. Accordingly, every depicted point in the figure represents the results of a separate system, e.g. an 11 monolayer copper film with a bismuth impurity within the third layer. Consequently and also apparently in the picture, the results are symmetric with respect to the impurity position. Hence, surface and adatom position are present twice.

A first look at figure 3.2 reveals a large difference to the results obtained for Au

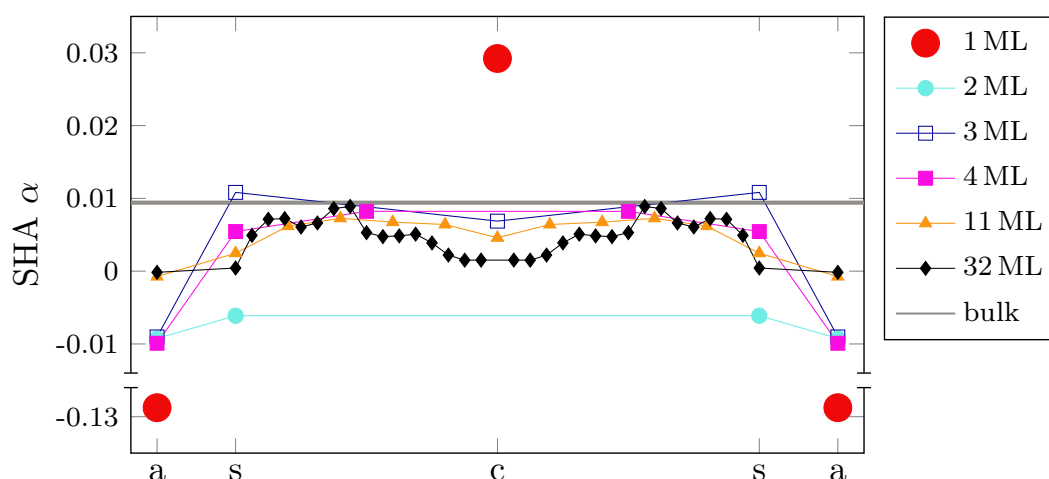


Figure 3.3.: SHA  $\alpha$  due to the skew-scattering mechanism induced by Pt impurities at various positions in and on free-standing Au(111) films consisting of different number of monolayers. The notation is equal to figure 3.2. Results stem from reference [60].

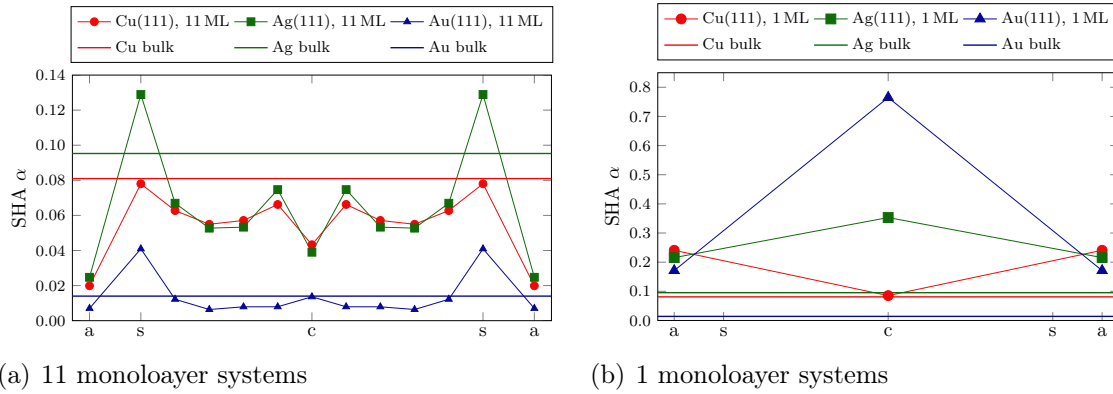


Figure 3.4.: Spin Hall angle  $\alpha$  due to skew scattering induced by Bi impurities in (a) 11 ML or (b) 1 ML Cu, Ag, and Au films with (111) surface orientation. For the purpose of comparison the associated bulk values [88] are shown as horizontal lines in the corresponding colors.

films with Pt impurities [60, H1] with corresponding values depicted in figure 3.3. In particular, Bi adatoms do not change the sign of the corresponding spin Hall angle in comparison to substitutes. On the other hand, similar to Au(Pt) systems, the SHA for ultrathin Cu(Bi) films tend to be larger than for thicker systems. Further on, thick films with Bi impurities in an intermediate position, i.e. between surface and central layer, produce a SHA close to the bulk value. As explained in detail in reference [H1], this behavior is related to the absence of accumulated wave function nodes in this region. Near the boundaries and the film center, the co-occurrence of these nodes lower the scattering rates, enhance the charge conductivity and consequently lead to a decreased spin Hall angle.

Another analogy to the Au(Pt) results is that the largest value for the SHA, which is about 24%, is found for the 1 ML film with Bi adatoms. However, the SHA of about 9% induced by substitutional Bi impurities in the same slab is not the second largest value since it is exceeded by the values of the 2 ML and 4 ML systems with Bi substitutes.

Further opportunities for data analysis can be achieved by the investigation of other host materials as Ag and Au for which the experimental lattice constants  $a_{\text{Ag}} = 7.7227 \text{ a.u.} = 4.0867 \text{ \AA}$  and  $a_{\text{Au}} = 7.7067 \text{ a.u.} = 4.0782 \text{ \AA}$  were chosen. As visible in figure 3.2, normally, there is no enormous quantitative change of the results between 11 ML and 32 ML films. Accordingly, it should be sufficient to study the 11 ML systems in order to make conclusions about thicker ones. The corresponding results are presented in figure 3.4(a). Obviously, the Ag and Au systems show similar features as those based on Cu. Again, the intermediate impurity positions lead to SHAs slightly below the corresponding bulk values. Interestingly, surface impurities induce the largest effect for all considered hosts which can even exceed the related bulk value. Nevertheless, none of the thick systems reaches the value of 24% obtained for the 1 ML Cu film with Bi adatoms. Therefore, the free-standing monolayers were analyzed. Figure 3.4(b) shows some surprising results. As already seen in figure 3.2, Bi atoms substituted in a 1 ML Cu(111) film show a SHA ( $\alpha = 8.6\%$ ) very close to the bulk value of 8.1%. By contrast, the corresponding results for Ag ( $\alpha = 35\%$ ) and Au ( $\alpha = 76\%$ ) are enormously enhanced in comparison to the

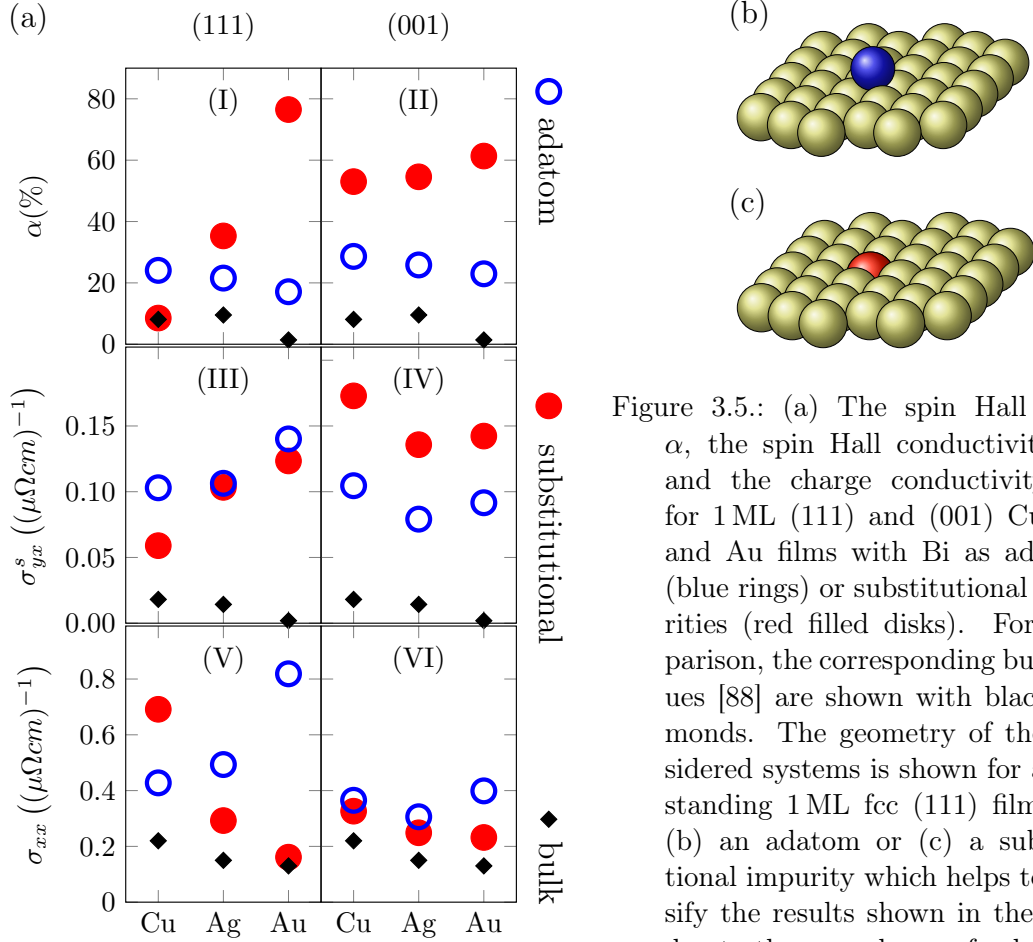


Figure 3.5.: (a) The spin Hall angle  $\alpha$ , the spin Hall conductivity  $\sigma_{yx}^s$  and the charge conductivity  $\sigma_{xx}$  for 1 ML (111) and (001) Cu, Ag, and Au films with Bi as adatoms (blue rings) or substitutional impurities (red filled disks). For comparison, the corresponding bulk values [88] are shown with black diamonds. The geometry of the considered systems is shown for a free-standing 1 ML fcc (111) film with (b) an adatom or (c) a substitutional impurity which helps to classify the results shown in the chart due to the accordance of colors.

related bulk systems with  $\alpha_{\text{Ag bulk}} = 9.5\%$  and  $\alpha_{\text{Au bulk}} = 1.4\%$  [88]. On the other hand, bismuth adatoms on the (111) noble metal films cause relatively similar spin Hall angles of 24% for copper, 21% for silver, and 17% for gold.

A summary of these results for (111) films with either Bi adatoms or substitutes, as shown in figures 3.5(b) and (c), extended by those obtained for the related (001) films can be found in figure 3.5(a) where, for a better analysis of the spin Hall angle, the contributing spin Hall and charge conductivities are depicted as well. Considering figures 3.5(a) (I) - (II) reveals that not only the SHAs for the (111) but also for the (001) films are drastically increased in comparison to the related bulk systems with  $\alpha < 10\%$  [88]. In the same way, most of these values exceed those reported for the corresponding noble metal films with Pt impurities ( $\alpha < 19\%$ ) [H1]. The analysis of the conductivities contributing to the spin Hall angle via equation (1.9) shows that the enhancement of the SHA in comparison to the bulk results is solely determined by the SHC which is strongly increased in all systems, as shown in figures 3.5(a) (III) - (IV). By contrast, the charge conductivity alone would cause a reduction of  $\alpha$  since it is also increased in comparison to the bulk values but enters equation (1.9) in the denominator.

Another striking feature is the strong dependence of the SHA on the host material for substitutional Bi impurities in (111) films, culminating in the nearly 80% value for gold, whereas substitutes in (001) systems as well as adatoms show more or less host-independent results. For the case of substitutional Bi impurities in (111) films,

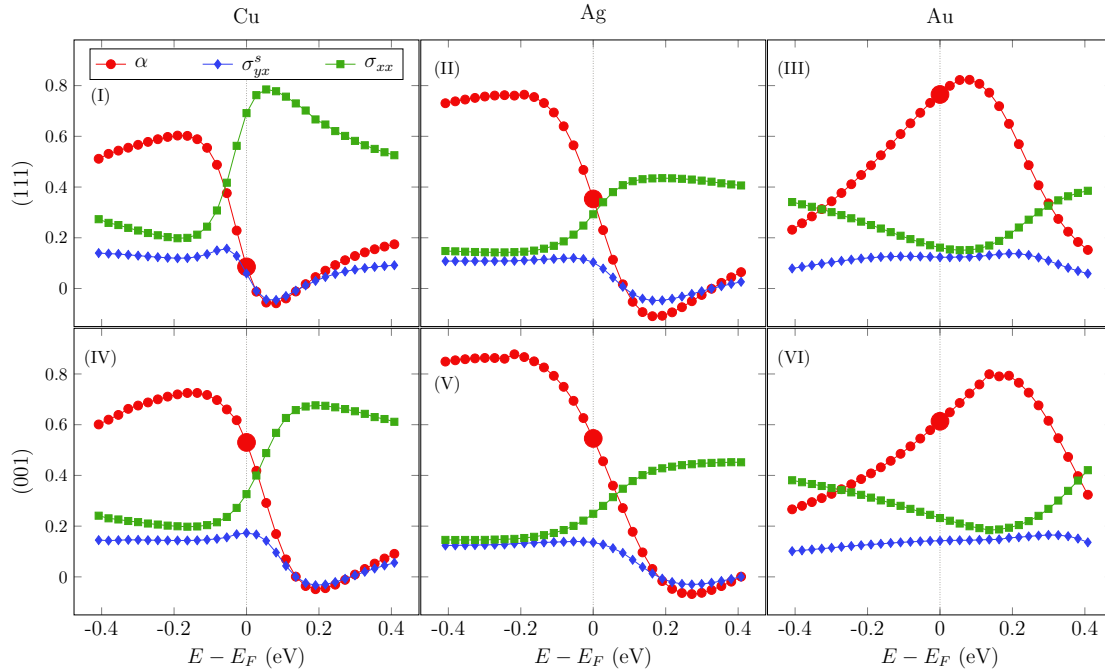


Figure 3.6.: The results of transport calculations performed at different energies around the Fermi level ( $E_F$ ) are shown for 1 ML (111) and (001) Cu, Ag, and Au films with substitutional Bi impurities. The corresponding  $\alpha$  (red filled disks),  $\sigma_{yx}^s$  (blue diamonds), and  $\sigma_{xx}$  (green squares) are displayed and  $\alpha(E_F)$  is highlighted with a larger disk. All quantities have absolute values in the same order of magnitude but different units: the conductivities are given in  $(\mu\Omega cm)^{-1}$ , whereas  $\alpha$  is dimensionless and has to be multiplied by 100 to get the values in percent.

$\sigma_{yx}^s$  and  $\sigma_{xx}$  change in opposite direction going from Cu via Ag to Au (compare figures 3.5(a) (III) and (V)). As a result, both conductivities facilitate to amplify the corresponding SHA shown in figure 3.5(a) (I). However, the influence of the charge conductivity is stronger. While  $\sigma_{xx}$  is reduced by a factor of 4 changing the host from Cu to Au,  $\sigma_{yx}^s$  is increased by about a factor of 2 which leads to the factor of 8 between Bi substitutes in 1 ML Cu(111) and Au(111) films.

For several reasons, the following analysis will focus on substitutional impurities. Firstly, the associated results are mostly the largest ones (with an exception for Cu(111)). Secondly, they have a much stronger dependence on the host material which can help to identify criteria for a large SHA. Furthermore, the colossal SHE in the Au(111) system needs to be understood. Finally, substitutional impurities ought to provide more stable systems and therefore should be more promising for possible practical applications.

In order to get further insights into the underlying mechanisms of the colossal SHE, we investigate the energy dependence of the obtained quantities. The corresponding values for the SHA and its constituents  $\sigma_{yx}^s$  and  $\sigma_{xx}$  are shown in figure 3.6. In all cases,  $\alpha$  is strongly energy dependent.

Analyzing the contributions to the SHA from the charge and spin Hall conductivity separately, one can see differences depending on the host material. While for Au the energy dependence of  $\alpha$  is almost solely determined by the charge conductivity since the related SHC barely changes especially near the Fermi energy,  $\sigma_{yx}^s$  and  $\sigma_{xx}$



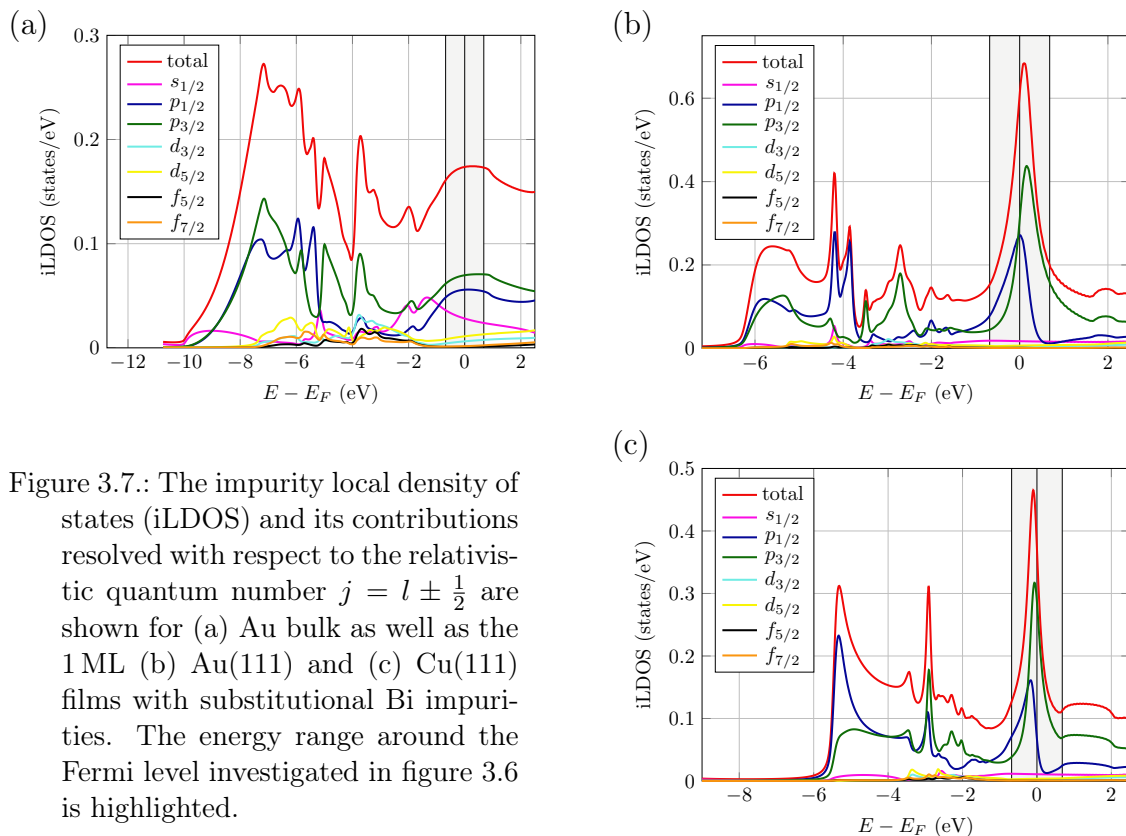
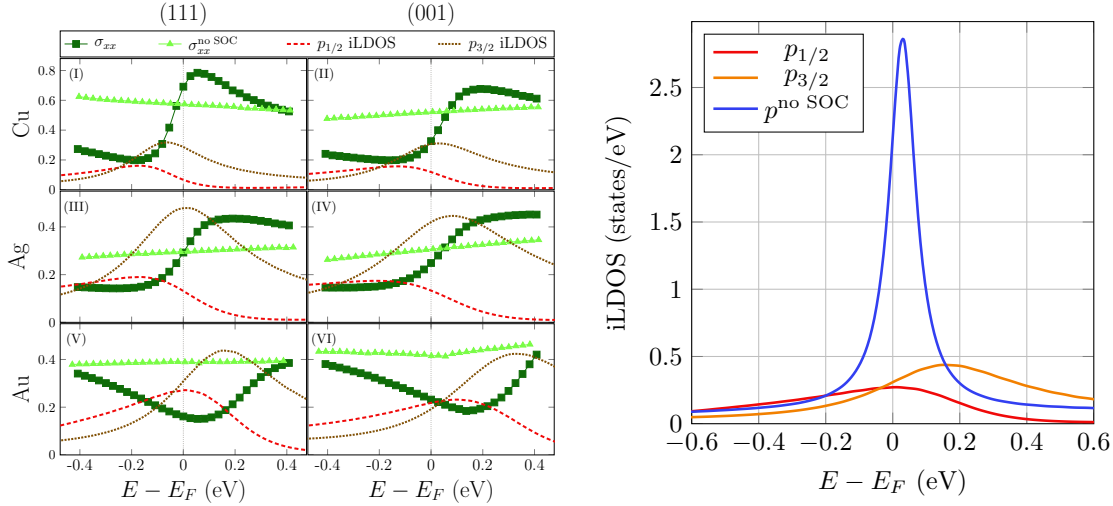


Figure 3.7.: The impurity local density of states (iLDOS) and its contributions resolved with respect to the relativistic quantum number  $j = l \pm \frac{1}{2}$  are shown for (a) Au bulk as well as the 1 ML (b) Au(111) and (c) Cu(111) films with substitutional Bi impurities. The energy range around the Fermi level investigated in figure 3.6 is highlighted.

play a comparable role for Cu and Ag. Nevertheless, a certain correlation between the two conductivities exists for all considered systems. Indeed, the SHC increases with decreasing charge conductivity and vice versa, which is most pronounced for the Ag films. This is related to the fact that, generally, stronger scattering should reduce  $\sigma_{xx}$  but enhance  $\sigma_{yx}^s$  [H1]. However, the situation in real systems can differ from such a simplified picture. For instance, the distinct maximum of the SHA in the Au films is merely determined by the corresponding minimum of the charge conductivity. For both (111) and (001) Au films small changes of energy strongly affect  $\sigma_{xx}$ , whereas  $\sigma_{yx}^s$  remains almost constant. In the case of the 1 ML Au(111) film the minimum of the charge conductivity occurs in the vicinity of the Fermi level which causes the colossal SHA shown in Fig. 3.5(a) (I). Thus, going from bulk Au to the 1 ML Au(111) film, at first the giant SHE occurs since the SHC is increased due to the absence of interband scattering [H1]. Then, the SHA is further enhanced through the suppression of the charge conductivity. These are the ingredients of the obtained colossal SHE.

To elucidate the energy dependence of the charge conductivity further, one needs to recall that the transport properties of dilute noble metal alloys are significantly influenced by the impurity local density of states (iLDOS). Figure 3.7 shows this quantity for Bi impurities in bulk Au as well as 1 ML Au(111) and Cu(111) films together with its decomposition into the relativistic  $j$ -resolved contributions. One can see that the iLDOS of Bi is predominantly provided by the  $p$  states. This is more pronounced in the case of the thin films due to the resonance behavior of the  $p_{1/2}$  and  $p_{3/2}$  channels which is caused by the reduced coordination number of the impurity atom. Consequently, further considerations can be restricted to  $p$  states.



(a) The contributions of the relativistic  $p_{1/2}$  (dashed red) and  $p_{3/2}$  channels (dotted brown) to the impurity local density of states are shown together with the energy-dependent charge conductivity  $\sigma_{xx}$  (green squares) and the corresponding quantity  $\sigma_{xx}^{\text{no SOC}}$  (light green triangles) obtained neglecting spin-orbit coupling effects for 1 ML (111) and (001) Cu, Ag, and Au films with substitutional Bi impurities.

(b) Contributions from  $p$  states to the impurity local density of states for substitutional Bi impurities in a 1 ML Au(111) film including and neglecting SOC effects. While the resonances are split in presence of SOC this is not the case when SOC is absent, where  $p^{\text{no SOC}}$  corresponds to the total impurity density of  $p$  states.

Figure 3.8.: Illustrations related to the influence of  $p$  states and SOC on the charge conductivities of 1 ML films. The conductivities and the iLDOS are plotted in units of  $(\mu\Omega\text{cm})^{-1}$  and (states/eV), respectively.

For a closer look at the correlations between charge conductivity and iLDOS, figure 3.8(a) can be considered. Obviously, the energy dependence of  $\sigma_{xx}$  is correlated with the  $p_{1/2}$  local density of states of the bismuth impurity. For all systems, especially the minimum of the charge conductivity matches the maximum of this iLDOS. On the other hand, the  $p_{3/2}$  iLDOS is not correlated with the conductivity's shape.

Another question is, if it is solely the resonant scattering at the  $p_{1/2}$  impurity states that reduces the charge conductivity. Corresponding results for the charge conductivity neglecting the influence of spin-orbit coupling effects,  $\sigma_{xx}^{\text{no SOC}}$ , can be found in figure 3.8(a) as well. The corresponding procedure of scaling the SOC strength to zero was performed according to the approach of reference [89]. For all considered systems,  $\sigma_{xx}^{\text{no SOC}}$  has a trivial linear dependence as a function of energy. Thus, the found strong change of  $\sigma_{xx}$  with energy is solely provided by the SOC which provides the bismuth's resonant  $p_{1/2}$  states separated from the  $p_{3/2}$  states. Another proof for this statement can be found in figure 3.8(b) where the  $p$  contribution to the iLDOS of Bi is analyzed. The results neglecting and including SOC effects are shown for a 1 ML Au(111) film with Bi substitutes. Obviously, the resonant behavior of states in case of neglected SOC is even enhanced in comparison to the relativistic picture. Nevertheless, the corresponding quantity  $\sigma_{xx}^{\text{no SOC}}$  in figure 3.8(a) (V) shows an almost linear dependence and is not lowered as it is the case if SOC is switched on. Although the influence of the  $p_{1/2}$  iLDOS and SOC on the charge conductivity is ob-

vious, the underlying mechanism is quite complex which can be shown additionally by the following analysis.

The charge conductivity  $\sigma_{xx}$  and the spin Hall conductivity  $\sigma_{yx}^s$  are obtained as components of the related charge and spin conductivity tensors (2.132) and (2.134). Both incorporate the mean free path

$$\Lambda_{\mathbf{k}} = \tau_{\mathbf{k}} \left( \mathbf{v}_{\mathbf{k}} + \sum_{\mathbf{k}'} P_{\mathbf{k}'\mathbf{k}} \Lambda_{\mathbf{k}'} \right) \quad (3.3)$$

which in turn contains the scattering-out term  $\tau_{\mathbf{k}}\mathbf{v}_{\mathbf{k}}$  as well as the scattering-in term  $\tau_{\mathbf{k}} \sum_{\mathbf{k}'} P_{\mathbf{k}'\mathbf{k}} \Lambda_{\mathbf{k}'}$ , where the latter one corresponds to the vertex corrections of the Kubo theory [90].

Equation (3.3) is solved by an iterative scheme [65] proposed originally by Coleridge [91]. In our approach, the (anisotropic) relaxation time approximation (RTA)  $\Lambda_{\mathbf{k}'} = \tau_{\mathbf{k}'}\mathbf{v}_{\mathbf{k}'}$  is used as a starting value. The employed criterion to ensure the convergence of the vector mean free path is

$$\max \left( \frac{|\Lambda_{\mathbf{k}}^N - \Lambda_{\mathbf{k}}^{N-1}|}{|\Lambda_{\mathbf{k}}^{N-1}|} \right) < 0.0001, \quad (3.4)$$

where  $N$  is the number of the last iteration. The executed calculations showed that convergence is typically reached within less than 20 iterations. An advantage of the used computational scheme is that the transport properties of the considered systems can be obtained for an arbitrary number of iterations in order to investigate the influence of the scattering-in term in detail.

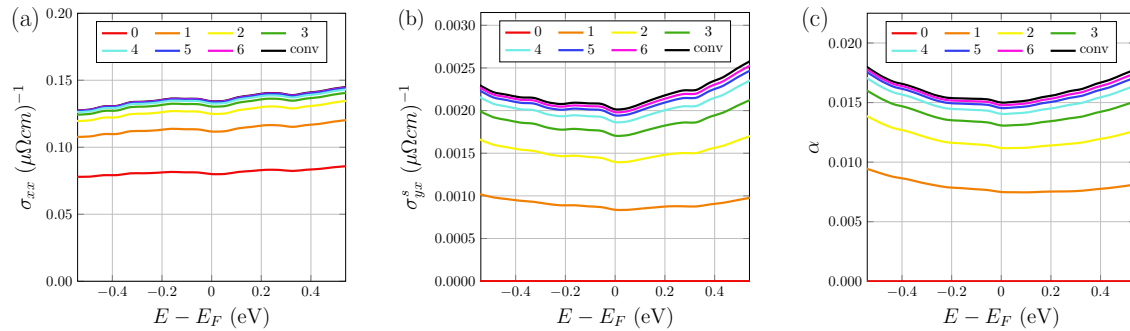
Figure 3.9 presents the corresponding spin Hall angles as well as the charge and spin Hall conductivities for Au bulk as well as 1 ML Au(111) and Cu(111) films. The number of iterations equal to zero corresponds to completely neglecting the scattering-in term in equation (3.3). This provides  $\sigma_{xx}$  within the RTA while  $\sigma_{yx}^s$  completely vanishes in this case since it is solely caused by the scattering-in term [82] and at least one iteration is required to obtain a non-vanishing value.

For the bulk system, the energy-dependent curve shapes for the presented quantities are practically unchanged during the iterations. This property is strongly correlated with the flat Bi iLDOS in the investigated energy region visible in figure 3.7(a). In this way, RTA and first iteration give quite reasonable results.

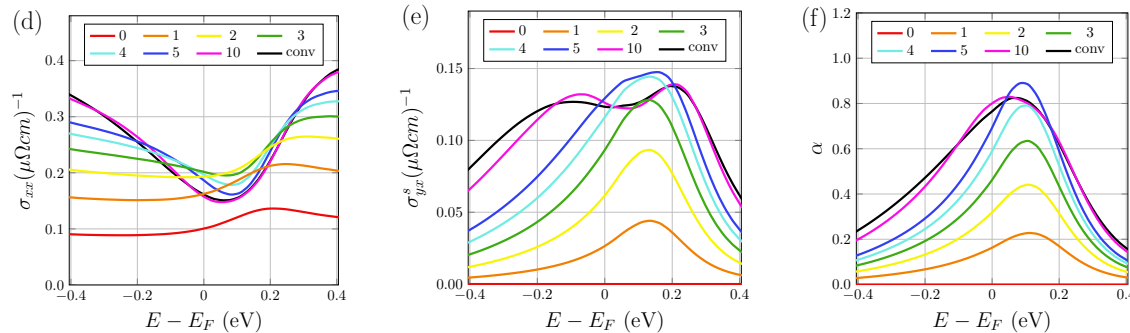
The situation for the films is rather different. Namely, the energy dependence of the considered quantities is strongly modified during the iteration process due to the well-pronounced peaks of the impurity LDOS near  $E_F$  (compare figures 3.7(b) and 3.7(c)). Therefore, neither the RTA for  $\sigma_{xx}$  nor the first iteration for  $\sigma_{yx}^s$  satisfactorily provide at least the correct curve shape.

These results show that the correct description of ultrathin films as investigated here requires the employment of the complete computational scheme based on the first-principles calculations. Consequently, it is difficult to describe the obtained colossal SHE with simple considerations like the phase shift model, which will be investigated later in sections 3.2 and 3.3. There, the charge conductivity and the spin Hall conductivity are obtained within the RTA and the first iteration, respectively, which is an appropriate treatment for the considered bulk systems.

## Au bulk



## Au(111) film



## Cu(111) film

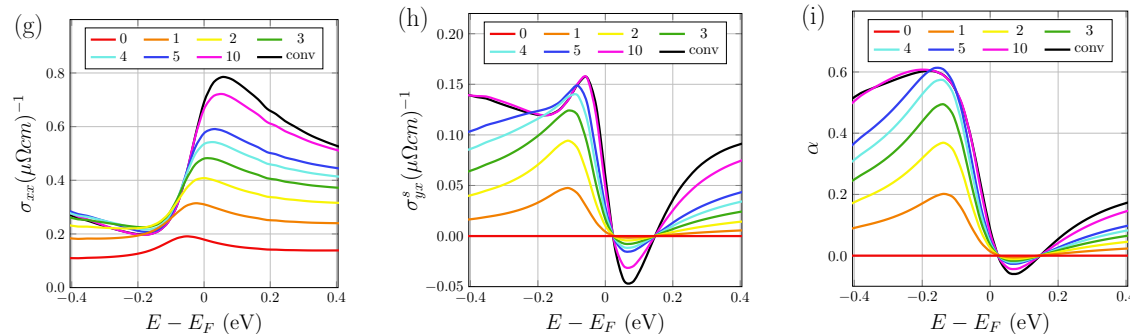


Figure 3.9.: The longitudinal conductivity  $\sigma_{xx}$ , the spin Hall conductivity  $\sigma_{yx}^s$ , and the spin Hall angle  $\alpha$  as functions of energy for various numbers of iterations executed for solving equation (3.3) are shown for Au bulk as well as the 1 ML Au(111) and Cu(111) films with substitutional Bi impurities. Here, “conv” means the converged results.

Although a simple picture for a fundamental explanation cannot be provided, it is possible to summarize the above consideration by stating that the strong influence of the scattering-in term on the energy dependence of the conductivities is definitely related to the  $p_{1/2}$  resonance states.

Having this microscopic picture in mind, the host dependence of  $\alpha$  for the two surface orientations can be understood. As can be seen in figure 3.6, there are extreme similarities in the general energy dependence  $\alpha(E)$  between (001) and (111) films for each host material, separately. However, the coordination number for (001) films is reduced in comparison to the (111) systems. The accompanied smaller charge density leads to a lowered Fermi energy. As a result, the related impurity

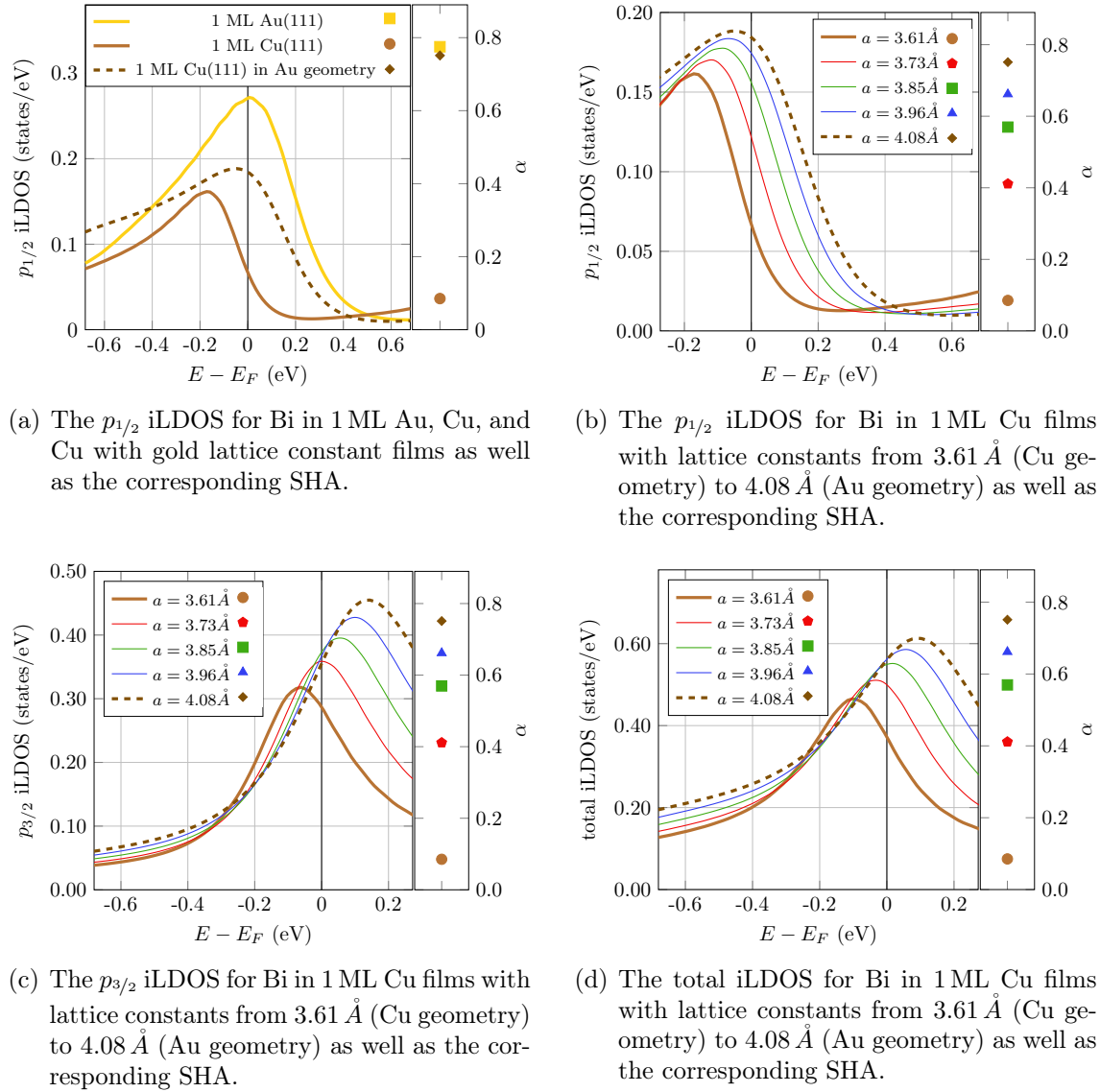


Figure 3.10.: Various  $p$  impurity local density of states at a substitutional Bi impurity atom in different 1 ML fcc (111) films with diverse lattice constants are shown together with the corresponding spin Hall angle calculated at  $E_F$ .

resonances of the (001) films are shifted to higher energies with respect to the Fermi level. In agreement with the discussion above, the conductivity minimum is shifted accordingly. Additionally,  $\sigma_{xx}$  changes strongly at energies around  $E_F$  which in turn causes strong variations of  $\alpha$ . Thus, it is somewhat accidental that the SHA shown in figure 3.5(a) is nearly the same for the (001) films, whereas it varies strongly for the (111) films. A Fermi level shift for the (001) films to slightly higher energies would simulate the situation of the (111) surface orientation.

This knowledge can be employed to optimize the SHA. The aim is to fix the  $p_{1/2}$  impurity resonance at the Fermi level. A possible opportunity for this resonance shift is strain engineering of the film grown on an appropriate substrate. This assumption is going to be investigated using the example of the Cu(111) film since it shows the smallest SHA among all the considered systems, which can be seen in figure 3.5(a)

(I) - (II). According to figure 3.8(a) (I), the peak of the corresponding  $p_{1/2}$  impurity LDOS is below  $E_F$ . Following the discussion above, one can assume that a shift of the impurity resonance towards the Fermi level can be achieved by an increase of the host lattice constant.

Figure 3.10(a) shows that the desired condition can be fulfilled if the lattice constant of Au is used for the hypothetically strained Cu(111) film. The increase of the lattice constant by about 13% from  $a_{\text{Cu}} = 3.6148 \text{ \AA}$  to  $a_{\text{Au}} = 4.0782 \text{ \AA}$  shifts the maximum of the  $p_{1/2}$  impurity LDOS close to  $E_F$  as in the case of the Au film. This in turn leads to the colossal SHA, as shown in the right part of figure 3.10(a). Of course, the considered change of the lattice constant is quite strong. That is why additional calculations for three 1 ML systems with lattice constants between  $a_{\text{Cu}}$  and  $a_{\text{Au}}$  were executed. The related results for  $p_{1/2}$ ,  $p_{3/2}$ , and total Bi iLDOS as well as the resulting SHA can be found in figures 3.10(b) - (d). As expected, there is a gradual change of both, the impurity LDOS and  $\alpha$ . It is worth mentioning that already an increase of the lattice constant by about 3% leads to an enhancement of  $\alpha$  from below 10% to slightly above 40%. Thus, already quite small changes of the lattice constant can have strong effects on the SHE by reason of the large slope of  $\sigma_{xx}(E)$  slightly below the Fermi level, as visible in figures 3.6 (I) and 3.8(a) (I). Additionally, these results support the fact, that the  $p_{1/2}$  iLDOS is strongly correlated with the magnitude of the SHA. Following the corresponding results in figure 3.10(b) one can identify that the iLDOS at the Fermi level increases similarly to the SHA. By contrast, the  $p_{3/2}$  iLDOS at  $E_F$  in figure 3.10(c) is almost unchanged for four of the analyzed systems. In addition, the films with  $a = 3.96 \text{ \AA}$  and  $a = 4.08 \text{ \AA}$  offer identical total iLDOS displayed in figure 3.10(d) although the SHA is obviously different.

The presented modification of the lattice constant of the host in order to maximize the  $p_{1/2}$  iLDOS at the Fermi level illustrated by the obtained results indicates a new route to design materials with large spin Hall angle. Nonetheless, free-standing 1 ML films considered in this study are quite artificial from the practical point of view. Hence, a substrate is needed in order to have more realistic systems for the observation of the colossal SHE. For this aim, insulating substrates seem to be most reasonable choice in order to provide the required conditions discussed above. On the one hand, an appropriate material can enforce the aforementioned strain (or constriction). On the other hand, induced electrostatic forces can also affect the relative position of the Fermi level with respect to the impurity states.

However, there is also a possible undesirable influence of a substrate. The considered skew-scattering mechanism is strongest for host electron spins pointing out of plane, while the Rashba-type SOC induced by a substrate would force them to be oriented within the film plane. In order to ensure the desired spin orientation, a symmetric quantum well structure *insulator/metal film/insulator* could be utilized.

It is important to mention that the presence of the Rashba-type SOC would lead to an additional spin Hall current also polarized in the  $z$  direction [92, 93]. An estimation of the size of the spin Hall conductivity due to the so-called interfacial spin-orbit coupling (ISOC) can be performed according to equation (6) of reference [92] as

$$\sigma_{\text{ISOC}} = \frac{e}{8\pi^2} k_F. \quad (3.5)$$

A transformation into the units used during this thesis can be performed with the help of the prefactor  $(e/\hbar)$ . Using the reasonable value  $k_F = 1.36 \text{ \AA}^{-1}$  for Cu [92] leads to about  $4 \cdot 10^{-4} (\mu\Omega\text{cm})^{-1}$ . Obviously, the effect due to the Rashba-type SOC provides a contribution two orders of magnitude smaller than for the corresponding SHC shown in figure 3.5(a).

---

## 3.2. Analysis of the Giant Spin Hall Effect in Cu(Bi) Alloys

In this part of the results, I will concentrate on the analysis of the giant spin Hall effect predicted [34, 88], observed [35], and further investigated [94, H2] for Cu(Bi) alloys.

In the context of a screening among various host and impurity combinations, Gradhand et al. [34, 88] pointed out that the Cu(Bi) alloy would be worth investigated experimentally since the *ab initio* method, which is essentially the same as the one utilized in the present work, forecast the large spin Hall angle of 8.1%. Since this value was of the order of the giant SHA ( $\alpha \approx 11\%$ ) measured for Au by Seki et al. [30], the largest magnitude reported at that time, it naturally attracted a lot of attention.

Consequently, the group of Yoshichika Otani conducted experiments using the inverse SHE for such alloys and reported a SHA of  $-24\%$ , ascribing it to skew scattering at Bi impurities in Cu [35]. Besides the measured magnitude, larger by a factor of three in comparison to Gradhand's prediction, it was the opposite sign which initiated a hot debate. In order to clarify this discrepancy, several aspects which possibly could have solved this problem were investigated. Although the final solution is now known to be much simpler, only the arguments considered in what follows helped to unravel the mystery. Additionally, these discussions give further insights into the topic and can help theoreticians and experimentalists to pay more attention when comparing their results.

The sign of the SHA is a subtle point since different sign conventions for the spin Hall conductivity are used in the literature. This complicates a comparison between various approaches. One definition uses the SHC in units of the charge conductivity with the corresponding prefactor of  $e^2$  as in references [34, 38, 67, 82] which rely on the semiclassical theory. Its advantage is the coherent treatment of spin and charge conductivities providing the dimensionless spin Hall angle as their ratio. In addition, for materials like copper with spin expectation values of the Bloch states close to 1 (in units of  $\hbar/2$ ), the two-current model presented in the introduction can be employed. Accordingly, the charge and spin Hall current densities are given by

$$j_x = j_x^+ + j_x^- = \sigma_{xx} E_x = (\sigma_{xx}^+ + \sigma_{xx}^-) E_x \quad (3.6)$$

and

$$j_y^s = j_y^+ - j_y^- = \sigma_{yx}^s E_x = (\sigma_{yx}^+ - \sigma_{yx}^-) E_x, \quad (3.7)$$

respectively. Although this approach appears natural within the semiclassical theory, the most common definition is related to the Kubo theory [93, 95, 96]. Here, the SHC has the prefactor of  $(-e)(\hbar/2)$  replacing the electron charge  $(-e)$  by the spin units  $\hbar/2$ . Such a definition provides opposite sign in comparison to the first one. Finally, one can use the SHC expressed in units of the charge conductivity but keeping the sign from the common definition of the Kubo formula [93, 95, 96]. This was done in reference [33] exploiting the Kubo-Středa approach.

Throughout this thesis, the used SHC coincides with  $\sigma_{yx}^s$  of references [34, 82],  $\sigma_{xy}^s$  of reference [33], and  $\frac{2e}{\hbar} \sigma_{xy}^s$  of references [93, 95, 96]. Taking into account that for



the systems with both time and space inversion symmetry the relation  $\sigma_{xy}^s = -\sigma_{yx}^s$  is valid, a consistent comparison of different approaches becomes possible. Clearly, the sign of the SHC determines the sign of the spin Hall angle given by equation (1.9) since the charge conductivity is a positive quantity.

After this clarification which should circumvent any sign issues due to different definitions, a consistent comparison between various experimental and theoretical results is possible. Niimi et al. [35] also reported results for the Cu(Ir) alloy and pure Pt in comparison to the problematic case of the Cu(Bi) alloy. It is commonly assumed that the SHE in Pt is related to the intrinsic mechanism since reproducible experimental results are in good agreement with theoretical predictions [33, 75]. The *ab initio* calculations confirm in particular the sign of the corresponding  $\sigma_{yx}^s$ . Moreover, the extrinsic contribution was shown to be small for platinum [33, 97]. Agreement between experiment and theory is also obtained for the Cu(Ir) alloy. Considering the skew-scattering mechanism,  $\alpha = 0.035$  and  $\alpha = 0.029$  were obtained from the Boltzmann equation and the Kubo-Středa formula, respectively [H2]. The recent experimental value is  $\alpha = 0.021 \pm 0.006$  [98] which is in good agreement with  $\alpha = 0.026$  measured for this alloy by Fert et al. [67] already in 1981. For Cu(Ir), both charge and spin resistivity show almost perfect linear dependence on the impurity concentration up to 12 at.% [35, 98] which indicates the dominance of the skew-scattering mechanism. By contrast, for the Cu(Bi) alloy the experimental results deviate from the linear dependence above 0.5 at.% impurity concentration [35]. To handle this problem, lower concentrations were chosen for the measurement which led to a negative SHA of  $-0.24$  in contradiction to first-principles calculations. To clarify this issue, a detailed analysis of existing as well as new *ab initio* results were performed [H2] in comparison to the experiment. Furthermore, the phase shift model based on relativistic phase shifts and introduced in section 2.4.2, which generalizes the resonant scattering model of reference [35] adapted from the approach of Fert and Levy [38], was employed. Among others, this model is used to simulate the scattering conditions needed to reproduce the experimental data. The formula used by Niimi et al. [35]

$$\alpha_H = \frac{-2 \sin \eta_0 \{ \sin \eta_{1/2} \sin(\eta_{1/2} - \eta_0) - \sin \eta_{3/2} \sin(\eta_{3/2} - \eta_0) \}}{3(\sin^2 \eta_0 + \sin^2 \eta_{1/2} + 2 \sin^2 \eta_{3/2})} \quad (3.8)$$

incorporates relativistic phase shifts  $\eta_0$ ,  $\eta_{1/2}$  and  $\eta_{3/2}$  which are related to  $s$  ( $l = 0$ ) and  $p$  ( $l = 1$ ) electrons. In the notation used in this thesis, they are identical to  $\delta_{1/2}^s$ ,  $\delta_{1/2}^p$ , and  $\delta_{3/2}^p$  where the connection to  $s$  and  $p$  states is written explicitly to prevent intermixing of states with different  $l$  but same  $j$ .

In order to derive such formula from the equations given in section 2.4.2, it is necessary to skip all terms with  $l > 1$ , assuming they are negligible for the scattering at bismuth impurities. Then, from equations (2.184), (2.164), and (2.187) one can obtain

$$\alpha = \frac{\sigma_{yx}^+}{\sigma_{xx}^+} = \frac{2 \sin \delta_{1/2}^s [\sin \delta_{1/2}^p \sin(\delta_{1/2}^p - \delta_{1/2}^s) - \sin \delta_{3/2}^p \sin(\delta_{3/2}^p - \delta_{1/2}^s)]}{3(\sin^2 \delta_{1/2}^s + \sin^2 \delta_{1/2}^p + 2 \sin^2 \delta_{3/2}^p)}. \quad (3.9)$$

Obviously, equation (3.9) is equivalent to (3.8) but has opposite sign. The origin of this discrepancy arises from the scattering-in term of the Boltzmann equation. In the

present work, the scattering-in term is used according to Kohn and Luttinger [66] as  $\sum_{\mathbf{k}'} P_{\mathbf{k}' \rightarrow \mathbf{k}} g_{\mathbf{k}'}$ . By contrast, equation (3.8) was based on an erroneous scattering-in term written as  $\sum_{\mathbf{k}'} P_{\mathbf{k} \rightarrow \mathbf{k}'} g_{\mathbf{k}'}$  [99, 100]. In the non-relativistic case the reversibility relation  $P_{\mathbf{k}' \rightarrow \mathbf{k}} = P_{\mathbf{k} \rightarrow \mathbf{k}'}$  holds. However, the presence of the SOC leads to  $P_{\mathbf{k}' \rightarrow \mathbf{k}} \neq P_{\mathbf{k} \rightarrow \mathbf{k}'}$  and  $P_{\mathbf{k}' \rightarrow \mathbf{k}}^{\text{antisym}} = -P_{\mathbf{k} \rightarrow \mathbf{k}'}^{\text{antisym}}$  which causes opposite sign in the SHA evident from equations (2.106) and (2.167).

The impurity phase shifts used to calculate the SHA by means of equation (3.9) were obtained according to equation (2.84). For a Bi atom embedded in Cu bulk, they are the following

$$\delta_{1/2}^s = 0.94 \quad \delta_{1/2}^p = 1.32 \quad \delta_{3/2}^p = 0.79. \quad (3.10)$$

Levy et al. [94] obtained the values

$$\eta_0 = 1.46 \quad \eta_{1/2} = 1.17 \quad \eta_{3/2} = 0.72 \quad (3.11)$$

by a different method employing Friedel's sum rule. Accordingly, the  $l$ -dependent scattering phase shifts are proportional to the number of electrons with corresponding angular momentum. For the investigated system, the equations

$$\eta_0 = \pi(Z_s^{\text{Bi}} - Z_s^{\text{Cu}})/2, \quad \eta_{1/2} = \pi(Z_{1/2}^{\text{Bi}} - Z_{1/2}^{\text{Cu}})/2, \quad \eta_{3/2} = \pi(Z_{3/2}^{\text{Bi}} - Z_{3/2}^{\text{Cu}})/4 \quad (3.12)$$

were used, where  $Z_j^{\text{Bi}}$  and  $Z_j^{\text{Cu}}$  represent the charge on the Bi impurity and the host atoms, respectively. The quantities  $Z_j$  are evaluated as the integrated DOS at the Fermi level. Besides this diverse approach for the estimation of the phase shifts, the *ab initio* method to determine the electronic structure and consequently the DOS differs as well. Namely, Quantum ESPRESSO calculations using pseudopotentials based on the generalized gradient approximation (GGA) were performed in reference [94]. Although the approaches are quite different, the results for the  $p$  phase shifts are similar. However, the  $s$  phase shifts do not agree. Especially this discrepancy leads to the different absolute values of the SHA obtained by Niimi et al. [35] and Levy et al. [94] in comparison to the ones obtained here [H2]. While the phase

Table 3.1.: The relative extension of the distances from Bi and Ir impurities to the nearest neighbors (NN) and the next-nearest neighbors (NNN) in a Cu host, as obtained within both the local density approximation and the generalized gradient approximation for the exchange-correlation potential ( $V_{\text{xc}}$ ). The experimental lattice constant of Cu is  $a_{\text{exp.}} = 3.6149 \text{ \AA}$ , while the theoretical values ( $a_{\text{theory}}$ ) are  $3.5228 \text{ \AA}$  and  $3.6394 \text{ \AA}$  for LDA and GGA, respectively.

$V_{\text{xc}}$	LDA		GGA	
	$a_{\text{theory}}$	$a_{\text{exp.}}$	$a_{\text{theory}}$	$a_{\text{exp.}}$
Lattice constant				
NN to Bi	5.40%	6.07%	5.52%	5.33%
NNN to Bi	0.48%	0.61%	0.47%	0.44%
NN to Ir	1.44%	0.94%	0.97%	1.14%
NNN to Ir	0.20%	0.30%	0.27%	0.25%

shifts (3.11) introduced in equation (3.8) lead to  $\alpha = -0.043$ , the combination of (3.10) and equation (3.9) results in  $\alpha = 0.096$ .

Another point related to the spin Hall effect in the Cu(Bi) alloy is structural relaxation of the host atoms next to the impurity, which was neglected in former first-principles studies [33, 34, 82]. Therefore, besides charge relaxation, lattice relaxation will be investigated in order to clarify its influence on the spin Hall effect. The results related to geometry relaxation were obtained using the Vienna *Ab initio* Simulation Package (VASP) [101]. The electron-ion interactions are represented by the projector-augmented wave (PAW) pseudopotential [102] and the electronic wave functions expanded as plane waves with the cutoff energy of 450 eV. The corresponding system was simulated with a 108-atom supercell and the relaxation was performed until the forces were less than  $5 \cdot 10^{-3}$  eV/Å. The results for Bi and Ir impurities in a Cu host can be found in table 3.1. Obviously, the structural relaxation found for the Bi impurity is much stronger in comparison to the Ir impurity. Therefore, one could assume that the discrepancy between theory and experiment for the Cu(Bi) alloy, in contrast to a good agreement obtained for the Cu(Ir) alloy, is caused by this effect. In order to perform transport calculations for the Cu(Bi) alloy, the structural relaxation for the next-nearest neighbors was neglected and the averaged (over the row) value of 5.6% for the nearest neighbors was used. The phase shifts corresponding to this geometry are obtained as

$$\delta_{1/2}^s = 0.95 \quad \delta_{1/2}^p = 1.39 \quad \delta_{3/2}^p = 0.89. \quad (3.13)$$

Table 3.2 contains the results for the skew-scattering contribution to the SHA of the Cu(Bi) alloy obtained from various approaches. The values from first-principles calculations are shown in comparison to the results of equation (3.9) based on the spherical band approximation. Obviously, both approaches lead to similar results. The inclusion of contributions from *d* and *f* electrons in equations (2.184) and (2.187) results in almost the same value of 0.095. These findings confirm the assumption of reference [35], that the dominant scattering process in the Cu(Bi) alloy is related to *p* electrons. Additionally, this is in agreement with reference [34]. There, it was highlighted that the spin-orbit driven scattering at Bi impurities is particularly high for *p* electrons. Furthermore, reasonable agreement between the results obtained by the Boltzmann equation and the Kubo-Středa formula can be demonstrated by

Table 3.2.: The skew-scattering contribution to the spin Hall angle  $\alpha$  for the dilute Cu(Bi) alloy calculated by means of the semiclassical and quantum-mechanical *ab initio* approaches as well as within the spherical band approximation. Here, the values for the “relaxed” case are obtained including structural relaxation around the impurity atom.

Theory	$\alpha$	$\alpha$ (relaxed)
Phase-shift model, equation (3.9)	0.096	0.089
Boltzmann equation	0.081	0.063
Kubo-Středa formula	0.127	-
Experiment [35]	-0.24	-

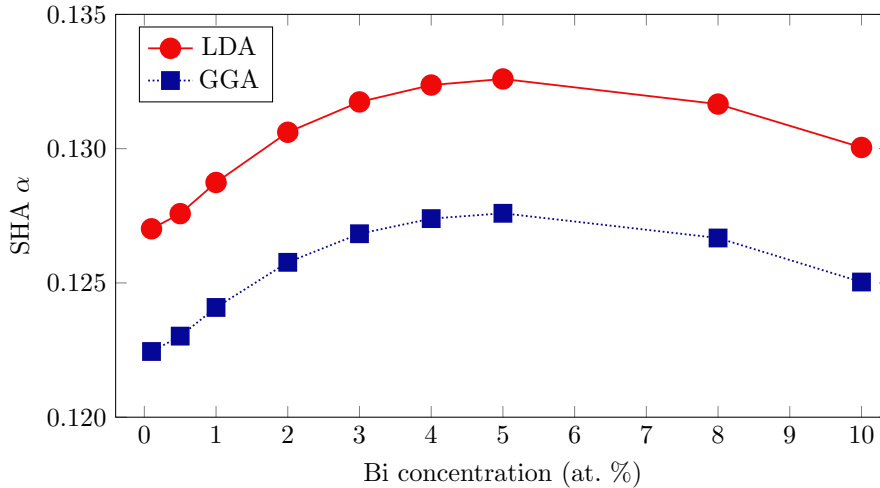


Figure 3.11.: The spin Hall angle for the Cu(Bi) alloy with different impurity concentrations obtained from the Kubo-Středa formula using both the local-density approximation (LDA) and the generalized gradient approximation (GGA) for the exchange-correlation potential.

table 3.2 as well. Nevertheless, the analysis carried out here cannot describe the experimental data, since the structural relaxation around the impurity leads to a relative reduction of the SHA by  $\sim 20\%$  only. Especially, the sign of all displayed results for the spin Hall angle from theory shows up to be positive.

Besides the conventional skew-scattering contribution, the intrinsic and side-jump mechanisms are other options for a possible explanation of the discrepancy between theory and experiment. For that reason, the Kubo-Středa formula was used<sup>2</sup> to perform corresponding calculations for Cu(Bi) alloys with different impurity concentrations. Figure 3.11 shows the results for the SHA including the intrinsic, side-jump, and skew-scattering contribution. In order to prove the validity of the local density approximation, the corresponding results based on the generalized gradient approximation for the exchange-correlation potential are obtained and shown as well. One can see that the sign of the total spin Hall angle is positive for the whole range of the impurity concentrations analyzed in the experiment of Niimi et al. [35]. Altogether this demonstrates that the sign of the measured SHA cannot be explained by spin-orbit driven scattering at substitutional Bi impurities randomly distributed in bulk Cu. Additionally, as shown in section 3.1, the corresponding investigations for thin and ultrathin films cannot account for the experimental results since solely positive values are predicted.

Thus, state-of-the-art *ab initio* calculations for the skew-scattering contribution to the SHA in dilute Cu(Bi) alloys neither for 3D nor for 2D systems can explain the existing experimental data. However, the considered model allows to simulate the dependence of the SHA on scattering properties by a variation of the corresponding phase shifts. Figure 3.12 shows  $\alpha$  depending on the phase shifts involved in equation

<sup>2</sup>The corresponding results were obtained in collaboration with the group of Hubert Ebert in Munich.

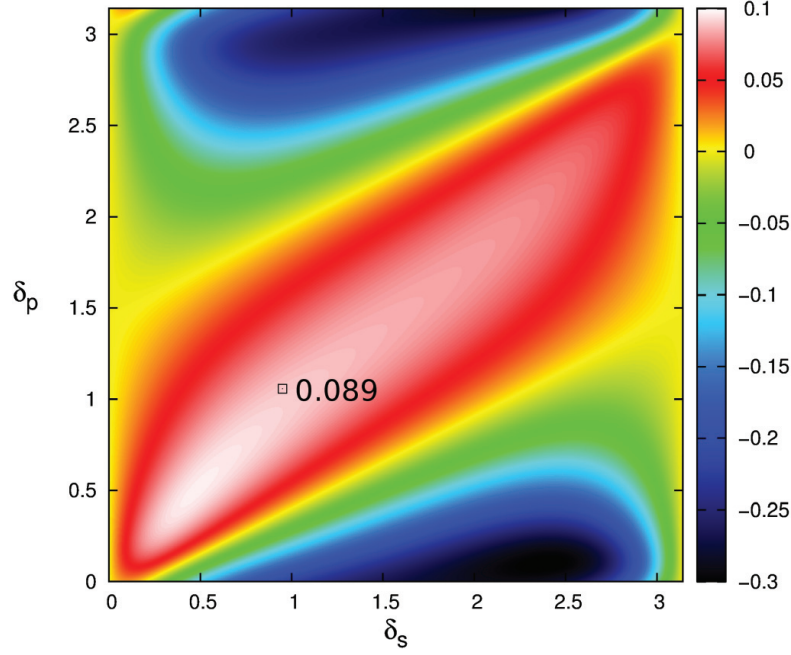


Figure 3.12.: The dependence of the spin Hall angle given by equation (3.9) on the  $s$  and  $p$  scattering phase shifts  $\delta^s = \delta_{1/2}^s$  and  $\delta_p = \frac{1}{3}(\delta_{1/2}^p + 2\delta_{3/2}^p)$  is shown for the relaxed geometry together with the corresponding value of  $\alpha$  from table 3.2 at the position given by equation (3.13).

(3.9). Namely, the difference between the two  $p$  phase shifts

$$\delta_{1/2}^p - \delta_{3/2}^p = 0.50, \quad (3.14)$$

as obtained from the first-principles calculations for the relaxed geometry (see equation (3.13)), was fixed and  $\delta_{1/2}^s$  as well as  $\delta_p = \frac{1}{3}(\delta_{1/2}^p + 2\delta_{3/2}^p)$  were varied in the range between 0 and  $\pi$ . The SHA related to the *ab initio* phase shifts is situated in a stable positive region. However, certain combinations of the phase shifts can deliver the experimental result with  $\alpha = -0.24$ . Besides the dependence on the averaged  $p$  phase shift, it is worth to investigate a variation of the spin-orbit splitting  $\delta_{1/2}^p - \delta_{3/2}^p$  which can be caused by electron correlation effects, as proposed in reference [37]. Nevertheless, even with this procedure, the results of the phase-shift model for the Cu(Bi) alloy, whether relaxed or unrelaxed, remain stable with respect to the sign of the SHA for the full parameter space [H2]. Therefore, only a significant modification of the potential scattering properties could provide agreement between theory and experiment. This probably points to the existence of other scattering centers in the Cu(Bi) samples than just randomly distributed substitutional Bi impurities. Taking this into account, impurity cluster formation can play an important role and is not considered in theory yet. In their experiment, Niimi et al. showed [35] that Bi atoms start to segregate at the interface at impurity concentrations above 0.5 at.%. That is why they restricted the analysis for the extraction of the skew-scattering contribution from experimental data to lower concentrations where a linear relation between the impurity concentration and the resistivity of the studied films was observed. In this regime it was assumed that Bi impurities are randomly distributed

without short-range ordering although the formation of extremely small clusters such as dimers or trimers down to lowest impurity concentrations could not be excluded. In comparison to single substitutional Bi impurities, remarkable changes of the scattering properties along with a potentially strong impact on the SHE can be expected for such cluster formations. In addition, the existence of rough interfaces and grain boundaries in the films can cause extra scattering or can force the impurities to accumulate there which would change the scattering properties as well. However, the description of these cases together with the extension of the present theoretical approaches goes beyond the intention of this thesis.

After all these considerations have been published [H2], an important erratum related to reference [38] was released [100]. Besides the already mentioned usage of the wrong scattering-in term, which conspired with another sign error, the authors stated that the experimental results for Ir in Cu from reference [98] were obtained for the  $y$ - $x$  component of the resistivity tensor  $\rho_{yx}$ . However, the other considerations were for  $\rho_{xy}$ , which has the same sign as  $\sigma_{yx}$ . Consequently, the results for Cu(Bi) published by the same experimentalists were for the opposite tensor component as well. In this way, the different sign between the various approaches for the Cu(Bi) alloy was due to the formulation of the SHA in terms of either conductivities or resistivities

$$\alpha(\sigma) = \frac{\sigma_{yx}}{\sigma_{xx}} \stackrel{!}{=} \frac{\rho_{xy}}{\rho_{xx}} = -\frac{\rho_{yx}}{\rho_{xx}} = -\alpha(\rho), \quad (3.15)$$

as pointed out explicitly by Gu et al. [103]. In the subsequent publication related to the Cu(Bi) issue, Levy et al. [94] state explicitly that equation (3.8) is derived on the basis of  $\rho_{yx}$ . Nevertheless, the obtained agreement with respect to the Bi results opened the problem of contradictory results for Ir in Cu. Regarding the results for  $\sigma_{yx}$ , experiments from Niimi et al. [98] predict negative values. Since the results obtained employing the resonant scattering model by Fert and Levy [38] were fitted to the experimental values, they stated that the sign of the free (in their consideration) parameter  $\eta_1$  has to be changed. Additionally, the disagreement with the positive values published by Fert et al. in 1981 [67] needs to be understood. Although it was explicitly stated that the  $x$ - $y$  component of the resistivity tensor is considered, the used definition  $\rho_{xy} = E_y/j_x$  corresponds to  $\rho_{yx}$  in the framework used here. Accordingly, all these results are in good agreement among each other, especially with respect to the sign.

The last missing piece in the puzzle is related to the theoretical predictions for Cu(Ir) from *ab initio* treatments. All the corresponding calculations, including the extended phase shift model discussed in section 3.3, forecast positive spin Hall angles [H3]. Nevertheless, in contrast to Bi, Ir impurities in Cu lead to a quite small SHA. Thus, already slight variations in the electronic structure of the system could change the sign. This topic was investigated by the group of Sadamichi Maekawa [104]. They reconsidered the skew-scattering contribution to the SHE in the framework of Fert and Levy's phase shift model and focused especially on the  $p$  phase shift  $\eta_1$  since it determines the sign of the SHA. After performing quantum Monte Carlo calculations which include local electron correlation effects for the  $5d$  states of the Ir impurity, they find that  $\eta_1$  actually changes sign. Accordingly, the remaining discrepancy could be solved. Under the assumption of well recorded experimental and theoretical data, this is the last resort to bring all considerations into accordance.

### 3.3. Potential Scattering versus Spin-Orbit Scattering

While the previous section focused on the phase-shift model in terms of  $j$ -dependent (relativistic) phase shifts, I will concentrate on the formulation based on  $l$ -dependent (non-relativistic) scattering phase shifts now. Although they are called non-relativistic phase shifts, which refers to the classification according to the angular momentum  $l$ , the scalar-relativistic effects are still taken into account.

The underlying idea is based on the resonant-scattering model proposed by Fert and Levy [38] who restrict their consideration to scattering events between the  $d$  and  $p$  channels only. The reason for this restriction is the knowledge that the residual resistivity of noble metals with transition-metal impurities is well described by Friedel's  $d$ -resonance model [55, 105, 106]. Accordingly, it was assumed that the spin-orbit driven transverse transport in Cu systems with  $5d$  impurities is also caused mainly by  $d$  states. The derivation outlined in section 2.4.2 extends this approach to all contributions between  $s$ ,  $p$ ,  $d$ , and  $f$  electrons. For  $5d$  impurities in a Cu host, the relativistic phase shifts based on equation (2.84) are given in table 3.3, whereas table 3.4 shows the corresponding phase shifts in absence of SOC utilizing equation (2.179).

Besides the restriction to  $d$ - $p$  scattering events, Fert and Levy obtained  $d$  phase shifts relying on Friedel's sum rule for isolated atoms

$$\sum_l Z_l = \frac{2}{\pi} \sum_l (2l + 1) \eta_l \quad (3.16)$$

which leads to

$$\eta_2 = \frac{\pi}{10} Z_d \quad (3.17)$$

for  $d$  electrons. In their approach, the  $p$  phase shift was treated as a free parameter which needed to be obtained by a fit to experimental data. As a reference

Table 3.3.: The relativistic phase shifts of  $5d$  impurities in a Cu host calculated by means of the KKR Green function method.

impurity	$\delta_s$	$\delta_{p_{1/2}}$	$\delta_{p_{3/2}}$	$\delta_{d_{3/2}}$	$\delta_{d_{5/2}}$	$\delta_{f_{5/2}}$	$\delta_{f_{7/2}}$
Lu	-0.73	-0.29	-0.44	0.60	0.53	0.002	-0.001
Hf	-0.56	-0.20	-0.36	1.10	0.90	0.007	0.006
Ta	-0.43	-0.13	-0.29	1.69	1.36	0.008	0.007
W	-0.35	-0.07	-0.24	2.09	1.74	0.008	0.008
Re	-0.28	-0.03	-0.20	2.33	2.02	0.007	0.007
Os	-0.22	0.01	-0.17	2.51	2.23	0.007	0.007
Ir	-0.16	0.04	-0.14	2.65	2.43	0.006	0.006
Pt	-0.07	0.09	-0.10	2.77	2.62	0.006	0.006
Au	0.08	0.18	-0.04	2.89	2.80	0.006	0.006

Table 3.4.: The non-relativistic phase shifts obtained from the relativistic ones by equation (2.179) and the partial  $s$ ,  $p$ , and  $d$  charges of  $5d$  impurity atoms in a Cu host. In addition, the number of  $d$  electrons ( $N_d$ ) for an isolated impurity atom as well as the corresponding  $d$  phase shifts based on Friedel's sum rule (FSR) in equation (3.17) are shown. The  $5d$  shell filling causes a monotonic enhancement of the  $s$  and  $p$  partial charges, while the partial  $f$  charges stay almost constant. Their values are less than 0.1 and not included here.

impurity	$\eta_0$	$\eta_1$	$\eta_2$	$s$	$p$	$d$	$N_d$	$\eta_2^{\text{FSR}}$
Lu	-0.73	-0.39	0.56	0.38	0.34	1.16	1	0.31
Hf	-0.56	-0.31	0.98	0.45	0.38	1.78	2	0.63
Ta	-0.43	-0.24	1.49	0.50	0.42	2.62	3	0.94
W	-0.35	-0.18	1.88	0.54	0.46	3.64	4	1.26
Re	-0.28	-0.14	2.14	0.58	0.48	4.73	5	1.57
Os	-0.22	-0.11	2.34	0.61	0.51	5.84	6	1.88
Ir	-0.16	-0.08	2.52	0.64	0.54	6.94	7	2.20
Pt	-0.07	-0.04	2.68	0.69	0.58	7.97	9	2.83
Au	0.08	0.03	2.84	0.78	0.67	8.81	10	3.14

point, they chose a Cu(Ir) alloy, assuming  $Z_d = 8$ . Then, using  $\alpha = 2.1\%$  from reference [98] they found  $\eta_1 = -4.3^\circ = -0.075^3$ , which is actually in very good agreement with the corresponding value  $\eta_1^{\text{Ir}} = -0.08$  in table 3.4. Furthermore, they used this  $\eta_1 = -0.075$  for *all* considered  $5d$  impurities in Cu, while the *ab initio*  $p$  phase shifts (table 3.4) vary quite strongly and even change sign for Au. According to the highlighted differences between the approach used by Fert and Levy and the one presented here, arising discrepancies in the respective results are not surprising. Actually, Fert and Levy already mentioned [38] that the disregarded influence of a crystal field in their isolated-atom approximation can change the resulting phase shifts and consequently the magnitude of the spin Hall effect. An exhaustive quantitative analysis performed on the basis of *ab initio* calculations for the scattering phase shifts will be presented in what follows.

In order to apply the phase shift model by means of equations (2.164), (2.172), and (2.177) - (2.179) for a Cu host with  $5d$  impurities,  $k_F = 1.346 \text{ \AA}^{-1}$  is used. This value was obtained via averaging the wave vector over the Fermi surface of a copper crystal with the unit cell volume  $V_0 = a^3/4$  and the lattice constant  $a = 3.6148 \text{ \AA}$ . Figure 3.13 shows results for the SHC obtained by the considered phase-shift model in comparison to direct first-principles calculations performed applying the Boltzmann equation and the Kubo-Středa formula<sup>4</sup>. Also included are the corresponding results of the relativistic phase shift model presented in the previous section. The results of the considered non-relativistic and the relativistic phase shift models al-

<sup>3</sup>Based on the sign issue presented in section 3.2 and the corresponding erratum published by Fert and Levy [100], the free (in their approach) parameter  $\eta_1$  has to change sign. This would contradict table 3.4 but could be understood by the work of Xu et al. [104], which was discussed at the end of section 3.2.

<sup>4</sup>As in section 3.2, the results of the Kubo-Středa approach were obtained in collaboration with the group of Hubert Ebert in Munich.



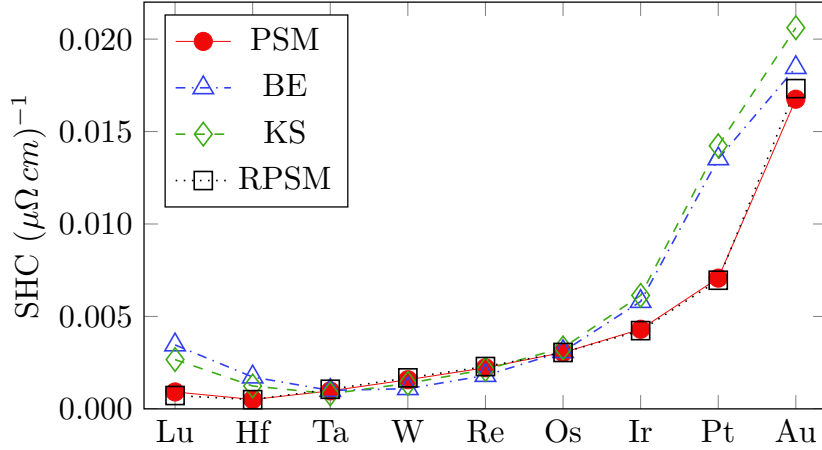


Figure 3.13.: The spin Hall conductivity for 5d impurities in a Cu host obtained by the considered phase shift model (PSM), the Boltzmann equation (BE), and the Kubo-Středa formula (KS). For comparison, the results obtained within the relativistic phase shift model (RPSM) introduced in section 3.2 are shown. The impurity concentration is fixed to 1 at.%.

most coincide, which points to an efficient treatment of the SOC within the used perturbative approach. In addition, the models are in good agreement with the results of the *ab initio* calculations. This is a consequence of two facts. Namely, copper possesses an almost spherical Fermi surface and exhibits a relatively weak SOC. As shown in reference [H4], which presents a detailed systematic comparison between results from the phase shift model and first-principles calculations for various host-impurity combinations, these are the requirements to the host material in order to provide good qualitative agreement with *ab initio* results.

In comparison to the first-principles calculations, the introduced models give easy access to a detailed analysis, which helps to identify the most important contributions. The model discussed in this section is particularly useful in that respect, since equation (2.172) makes it possible to separate different  $l$  channels for the spin-orbit scattering contributing to the SHC. They are shown in figure 3.14 and labeled with  $ll'$  according to the related terms

$$C_{ll'} = \frac{\lambda_l \sin^2 \eta_l}{\Delta_l} \sin(2\eta_l - \eta_{l'}) \sin \eta_{l'} \quad (3.18)$$

in the curly brackets of

$$\begin{aligned} \sigma_{yx}^+ \propto \tau_0^2 \left\{ \frac{1}{3} \frac{\lambda_1 \sin^2 \eta_1}{\Delta_1} [\sin(2\eta_1 - \eta_0) \sin \eta_0 - \sin(2\eta_1 - \eta_2) \sin \eta_2] \right. \\ \left. + \frac{\lambda_2 \sin^2 \eta_2}{\Delta_2} [\sin(2\eta_2 - \eta_1) \sin \eta_1 - \sin(2\eta_2 - \eta_3) \sin \eta_3] \right. \\ \left. + 2 \frac{\lambda_3 \sin^2 \eta_3}{\Delta_3} \sin(2\eta_3 - \eta_2) \sin \eta_2 \right\}. \quad (3.19) \end{aligned}$$

Obviously, all contributions involving  $s$  and  $f$  states are negligible and the total SHC is provided just by two terms labeled as  $p-d$  and  $d-p$ . Surprisingly, the  $p-d$

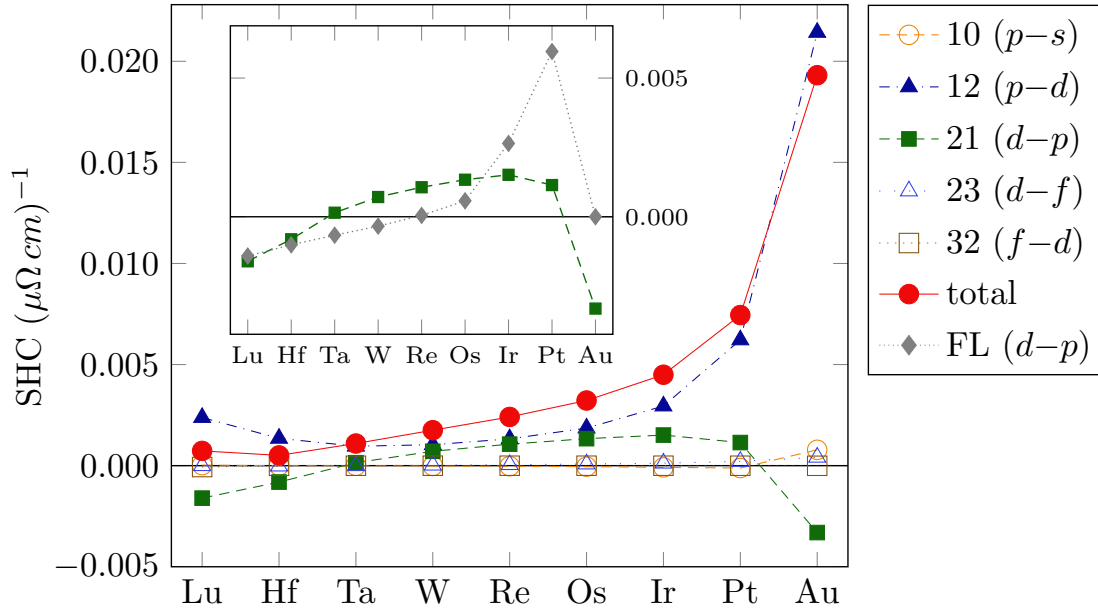


Figure 3.14.: The spin Hall conductivity for 5d impurities in a Cu host obtained by the considered phase shift model. The different contributions to  $\sigma_{yx}^s$  labeled as  $l'$  correspond to  $C_{l'}$  defined by equation (3.18). The inset shows a direct comparison between the SHC due to  $d-p$  scattering based on phase shifts from Friedel's sum rule, as used by Fert and Levy (FL), or *ab initio* calculations.

contribution, related to the spin-orbit scattering in the  $p$  channel, is of the same order as the  $d-p$  term. Moreover, for Pt and Au impurities the  $p-d$  contribution becomes even significantly larger than the  $d-p$  one. This result shows that the simplified models that are aimed at “a general rather than numerical description” [38] need to be examined intensively in order to predict reliable qualitative results.

The inset of figure 3.14 also helps to compare the results for the single  $d-p$  contribution from Fert and Levy [38] with those obtained here. Basically, the order of magnitude of the values is equal although several differences can be obtained. For instance, a drastic disagreement arises for the Au impurity for which the approach of reference [38] predicts a vanishing SHC due to Friedel's sum rule (since  $\eta_2 = \pi$ ), whereas the *ab initio* approach for the phase shifts forecasts a relatively large (negative) contribution. Furthermore, the sign change which appears around the Re impurity in reference [38] is shifted to a lower  $d$ -shell filling and emerges nearby Ta applying the *ab initio* input. This is a direct consequence of used phase shifts which are larger than the corresponding ones stemming from Friedel's sum rule, as can be seen in table 3.4. Equation (3.18) helps to understand that larger  $d$ -phase shifts lead to the aforesaid shift of the  $l$ -dependent sine contribution in the  $C_{21}$  term. The *ab initio* treatment with the consideration of the impurity within a host cluster suffices to deliver results which confirm the corresponding prediction from Fert and Levy forecasting the described left-shift of the sign change when using scattering phase shifts from *ab initio* calculations [38].

In order to get a deeper insight into the origin of the aforementioned unexpected results, which show that  $p-d$  and  $d-p$  contributions give comparable results, it is worth using another helpful property of equation (3.19). The specific structure of

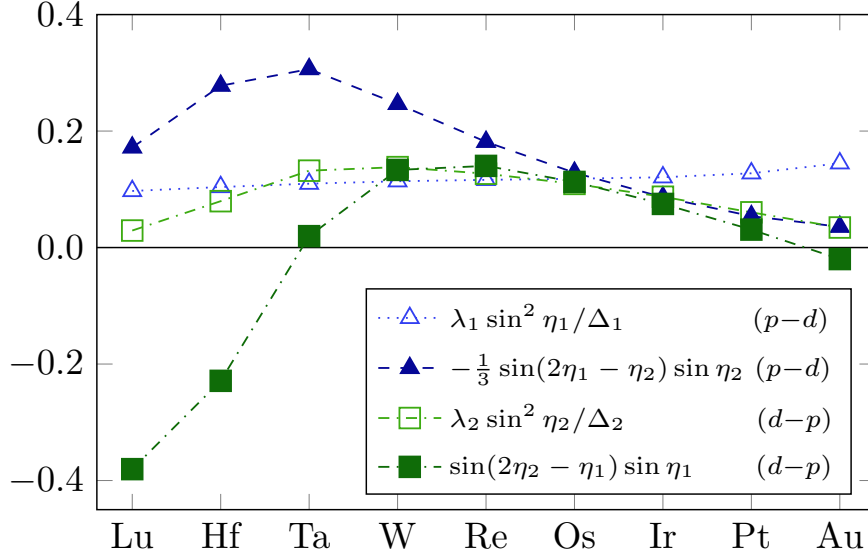


Figure 3.15.: Analysis of the spin-orbit and potential scattering contributions to the term  $C_{UW}$  for 5d impurities in Cu. The two parts of the contributions  $C_{p-d}$  and  $C_{d-p}$  are shown separately.

this equation for the spin Hall conductivity allows to analyze the interplay between the spin-orbit and the potential scattering as well as the respective contributions to the SHE. Precisely, it is possible to divide the terms  $C_{p-d} \equiv -\frac{1}{3}C_{12}$  and  $C_{d-p} \equiv C_{21}$  which give the dominant contributions to equation (3.19) into two factors. While the first one,  $(\lambda_l/\Delta_l)\sin^2\eta_l$ , can be attributed to the spin-orbit scattering strength for the corresponding  $l$  channel, the other one is described merely in terms of the non-relativistic phase shifts. Figure 3.15 shows the separate contributions for the investigated 5d impurities in Cu. The two terms related to SOC in the  $l = 1$  or  $l = 2$  channel behave differently. On the one hand, the part for  $l = 1$  has just a small enhancement going from Lu to Au. On the contrary, the corresponding part for  $l = 2$  shows resonance behavior around W with reduced values towards Lu and Au caused by the 5d shell filling, which can be followed in table 3.4. Hence, for Au impurities the spin-orbit scattering strength in the  $p$  channel is four times larger than for  $d$  states. However, both contributions are of comparable magnitude from Hf to Ir impurities. The question of how they contribute to the entire spin Hall conductivity is determined by the second part of the corresponding  $C_{UW}$  terms given by

$$\sin(2\eta_l - \eta_{l'}) \sin \eta_{l'} = 2 \sin \eta_l \sin \eta_{l'} \cos(\eta_l - \eta_{l'}) - \sin^2 \eta_{l'}. \quad (3.20)$$

Interestingly, the used identity reveals a symmetric term with respect to the exchange of  $l$  and  $l'$ . The remaining term, which depends on  $\eta_2$  and  $\eta_1$  for the  $p-d$  and  $d-p$  contributions, respectively, is responsible for emerging differences. In this way, the scattering-in term expressed in terms of  $C_{UW}$  highlights the coupling between, e.g. the spin-orbit scattering in the  $p$  channel and the potential scattering in the  $d$  channel. For the considered systems, the latter one is enhanced by the resonance properties of the 5d impurities in copper. The consideration of all necessary terms which combine the two scattering mechanisms leads to a positive SHC and consequently a positive SHA for all the considered systems. This is in contrast to

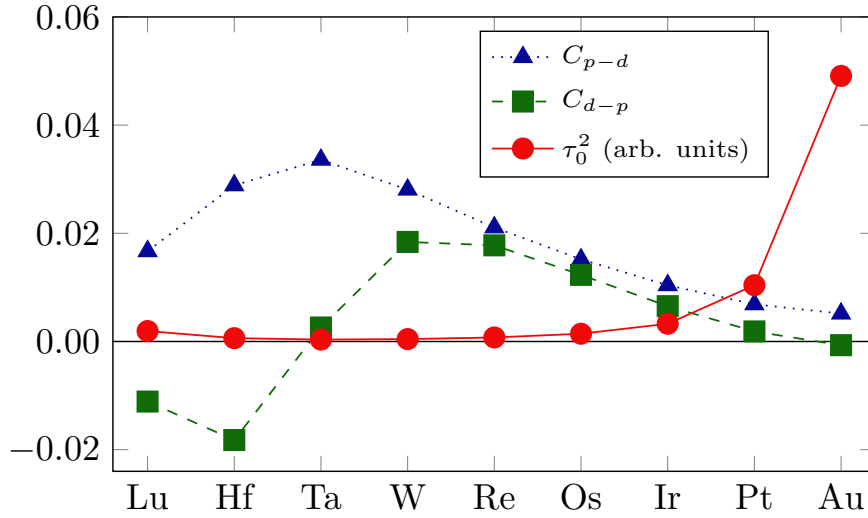


Figure 3.16.: Analysis of the two main contributions form  $C_U$  terms for  $5d$  impurities in Cu in comparison to the influence of the momentum relaxation time.

the results of reference [38] but in coherence with values obtained from *ab initio* methods visible in figure 3.13.

While the previous discussions can explain the positive sign for all the considered impurities in Cu, it cannot account for the significant enhancement for Pt and Au, as seen in figures 3.13 and 3.14. Figure 3.16, showing the momentum relaxation time in addition to the two dominant contributions in the braces of equation (3.19), helps to identify  $\tau_0$  to be responsible for the the main trend of the total SHC. In this way, the strong correlation between  $\tau_0^2$  and the total SHC of figures 3.13 and 3.14 together with equation (3.19) points to the crucial role of the potential scattering strength by itself for the magnitude of the SHC. Consequently, one cannot rely on the spin-orbit scattering strength only when considering the spin Hall effect.

### 3.4. Towards an *Ab Initio* Semiclassical Description of Side Jump

As exposed in the first section of the results, the first-principles semiclassical description of the skew-scattering mechanism was already successfully implemented and can be used to describe bulk as well as film systems appropriately. For the side-jump mechanism, the situation is different. Several approaches describe the SJ contribution to the anomalous Hall effect and present material-specific results for magnetic systems [107–109]. Nevertheless, the microscopic origins of AHE and SHE are the same. The cited publications present fully quantum-mechanical calculations of the transport properties on basis of Kubo approaches. A difference between those is the way, the side jump is considered. On the one hand, Kovalev et al. [107] and Weischenberg et al. [108] describe the SJ in terms of the host electronic structure. Accordingly, they investigate the *scattering-independent* side jump. On the other hand, Lowitzer et al. [109] use a coherent potential approximation to describe disorder and connect both extrinsic contributions with vertex corrections. In this way, it is quite easy to separate different contributions to the entire anomalous Hall conductivity obtained within the Kubo-Středa approach by

$$\sigma_{yx} = \sigma_{yx}^{\text{intr}} + \alpha^{\text{skew}} \sigma_{xx} + \sigma_{yx}^{\text{sj}}, \quad (3.21)$$

where  $\alpha^{\text{skew}}$  is the anomalous Hall angle due to skew scattering. By switching off the vertex corrections, they eliminate the intrinsic contribution. Afterwards, the limit  $\sigma_{xx} \rightarrow 0$  reveals the SJ conductivity.

Fert and Levy [38] went another path. They present material-specific results for the side-jump mechanism caused by *5d* impurities in a copper host, which were obtained based on a phase shift model similar to the one used for the description of skew scattering.

The aim of this chapter is to introduce an initial step into the direction of an *ab initio* semiclassical description of side jump considering two different simplified approaches. The first one follows a suggestion of Sinitsyn et al. [39, 78]. It focuses on the host properties expressed in terms of the Berry curvature, which is calculated from first principles according to reference [72] here. The corresponding side-jump conductivity contains the side-jump velocity (2.136) based on the microscopic displacement given by equation (2.139). The second approach places the emphasis on the properties of the impurities. Similar to the case of skew scattering, the resonant scattering model from Fert and Levy [38] is extended for this purpose. This approach is based on the side-jump velocity (2.156). The used scattering phase shifts are obtained by means of *ab initio* calculations.

In order to investigate the first approach, I will apply the corresponding expression (2.140) for  $\sigma_{yx}^{\text{sj}}$  to real materials. Namely, a Cu host with *5d* or Bi impurities is studied. Figure 3.17 shows the corresponding results. A first look at the spin Hall conductivity in figure 3.17(a) indicates that this quantity is more or less impurity independent as it was expected from the construction of the model. The slight variations arise solely from the scattering probability in equation (2.136) which depends on the impurity potential. Additionally, one can find that the influence of

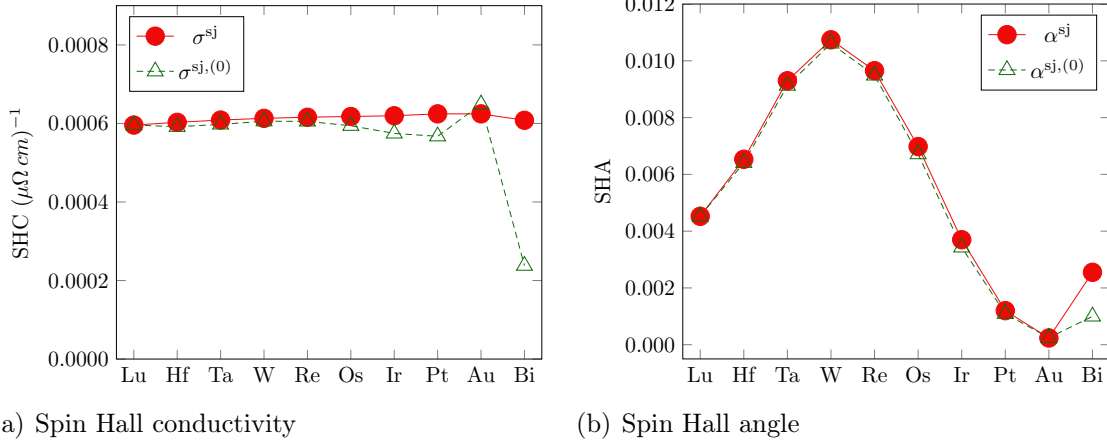


Figure 3.17.: The impurity-independent side-jump contribution to SHC and SHA for 5d and Bi impurities in Cu arising from the simplified model based on the Berry curvature. Besides the values related to the converged  $\Lambda_{\mathbf{k}}$  from equation (2.104) used for the SHC (2.140), the results for  $\sigma^{\text{sj},(0)}$  and  $\alpha^{\text{sj},(0)}$  employing the anisotropic RTA,  $\Lambda_{\mathbf{k}}^{(0)} = \tau_{\mathbf{k}} \mathbf{v}_{\mathbf{k}}$ , are shown to illustrate the influence of the scattering-in term on SJ in this model.

the scattering-in term of equation (2.104) is rather small. In particular, it hardly influences the results for the 5d impurities. The situation for Bi is quite different. As already stated for the skew-scattering mechanism, the scattering-in term has a strong impact especially for such  $p$  scatterers as Bi. In contrast to the SHC, the spin Hall angle has a strong dependence on the impurity atom, which originates from the impurity-dependent charge conductivity in the denominator of equation (1.9). Nevertheless, the influence of the scattering-in term on the SHA is a bit lowered in comparison to the SHC since it affects the charge conductivity as well, leading to a partial compensation.

These calculations can be considered as an estimation for the order of magnitude of the impurity-independent contribution to side jump. However, the restrictions to a  $\mathbf{k}$ -independent Berry curvature or small scattering angles are not fulfilled generally. Though, as can be seen in reference [72], the Berry curvature in Cu changes gently over the entire Fermi surface and its overall value is quite small. Hence, the order of magnitude should be reliable. For heavier systems like Au or spin hot spots forming materials like Al, the used approximation would be questionable since, for example, the corresponding maximum absolute values of the Berry curvature are increased by factors of 20 to 10000 [72].

As already mentioned, the Berry curvature-based model for the description of side jump is restricted to host-influence effects. As a counter-pole to this approach, the phase shift model, which only considers the influence of impurities, will be investigated in what follows. The corresponding formulas outlined in section 2.4.3 extend the consideration of Fert and Levy [38] to  $s$ ,  $p$ ,  $d$ , and  $f$  states, similar to the examined case of skew scattering. Additionally, the incorporation of the mean free path  $\Lambda_{\mathbf{k}}$  was extended beyond the relaxation time approximation leading to a separation between  $\sigma_{yx}^{\text{sj I}}$  and  $\sigma_{yx}^{\text{sj II}}$ . While  $\sigma_{yx}^{\text{sj I}}$  neglects the influence of the scattering-in term (see equation (2.191)), equation (2.192) for  $\sigma_{yx}^{\text{sj II}}$  includes the corresponding first contribution. In order to apply equations (2.196) and (2.197), the relativistic

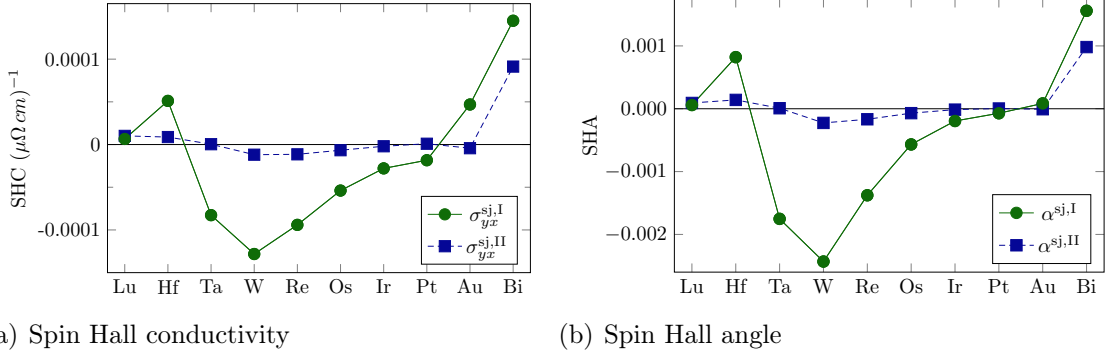


Figure 3.18.: The side-jump contribution to SHC and SHA for 5d and Bi impurities in Cu arising from the phase shift model. The graphs show the first and second contributions separately, which are related to neglecting the scattering-in term for the mean free path ( $\sigma_{yx}^{\text{sj,I}}$ , equations (2.191) and (2.196)) or considering its first iterative step ( $\sigma_{yx}^{\text{sj,II}}$ , equations (2.192) and (2.197)).

phase shifts from table 3.3 were used. The energy derivatives of the phase shifts were obtained numerically by a central difference quotient between phase shifts at energies  $10^{-6}$  Ry above and below the Fermi level. They are shown in table 3.5. The corresponding results for the spin Hall conductivity as well as for the related contribution to the spin Hall angle for 5d and Bi impurities in copper are shown in figure 3.18. As intended by the model, the results are strongly impurity dependent. Generally, the contribution stemming from the relaxation time approximation for the mean free path,  $\sigma_{yx}^{\text{sj,I}}$  and  $\alpha^{\text{sj,I}}$ , is larger than the part related to the scattering-in term,  $\sigma_{yx}^{\text{sj,II}}$  and  $\alpha^{\text{sj,II}}$ . Nevertheless, it does not seem reasonable to fully neglect the smaller contribution since for some impurities it is comparable to the first contribution. Especially for Bi, for which also the impurity-independent contribution to the side jump conductivity was strongly influenced by the scattering-in term (see

Table 3.5.: The energy derivatives of relativistic phase shifts of 5d or Bi impurities in a Cu host at the Fermi level given in  $(\text{Ry})^{-1}$ .

impurity	$\partial_{\mathcal{E}}\delta_s$	$\partial_{\mathcal{E}}\delta_{p_{1/2}}$	$\partial_{\mathcal{E}}\delta_{p_{3/2}}$	$\partial_{\mathcal{E}}\delta_{d_{3/2}}$	$\partial_{\mathcal{E}}\delta_{d_{5/2}}$	$\partial_{\mathcal{E}}\delta_{f_{5/2}}$	$\partial_{\mathcal{E}}\delta_{f_{7/2}}$
Lu	-0.66	-0.40	-0.57	3.07	2.56	0.027	0.029
Hf	-0.67	-0.30	-0.49	5.36	4.56	0.037	0.034
Ta	-0.67	-0.22	-0.40	4.94	5.60	0.041	0.038
W	-0.67	-0.15	-0.37	3.04	4.89	0.040	0.038
Re	-0.67	-0.11	-0.32	1.70	3.70	0.038	0.036
Os	-0.67	-0.06	-0.28	0.86	2.50	0.035	0.033
Ir	-0.67	-0.02	-0.25	0.31	1.40	0.032	0.031
Pt	-0.70	0.04	-0.21	-0.06	0.48	0.031	0.030
Au	-0.78	0.13	-0.13	-0.25	-0.13	0.033	0.031
Bi	-1.28	-0.42	0.09	0.03	-0.03	0.067	0.065

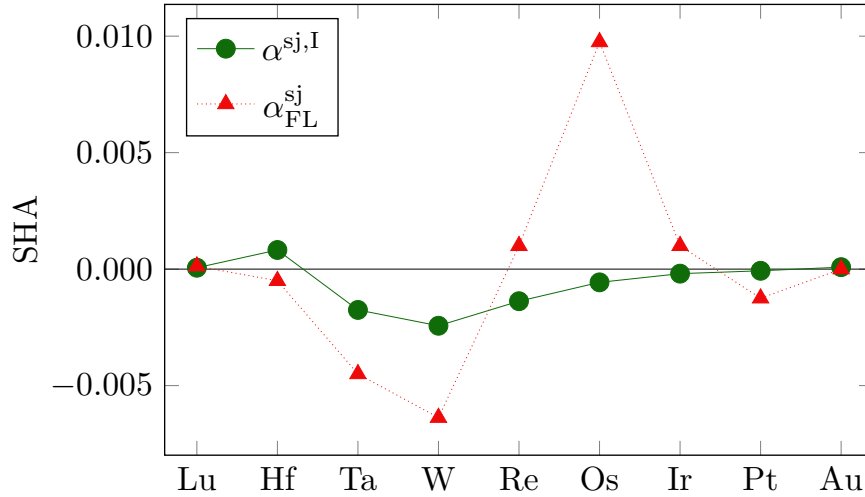


Figure 3.19.: The spin Hall angle  $\alpha_{FL}^{sj}$  from Fert and Levy [38] scaled to an impurity concentration of 1 at.% in comparison to the results  $\alpha^{sj,I}$  from the extended phase shift model.

figure 3.17), this contribution is of enormous importance. Additionally, one has to keep in mind that the iteration [65, H5] is not carried out beyond the first step in this analytical model. Therefore, further terms can also contribute when the entire scattering-in term is taken into account. However, the predicted values for the impurity-dependent side-jump contribution to the SHE are about an order of magnitude smaller than the impurity-independent part discussed above as well as the skew-scattering contribution (for an impurity concentration of 1 at.%) considered in section 3.3.

In the following part, I want to discuss the results from the extended phase shift model in comparison to those obtained by Fert and Levy [38]. As can be seen in figure 3.19, the two curves are quite different. In the case of Fert and Levy, the SHA changes sign nearby the Re impurity. This zero crossing occurs between Hf and Ta when the phase shifts from the *ab initio* calculations are used in the extended model. This shift to a lower *d*-shell filling has the same origin as pointed out in the discussion of skew scattering in section 3.3. To be exact, the used phase shifts are larger than those obtained from Friedel's sum rule (3.17) restricted to *d* electrons. Considering the trigonometric character of the leading term  $\cos(3\eta_2 - \eta_1) \sin \eta_2 \sin \eta_1$  for the SHC as used in reference [38], this behavior can be understood straightforwardly. Additionally, the absolute values of the spin Hall angles originating from the *ab initio* phase shifts are lowered in comparison to the other results. This characteristic is predominantly caused by the SOC constant, which is expressed by the scattering phase shifts from the impurity embedded in the host crystal (as discussed in section 2.4.2), whereas Fert and Levy approximate it by the corresponding atomic SOC constant from reference [110]. Both differences, the left-shift of the sign change as well as the reduced amplitudes, confirm a statement from the end of reference [38], where the authors predict such features for real scattering phase shifts.

Another important difference between the two curves is the impurity trend. The data published by Fert and Levy show a sign change from negative to positive near Re, whereas the results based on equation (2.196) switch sign from positive to nega-



tive near Hf when the atomic number is increased. In order to check the possibility of a sign issue in the used formula, appendix E shows the derivation of the side-jump conductivity in terms of non-relativistic phase shifts restricted to scattering between the resonant  $d$  and the  $p$  states, while the constriction to SOC-inducing  $d$  states is made. The comparison of equation (E.7) with the corresponding formula of reference [38] clearly indicates the aforementioned sign problem. In order to reassure in this regard, another formulation was derived in the appendix. Precisely, reference [94] from the same authors investigates skew-scattering and side-jump contributions to the spin Hall effect in bismuth-doped copper using the scattering phase shift model in terms of relativistic phase shifts. As shown by equation (E.15), the sign between their expression and ours coincides in this case.

As a last proof for the accordance of sign between the various equations for the side-jump conductivity derived within this thesis, a comparison of the results for bismuth impurities in copper is helpful, which can be found in table 3.6. If all  $s$ ,  $p$ ,  $d$ , and  $f$  channels are taken into account, the spin Hall conductivity is positive independent of the formulation in terms of either relativistic, using equation (2.196), or non-relativistic, employing equation (E.9), phase shifts. Hence, both models give equal results with respect to sign. Additionally, there is good agreement with respect to the magnitude of the SHC which points to an efficient treatment of SOC, as was already mentioned in section 3.3. This discussion manifests the existence of a sign problem for the side-jump contribution either in reference [38] or [94]. The remaining task is to clarify this point. Table 3.6 also shows the Cu(Bi) result for the SHC from side jump based on equation (E.15), which is entirely the same as in reference [94]. As the others, this conductivity has positive sign, which is in agreement with Levy et al. [94]. Hence, the assumption of an erroneous equation in reference [38] is confirmed. Nevertheless, the absolute value predicted by equation (E.15) is smaller by about a factor of three in comparison to the full equations. This discrepancy arises from neglecting terms including the energy derivative of the  $s$  phase shift. If these terms are incorporated, which can be done by inclusion of all  $s$ - $p$  transitions in equation (2.196), the remaining small difference can be ascribed to the higher  $l$  channel contributions. As already pointed out in section 3.3, this discussion shows that such models need to be treated with care within their limitations. The influence of neglected terms has to be checked carefully.

Table 3.6.: The side-jump contribution to the spin Hall conductivity for Cu(Bi) alloy from various approaches. The values are given in  $(\mu\Omega cm)^{-1}$ . Equations (2.196) and (E.9) include all transitions between  $s$ ,  $p$ ,  $d$ , and  $f$  states. However, equation (2.196) is formulated in terms of relativistic, whereas equation (E.9) is based on non-relativistic phase shifts. Equation (E.15) stems from reference [94], solely incorporating  $s$ - $p$  scatterings but neglecting terms with energy-derivatives of the  $s$  phase shifts. Those contributions are incorporated in the results called "eq. (2.196) only  $sp$  terms".

	eq. (2.196)	eq. (E.9)	eq. (E.15)	eq. (2.196) only $sp$ terms
$10^{-3}\sigma_{yx}^{+,sj,l}$	0.145	0.152	0.041	0.128

In the following, I want to comment on the factors influencing the sign of the side-jump contribution to SHC and SHA. The main outcome is that the sign of the side-jump conductivity is more sensitive to the definition of the transition matrix than the skew-scattering part. While in equation (2.165) for skew scattering the squared absolute value of the  $T$  matrix,  $|T_{\mathbf{k}'\mathbf{k}}|^2$ , appears, it is the term  $\text{Im}\{T_{\mathbf{k}\mathbf{k}'}^* \nabla_{\mathbf{k}'} T_{\mathbf{k}\mathbf{k}'}\}$  which is part of the expression (2.190) for side jump. The striking difference between both terms is that any phase information of the  $T$  matrix cancels for skew scattering due to the absolute square, whereas it has direct impact on side jump. This becomes obvious if the term is rewritten as

$$\text{Im}\{T_{\mathbf{k}\mathbf{k}'}^* \nabla_{\mathbf{k}'} T_{\mathbf{k}\mathbf{k}'}\} = \text{Im}\{|T_{\mathbf{k}\mathbf{k}'}| e^{-i \arg T_{\mathbf{k}\mathbf{k}'}} \nabla_{\mathbf{k}'} (|T_{\mathbf{k}\mathbf{k}'}| e^{i \arg T_{\mathbf{k}\mathbf{k}'}})\} = |T_{\mathbf{k}\mathbf{k}'}|^2 \nabla_{\mathbf{k}'} (\arg T_{\mathbf{k}\mathbf{k}'}), \quad (3.22)$$

where  $\arg T_{\mathbf{k}\mathbf{k}'}$  represents the argument of the complex quantity  $T_{\mathbf{k}\mathbf{k}'}$ . As can be seen in equation (3.22), an opposite definition of the  $T$  matrix phase directly changes sign of the entire expression while this is not the case for skew scattering. Hence, a proper theoretical description of the side-jump conductivity has to start with a proper gauge for the phases.

In the last part of this section, I want to come back to the separation between the two side-jump conductivities. While  $\sigma^{\text{sj,I}}$  excludes the scattering-in term (vertex corrections)  $\sigma^{\text{sj,II}}$  includes it. In this sense, one has to reconsider equation (3.21) from the approach of Lowitzer et al. [33, 109], where the side-jump contribution was solely connected to the vertex corrections. Hence, a more appropriate formulation should look like

$$\sigma_{yx} = \sigma_{yx}^{\text{intr}} + \alpha^{\text{skew}} \sigma_{xx} + \sigma_{yx}^{\text{sj, no vc}} + \sigma_{yx}^{\text{sj, vc}} \quad (3.23)$$

which distinguishes between SJ contributions in dependence or independence of vertex corrections (vc) explicitly. The emerging problem is that a separation of the four contributions to the total transversal conductivity stemming from the Kubo-Středa approach cannot be done equally to equation (3.21). Precisely, the terms  $\sigma_{yx}^{\text{intr}}$  and  $\sigma_{yx}^{\text{sj, no vc}}$  are both independent of the vertex corrections and behave similarly in the limit  $\sigma_{xx} \rightarrow 0$ . A possible approach could be to determine the intrinsic spin Hall conductivity explicitly based on the Berry curvature formalism described in section 2.3.1. This is subject of future investigations.

## Chapter 4

# Summary

---

*“Pass on what you have learned.”*

— Jedi Master Yoda

Within the present work, I investigated the extrinsic contributions to the spin Hall effect in two- and three-dimensional alloys based on noble metals.

Firstly, ultrathin films were studied using density functional theory within the local density approximation by means of the relativistic Korringa-Kohn-Rostoker Green function method. The skew-scattering results stem from a semiclassical Boltzmann approach. They vary to some extent for Bi-doped one-monolayer noble metal films depending on host material and surface orientation. The largest spin Hall angle is about 80% found for the Au(111) film. The origin of this *colossal* spin Hall effect was analyzed by energy-dependent transport calculations. The consideration of the Bi impurity density of states identified a connection between the  $p_{1/2}$  states and the longitudinal conductivity. Accordingly, it is helpful to push the impurity  $p_{1/2}$  resonance states towards the Fermi level. The accompanied reduced charge conductivity leads to a further enhancement of the giant spin Hall effect caused by the reduced sample dimension. In this context, strain engineering was examined to tune the resonant scattering. The example of Bi-doped Cu(111) films indicates the feasibility to create a colossal spin Hall effect in this way. These results point to a new route to design materials with an optimized conversion of charge current into spin current.

In the second approach, the resonant scattering model for skew scattering proposed by Fert and Levy was generalized to  $s$ ,  $p$ ,  $d$ , and  $f$  channels. An extensive analysis of this model for copper bulk systems with Bi impurities, which also includes structural relaxation, paved the way for the solution of an emerged sign issue between theory and experiment in the different definition of the spin Hall angle. In addition to this analysis,  $5d$  impurities in copper were restudied. While the restriction to resonant  $d$  scattering does not lead to agreement with *ab initio* results from the Boltzmann or Kubo-Středa formula, the generalized model using phase shifts from *ab initio* calculations delivers consistent results. The interplay between spin-orbit scattering and impurity scattering was investigated in detail. Hence, terms related to spin-orbit scattering in the  $p$  channel can have tremendous influence for the investigated systems. Accordingly, the application of such models needs to be handled with care.

The work is concluded by first steps in the direction of an *ab initio* semiclassical description of side jump. A simplified approach using the host Berry curvature leads to impurity-independent spin Hall conductivities. Due to severe restrictions, this model can help to estimate the corresponding contribution rather than being predictive. Similar to skew scattering, the impurity-dependent resonant scattering model was generalized by considering all important  $l$  channels. An additional

separation to contributions including and neglecting the scattering-in term of the Boltzmann equation (vertex corrections) was executed.

In conclusion, I would like to provide a short overview of the discussed mechanisms contributing to the spin Hall effect. Each of them has a particular impact depending on the electronic structure of the system under consideration. The intrinsic mechanism is particularly important for transition metals exhibiting many bands at the Fermi level. In the regime of low impurity concentration, skew scattering is of considerable significance. For finite systems, the effect is very sensitive to the impurity position with respect to the surface. In bulk systems, a large difference of the atomic number between impurity and host, for example Bi in Cu or C in Au, is required for large skew-scattering contributions to the spin Hall effect. This picture is modified for ultrathin films where Bi impurities in one-monolayer Au films give rise to the colossal spin Hall effect due to resonant scattering. The side-jump mechanism is more complex. Although being an extrinsic effect for which scattering centers are mandatory, a simple approximation can describe it on the basis of the electronic structure of the ideal host. Another approach focuses on the changed electronic structure around the defect and provides a spin Hall conductivity strongly dependent on the type of impurity. This contribution can be divided further from a theoretical point of view. Namely, in contrast to skew scattering, it has terms independent of the vertex corrections in addition to those solely caused by them.

---

# Gauge Dependence of Transport Properties

As described during the discussion of the spin polarization in section 2.1.3, for systems with both time and space inversion symmetry, the spin quantization axis can point in an arbitrary direction. For practical calculations, an appropriate gauge must be chosen, especially when spin-flip events are included and have to be described adequately, as done in this thesis. The two presented gauges giving either the spin polarization parallel to the global quantization axis chosen along the  $z$  direction (gauge I) or maximizing the value  $\langle \psi_{\mathbf{k}}^+ | \underline{\beta} \sigma_z | \psi_{\mathbf{k}}^+ \rangle$  (gauge II) are identical in the non-relativistic limit [63]. Hence, the relative influence on the SHA should be smaller for a light host as Cu in comparison to much heavier hosts like Au. The corresponding investigation compares the quantity

$$\Delta_{\alpha}^{\text{II,I}} = \frac{\alpha^{\text{II}} - \alpha^{\text{I}}}{\alpha^{\text{II}}} \quad (\text{A.1})$$

based on the results for the spin Hall angles obtained for different systems from the two gauges.

As can be seen in figure A.1, the chosen gauge generally has more impact on the results for thicker films, whereas the influence on the 1 ML systems is rather small. Additionally, the above stated prediction of less influenced results for Cu than for Au is confirmed. While the relative change for the 11 ML Cu film stays below  $1.5 \cdot 10^{-4}$  it is more than one order of magnitude larger for the 11 ML Au system and exceeds the value of  $6 \cdot 10^{-3}$ .

Nevertheless, the presented influence for the film systems is smaller than for the corresponding bulk systems for which the maximal deviations are  $\Delta_{\alpha, \text{Cu}}^{\text{II,I}} = 1 \cdot 10^{-3}$  and  $\Delta_{\alpha, \text{Au}}^{\text{II,I}} = 4 \cdot 10^{-2}$ .

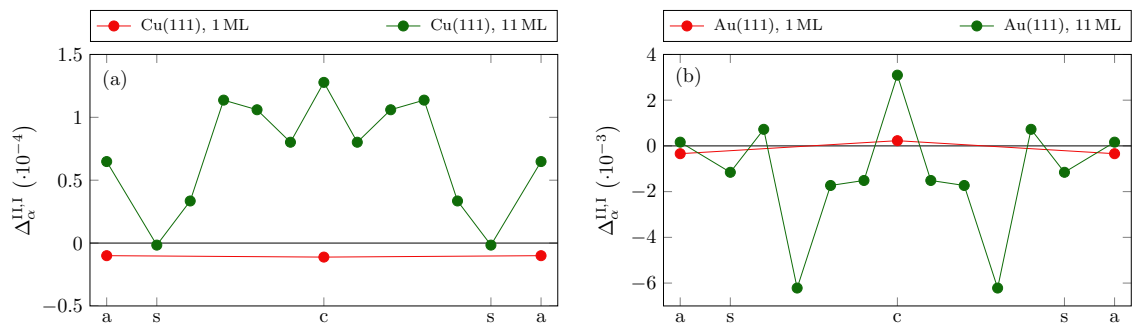


Figure A.1.: Comparison of the relative influence of the two discussed gauges on the SHA ( $\Delta_{\alpha}^{\text{II,I}}$ ) for Bi-doped (a) Cu and (b) Au film systems consisting of 1 or 11 ML.



# Longitudinal Conductivity in the Phase Shift Model

For a deeper investigation of the charge conductivity in the framework of the considered phase shift model, a suitable starting point is given by the corresponding expression

$$\sigma = \left( \frac{e^2}{\hbar} \right) \frac{m_e k_F}{\hbar (2\pi)^3} \int d\Omega_{\mathbf{k}} v_{\mathbf{k}}^x \Lambda_{\mathbf{k}}^x \quad (\text{B.1})$$

derived from equation (2.161). According to the separation of the mean free path

$$\Lambda_{\mathbf{k}}^x = \tau_{\mathbf{k}} v_{\mathbf{k}}^x + \tau_{\mathbf{k}} \sum_{\mathbf{k}'} P_{\mathbf{k}'\mathbf{k}} \tau_{\mathbf{k}'} v_{\mathbf{k}'}^x = \Lambda_{\mathbf{k}}^{\text{I},x} + \Lambda_{\mathbf{k}}^{\text{II},x} \quad (\text{B.2})$$

it is possible to make the separation  $\sigma_{xx} = \sigma_{xx}^{\text{I}} + \sigma_{xx}^{\text{II}}$ . Taking into account the spherical band approximation with  $\mathbf{v} = \hbar\mathbf{k}/m_e$ , it is possible to obtain

$$\sigma_{xx}^{\text{I}} = \left( \frac{e^2}{\hbar} \right) \frac{\hbar k_F}{m_e (2\pi)^3} \tau_0 \int d\Omega_{\mathbf{k}} k_x^2 = \left( \frac{e^2}{\hbar} \right) \frac{\hbar k_F^3}{6\pi^2 m_e} \tau_0 \quad (\text{B.3})$$

and

$$\begin{aligned} \sigma_{xx}^{\text{II}} &= \left( \frac{e^2}{\hbar} \right) \frac{\hbar k_F}{m_e (2\pi)^3} \tau_0^2 \int d\Omega_{\mathbf{k}} k_x \sum_{\mathbf{k}'} P_{\mathbf{k}'\mathbf{k}} k'_x \\ &= \left( \frac{e^2}{\hbar} \right) \frac{c_0 N V k_F^2}{\hbar^2 (2\pi)^5} \tau_0^2 \int d\Omega_{\mathbf{k}} \int d\Omega_{\mathbf{k}'} k_x k'_x |T_{\mathbf{k}'\mathbf{k}}|^2. \end{aligned} \quad (\text{B.4})$$

Using the transition matrix from equation (2.116) leads to

$$\begin{aligned} \sigma_{xx}^{\text{II}} &= \left( \frac{e^2}{\hbar} \right) \frac{c_0}{V_0} \frac{\hbar^2 k_F^2}{2\pi m_e^2} \tau_0^2 \sum_{lm} \left[ (l+m+1) e^{-i\delta_{l+\frac{1}{2}}} \sin \delta_{l+\frac{1}{2}} + (l-m) e^{-i\delta_{l-\frac{1}{2}}} \sin \delta_{l-\frac{1}{2}} \right] \times \\ &\left\{ \frac{(l+m+1)(l+m+2)(l+m+3) - (l-m+1)(l-m+2)(l-m+1)}{(2l+1)^2(2l+3)^2} e^{i\delta_{(l+1)+\frac{1}{2}}} \sin \delta_{(l+1)+\frac{1}{2}} \right. \\ &+ \frac{(l+m+1)(l+m+2)(l-m) - (l-m+1)(l-m+2)(l-m+2)}{(2l+1)^2(2l+3)^2} e^{i\delta_{(l+1)-\frac{1}{2}}} \sin \delta_{(l+1)-\frac{1}{2}} \\ &+ \frac{(l+m)(l+m-1)(l+m-1) - (l-m)(l-m-1)(l+m+1)}{(2l+1)^2(2l-1)^2} e^{i\delta_{(l-1)+\frac{1}{2}}} \sin \delta_{(l-1)+\frac{1}{2}} \\ &\left. + \frac{(l+m)(l+m-1)(l-m) - (l-m)(l-m-1)(l-m-2)}{(2l+1)^2(2l-1)^2} e^{i\delta_{(l-1)-\frac{1}{2}}} \sin \delta_{(l-1)-\frac{1}{2}} \right\}. \end{aligned} \quad (\text{B.5})$$

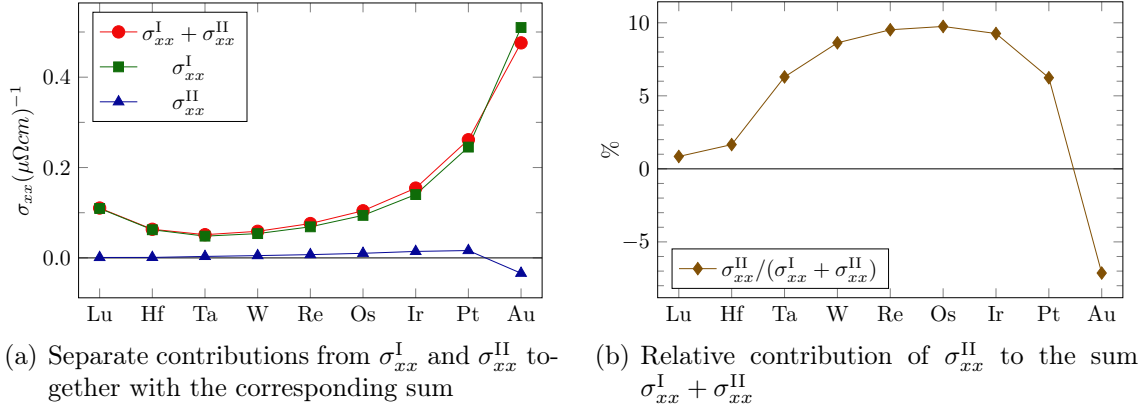


Figure B.1.: Comparison of  $\sigma_{xx}^I$  (neglecting the scattering-in term in the mean free path  $\Lambda_{\mathbf{k}}$ ) and  $\sigma_{xx}^{II}$  (taking into account the first iteration for the scattering-in term).

In order to compare the results for equation (B.3) and (B.5), the relaxation time from equation (2.187) was used. The corresponding data for 5d impurities in Cu is shown in figure B.1. It is visible that the second term gives positive contribution for impurities from Lu to Pt and is negative for Au only. The relative contribution of  $\sigma_{xx}^{II}$  to the sum of both terms lies between 1% for Lu and about 10% for Os. Hence, the restriction to the scattering-out term in  $\Lambda_{\mathbf{k}}$  for the estimation of the charge conductivity in the phase shift model seems to be a reasonable assumption.



## Integrals Over Spherical Harmonics

Reference [87] provides helpful expressions for integrals over three spherical harmonics. In order to derive the Hall component of the conductivity tensor in the framework of the phase shift models considered in section 2.4, the identities

$$\int d\Omega Y_l^m [Y_1^{-1} - Y_1^1] (Y_{l'}^{m'})^* = -\sqrt{\frac{3}{8\pi}} \times \left\{ \delta_{l',l+1} \left[ \delta_{m',m+1} \sqrt{\frac{(l+m+1)(l+m+2)}{(2l+1)(2l+3)}} - \delta_{m',m-1} \sqrt{\frac{(l-m+1)(l-m+2)}{(2l+1)(2l+3)}} \right] - \delta_{l',l-1} \left[ \delta_{m',m+1} \sqrt{\frac{(l-m)(l-m-1)}{(2l-1)(2l+1)}} - \delta_{m',m-1} \sqrt{\frac{(l+m)(l+m-1)}{(2l-1)(2l+1)}} \right] \right\} \quad (\text{C.1})$$

and

$$\int d\Omega Y_{l'}^{m'} [Y_1^1 + Y_1^{-1}] (Y_l^m)^* = -\sqrt{\frac{3}{8\pi}} \times \left\{ \delta_{l',l+1} \left[ \delta_{m',m+1} \sqrt{\frac{(l+m+1)(l+m+2)}{(2l+1)(2l+3)}} + \delta_{m',m-1} \sqrt{\frac{(l-m+1)(l-m+2)}{(2l+1)(2l+3)}} \right] - \delta_{l',l-1} \left[ \delta_{m',m+1} \sqrt{\frac{(l-m)(l-m-1)}{(2l-1)(2l+1)}} + \delta_{m',m-1} \sqrt{\frac{(l+m)(l+m-1)}{(2l-1)(2l+1)}} \right] \right\} \quad (\text{C.2})$$

are used. The combination of those together with

$$k_x = \sqrt{\frac{2\pi}{3}} k_F [Y_1^{-1}(\hat{\mathbf{k}}) - Y_1^1(\hat{\mathbf{k}})] \quad , \quad k_y = i\sqrt{\frac{2\pi}{3}} k_F [Y_1^{-1}(\hat{\mathbf{k}}) + Y_1^1(\hat{\mathbf{k}})] \quad (\text{C.3})$$

allows to represent the angular integrals required for the evaluation of

$$\sigma_{yx}^+ \propto \int d\Omega_{\mathbf{k}} \int d\Omega_{\mathbf{k}'} k_y k'_x |T_{\mathbf{k}'\mathbf{k}}^{+++}|_{\text{antisym}}^2 \quad (\text{C.4})$$

as

$$\int d\Omega_{\mathbf{k}} Y_l^m(\hat{\mathbf{k}}) [Y_1^{-1}(\hat{\mathbf{k}}) - Y_1^1(\hat{\mathbf{k}})] (Y_{l'}^{m'})^*(\hat{\mathbf{k}}) \int d\Omega_{\mathbf{k}'} Y_{l'}^{m'}(\hat{\mathbf{k}}') [Y_1^1(\hat{\mathbf{k}}') + Y_1^{-1}(\hat{\mathbf{k}}')] (Y_l^m)^*(\hat{\mathbf{k}}') = \left( \frac{3}{8\pi} \right) \left\{ \delta_{l',l+1} \left[ \delta_{m',m+1} \frac{(l+m+1)(l+m+2)}{(2l+1)(2l+3)} - \delta_{m',m-1} \frac{(l-m+1)(l-m+2)}{(2l+1)(2l+3)} \right] + \delta_{l',l-1} \left[ \delta_{m',m+1} \frac{(l-m)(l-m-1)}{(2l-1)(2l+1)} - \delta_{m',m-1} \frac{(l+m)(l+m-1)}{(2l-1)(2l+1)} \right] \right\}. \quad (\text{C.5})$$



## Side-Jump Conductivity within the Phase Shift Model

According to reference [87], the gradient emerging in the estimation of the side-jump conductivity (2.190) can be written as

$$\nabla_{\mathbf{k}} = \mathbf{e}_x \frac{\partial}{\partial k_x} + \mathbf{e}_y \frac{\partial}{\partial k_y} + \mathbf{e}_z \frac{\partial}{\partial k_z} = -\mathbf{e}_{+1} \nabla_{-1} + \mathbf{e}_0 \nabla_0 - \mathbf{e}_{-1} \nabla_{+1} \quad (\text{D.1})$$

with

$$\begin{aligned} \mathbf{e}_{+1} &= -\frac{1}{\sqrt{2}}(\mathbf{e}_x + i\mathbf{e}_y), & \mathbf{e}_0 &= \mathbf{e}_z, & \mathbf{e}_{-1} &= \frac{1}{\sqrt{2}}(\mathbf{e}_x - i\mathbf{e}_y), \\ \nabla_{-1} &= \frac{1}{\sqrt{2}} \left( \frac{\partial}{\partial k_x} - i \frac{\partial}{\partial k_y} \right), & \nabla_0 &= \frac{\partial}{\partial k_z}, & \nabla_{+1} &= -\frac{1}{\sqrt{2}} \left( \frac{\partial}{\partial k_x} + i \frac{\partial}{\partial k_y} \right), \\ \frac{\partial}{\partial k_x} &= \frac{1}{\sqrt{2}} (\nabla_{-1} - \nabla_{+1}), & \frac{\partial}{\partial k_z} &= \nabla_0, & \frac{\partial}{\partial k_y} &= \frac{i}{\sqrt{2}} (\nabla_{-1} + \nabla_{+1}). \end{aligned} \quad (\text{D.2})$$

In addition, the following helpful equations

$$\begin{aligned} \nabla_0 \left[ f(k) Y_l^m(\hat{\mathbf{k}}) \right] &= \sqrt{\frac{(l+1)^2 - m^2}{(2l+1)(2l+3)}} \left( \frac{\partial f}{\partial k} - \frac{l}{k} f \right) Y_{l+1}^m(\hat{\mathbf{k}}) \\ &\quad + \sqrt{\frac{l^2 - m^2}{(2l-1)(2l+1)}} \left( \frac{\partial f}{\partial k} + \frac{l+1}{k} f \right) Y_{l-1}^m(\hat{\mathbf{k}}) \end{aligned} \quad (\text{D.3})$$

and

$$\begin{aligned} \nabla_{\pm 1} \left[ f(k) Y_l^m(\hat{\mathbf{k}}) \right] &= \sqrt{\frac{(l \pm m + 1)(l \pm m + 2)}{2(2l+1)(2l+3)}} \left( \frac{\partial f}{\partial k} - \frac{l}{k} f \right) Y_{l+1}^{m \pm 1}(\hat{\mathbf{k}}) \\ &\quad - \sqrt{\frac{(l \mp m - 1)(l \mp m)}{2(2l-1)(2l+1)}} \left( \frac{\partial f}{\partial k} + \frac{l+1}{k} f \right) Y_{l-1}^{m \pm 1}(\hat{\mathbf{k}}) \end{aligned} \quad (\text{D.4})$$

can be found. For the  $y$ - $x$  component of the side-jump conductivities in equations (2.191) and (2.192), the  $k_y$  derivative of the  $T$  matrix needs to be inserted. Taking

into account equations (D.2) and (D.4), the corresponding expression

$$\begin{aligned}
\frac{\partial}{\partial k_y} \left[ f(k) Y_l^m(\hat{\mathbf{k}}) \right] &= \frac{i}{\sqrt{2}} (\nabla_{-1} + \nabla_{+1}) \left[ f(k) Y_l^m(\hat{\mathbf{k}}) \right] \\
&= \frac{i}{\sqrt{2}} \left\{ \left( \frac{\partial f}{\partial k} - \frac{l}{k} f \right) \left[ \sqrt{\frac{(l-m+1)(l-m+2)}{2(2l+1)(2l+3)}} Y_{l+1}^{m-1}(\hat{\mathbf{k}}) \right. \right. \\
&\quad \left. \left. + \sqrt{\frac{(l+m+1)(l+m+2)}{2(2l+1)(2l+3)}} Y_{l+1}^{m+1}(\hat{\mathbf{k}}) \right] \right. \\
&\quad \left. - \left( \frac{\partial f}{\partial k} + \frac{l+1}{k} f \right) \left[ \sqrt{\frac{(l+m-1)(l+m)}{2(2l-1)(2l+1)}} Y_{l-1}^{m-1}(\hat{\mathbf{k}}) \right. \right. \\
&\quad \left. \left. + \sqrt{\frac{(l-m-1)(l-m)}{2(2l-1)(2l+1)}} Y_{l-1}^{m+1}(\hat{\mathbf{k}}) \right] \right\} \quad (D.5)
\end{aligned}$$

can be obtained. Now, the function  $f$  required for the representation of the  $T$  matrix (2.193) needs to be specified. It reads

$$f(E) = \frac{1}{\sqrt{E}} \left[ \left( \frac{l+m+1}{2l+1} \right) e^{i\delta_{l+\frac{1}{2}}(E)} \sin \delta_{l+\frac{1}{2}}(E) + \left( \frac{l-m}{2l+1} \right) e^{i\delta_{l-\frac{1}{2}}(E)} \sin \delta_{l-\frac{1}{2}}(E) \right], \quad (D.6)$$

where the implicit energy dependence via  $k$  was written explicitly for all scattering phase shifts. Incorporating  $\frac{\partial f}{\partial k} = \frac{\partial f}{\partial E} \frac{\partial E}{\partial k}$  with  $\frac{\partial E}{\partial k} = \frac{\hbar^2 k}{m_e} = \hbar \sqrt{\frac{2E}{m_e}}$  leads to

$$\begin{aligned}
\frac{\partial f}{\partial k} &= \hbar \sqrt{\frac{2E}{m_e}} \frac{\partial f(E)}{\partial E} \\
&= \hbar \sqrt{\frac{2}{m_e}} \left[ \left( \frac{l+m+1}{2l+1} \right) e^{2i\delta_{l+\frac{1}{2}}} \frac{\partial \delta_{l+\frac{1}{2}}}{\partial E} + \left( \frac{l-m}{2l+1} \right) e^{2i\delta_{l-\frac{1}{2}}} \frac{\partial \delta_{l-\frac{1}{2}}}{\partial E} \right] \\
&\quad - \frac{\hbar}{E \sqrt{2m_e}} \left[ \left( \frac{l+m+1}{2l+1} \right) e^{i\delta_{l+\frac{1}{2}}} \sin \delta_{l+\frac{1}{2}} + \left( \frac{l-m}{2l+1} \right) e^{i\delta_{l-\frac{1}{2}}} \sin \delta_{l-\frac{1}{2}} \right]. \quad (D.7)
\end{aligned}$$

In order to determine the first side-jump contribution from equation (2.191), the abbreviation  $\tilde{T}_{\mathbf{k}\mathbf{k}'} = VT_{\mathbf{k}\mathbf{k}'}$  as well as the orthogonality of the spherical harmonics

$\int Y_{l'm'}^* Y_{lm} d\Omega = \delta_{ll'} \delta_{mm'}$  are used to rewrite

$$\begin{aligned}
& \int d\Omega_{\mathbf{k}'} \tilde{T}_{\mathbf{k}\mathbf{k}'}^* \frac{\partial \tilde{T}_{\mathbf{k}\mathbf{k}'}}{\partial k'_y} = \frac{32\pi^4 \hbar^6}{m_e^3 \sqrt{E_F}} \int d\Omega_{\mathbf{k}'} \sum_{l'm'} Y_{l'm'}^{m'}(\hat{\mathbf{k}}) \left( Y_{l'm'}^{m'}(\hat{\mathbf{k}}') \right)^* \times \\
& \quad \left[ \left( \frac{l' + m' + 1}{2l' + 1} \right) e^{-i\delta_{l'+\frac{1}{2}}} \sin \delta_{l'+\frac{1}{2}} + \left( \frac{l' - m'}{2l' + 1} \right) e^{-i\delta_{l'-\frac{1}{2}}} \sin \delta_{l'-\frac{1}{2}} \right] \frac{i}{\sqrt{2}} \sum_{lm} \left( Y_l^m(\hat{\mathbf{k}}) \right)^* \times \\
& \quad \left\{ \left( \frac{\partial f}{\partial k'} - \frac{l}{k'} f \right) \left[ \sqrt{\frac{(l-m+1)(l-m+2)}{2(2l+1)(2l+3)}} Y_{l+1}^{m-1}(\hat{\mathbf{k}}') + \sqrt{\frac{(l+m+1)(l+m+2)}{2(2l+1)(2l+3)}} Y_{l+1}^{m+1}(\hat{\mathbf{k}}') \right] \right. \\
& \quad \left. - \left( \frac{\partial f}{\partial k'} + \frac{l+1}{k'} f \right) \left[ \sqrt{\frac{(l+m-1)(l+m)}{2(2l-1)(2l+1)}} Y_{l-1}^{m-1}(\hat{\mathbf{k}}') + \sqrt{\frac{(l-m-1)(l-m)}{2(2l-1)(2l+1)}} Y_{l-1}^{m+1}(\hat{\mathbf{k}}') \right] \right\} \\
& = \frac{i}{\sqrt{2}} \frac{32\pi^4 \hbar^6}{m_e^3 \sqrt{E_F}} \sum_{l'm'} \left[ \left( \frac{l' + m' + 1}{2l' + 1} \right) e^{-i\delta_{l'+\frac{1}{2}}} \sin \delta_{l'+\frac{1}{2}} + \left( \frac{l' - m'}{2l' + 1} \right) e^{-i\delta_{l'-\frac{1}{2}}} \sin \delta_{l'-\frac{1}{2}} \right] \sum_{lm} \left( Y_l^m(\hat{\mathbf{k}}) \right)^* Y_{l'm'}^{m'}(\hat{\mathbf{k}}) \times \\
& \quad \left\{ \left( \frac{\partial f}{\partial k'} - \frac{l}{k'} f \right) \left[ \sqrt{\frac{(l-m+1)(l-m+2)}{2(2l+1)(2l+3)}} \delta_{l',l+1} \delta_{m',m-1} + \sqrt{\frac{(l+m+1)(l+m+2)}{2(2l+1)(2l+3)}} \delta_{l',l+1} \delta_{m',m+1} \right] \right. \\
& \quad \left. - \left( \frac{\partial f}{\partial k'} + \frac{l+1}{k'} f \right) \left[ \sqrt{\frac{(l+m-1)(l+m)}{2(2l-1)(2l+1)}} \delta_{l',l-1} \delta_{m',m-1} + \sqrt{\frac{(l-m-1)(l-m)}{2(2l-1)(2l+1)}} \delta_{l',l-1} \delta_{m',m+1} \right] \right\} \\
& = \frac{i}{\sqrt{2}} \frac{32\pi^4 \hbar^6}{m_e^3 \sqrt{E_F}} \sum_{lm} \left( Y_l^m(\hat{\mathbf{k}}) \right)^* \times \\
& \quad \left\{ Y_{l+1}^{m-1}(\hat{\mathbf{k}}) \left( \frac{\partial f}{\partial k'} - \frac{l}{k'} f \right) \sqrt{\frac{(l-m+1)(l-m+2)}{2(2l+1)(2l+3)}} \times \right. \\
& \quad \quad \left[ \left( \frac{l+m+1}{2l+3} \right) e^{-i\delta_{(l+1)+\frac{1}{2}}} \sin \delta_{(l+1)+\frac{1}{2}} + \left( \frac{l-m+2}{2l+3} \right) e^{-i\delta_{(l+1)-\frac{1}{2}}} \sin \delta_{(l+1)-\frac{1}{2}} \right] \\
& \quad + Y_{l+1}^{m+1}(\hat{\mathbf{k}}) \left( \frac{\partial f}{\partial k'} - \frac{l}{k'} f \right) \sqrt{\frac{(l+m+1)(l+m+2)}{2(2l+1)(2l+3)}} \times \\
& \quad \quad \left[ \left( \frac{l+m+3}{2l+3} \right) e^{-i\delta_{(l+1)+\frac{1}{2}}} \sin \delta_{(l+1)+\frac{1}{2}} + \left( \frac{l-m}{2l+3} \right) e^{-i\delta_{(l+1)-\frac{1}{2}}} \sin \delta_{(l+1)-\frac{1}{2}} \right] \\
& \quad - Y_{l-1}^{m-1}(\hat{\mathbf{k}}) \left( \frac{\partial f}{\partial k'} + \frac{l+1}{k'} f \right) \sqrt{\frac{(l+m-1)(l+m)}{2(2l-1)(2l+1)}} \times \\
& \quad \quad \left[ \left( \frac{l+m-1}{2l-1} \right) e^{-i\delta_{(l-1)+\frac{1}{2}}} \sin \delta_{(l-1)+\frac{1}{2}} + \left( \frac{l-m}{2l-1} \right) e^{-i\delta_{(l-1)-\frac{1}{2}}} \sin \delta_{(l-1)-\frac{1}{2}} \right] \\
& \quad - Y_{l-1}^{m+1}(\hat{\mathbf{k}}) \left( \frac{\partial f}{\partial k'} + \frac{l+1}{k'} f \right) \sqrt{\frac{(l-m-1)(l-m)}{2(2l-1)(2l+1)}} \times \\
& \quad \quad \left[ \left( \frac{l+m+1}{2l-1} \right) e^{-i\delta_{(l-1)+\frac{1}{2}}} \sin \delta_{(l-1)+\frac{1}{2}} + \left( \frac{l-m-2}{2l-1} \right) e^{-i\delta_{(l-1)-\frac{1}{2}}} \sin \delta_{(l-1)-\frac{1}{2}} \right] \left. \right\}. \tag{D.8}
\end{aligned}$$

With the help of the relations from appendix C, which lead to

$$\begin{aligned}
\int d\Omega_{\mathbf{k}} \left( Y_l^m(\hat{\mathbf{k}}) \right)^* k_x Y_{l+1}^{m-1}(\hat{\mathbf{k}}) &= \frac{k_F}{2} \sqrt{\frac{(l-m+1)(l-m+2)}{(2l+1)(2l+3)}} \\
\int d\Omega_{\mathbf{k}} \left( Y_l^m(\hat{\mathbf{k}}) \right)^* k_x Y_{l+1}^{m+1}(\hat{\mathbf{k}}) &= -\frac{k_F}{2} \sqrt{\frac{(l+m+1)(l+m+2)}{(2l+1)(2l+3)}} \\
\int d\Omega_{\mathbf{k}} \left( Y_l^m(\hat{\mathbf{k}}) \right)^* k_x Y_{l-1}^{m-1}(\hat{\mathbf{k}}) &= -\frac{k_F}{2} \sqrt{\frac{(l+m)(l+m-1)}{(2l+1)(2l-1)}} \\
\int d\Omega_{\mathbf{k}} \left( Y_l^m(\hat{\mathbf{k}}) \right)^* k_x Y_{l-1}^{m+1}(\hat{\mathbf{k}}) &= \frac{k_F}{2} \sqrt{\frac{(l-m)(l-m-1)}{(2l+1)(2l-1)}}, \tag{D.9}
\end{aligned}$$

the remaining integration over the angular part of  $\mathbf{k}$  can be executed. Consequently, the first contribution to the spin Hall conductivity due to side jump as written in equation (2.196) can be found.

For the derivation of the second side-jump contribution the expression from equation (D.8) is needed again but is used in the notation

$$\begin{aligned}
\int d\Omega_{\mathbf{k}''} \text{Im} \left\{ \tilde{T}_{\mathbf{k}\mathbf{k}''}^* \frac{\partial \tilde{T}_{\mathbf{k}\mathbf{k}''}}{\partial k_y''} \right\} &= \frac{16\pi^4 \hbar^6}{m_e^3 \sqrt{E_F}} \text{Re} \left\{ \sum_{l_1 m_1} \right. \\
&\left[ \left( \frac{l_1 + m_1 + 1}{2l_1 + 1} \right) e^{-i\delta_{l_1 + \frac{1}{2}}} \sin \delta_{l_1 + \frac{1}{2}} + \left( \frac{l_1 - m_1}{2l_1 + 1} \right) e^{-i\delta_{l_1 - \frac{1}{2}}} \sin \delta_{l_1 - \frac{1}{2}} \right] \sum_{lm} \left( Y_l^m(\hat{\mathbf{k}}) \right)^* Y_{l_1}^{m_1}(\hat{\mathbf{k}}) \times \\
&\left[ \left( \frac{\partial f}{\partial k'} - \frac{l}{k'} f \right) \left( \sqrt{\frac{(l-m+1)(l-m+2)}{(2l+1)(2l+3)}} \delta_{l_1, l+1} \delta_{m_1, m-1} + \sqrt{\frac{(l+m+1)(l+m+2)}{(2l+1)(2l+3)}} \delta_{l_1, l+1} \delta_{m_1, m+1} \right) \right. \\
&\left. - \left( \frac{\partial f}{\partial k'} + \frac{l+1}{k'} f \right) \left( \sqrt{\frac{(l+m-1)(l+m)}{(2l-1)(2l+1)}} \delta_{l_1, l-1} \delta_{m_1, m-1} + \sqrt{\frac{(l-m-1)(l-m)}{(2l-1)(2l+1)}} \delta_{l_1, l-1} \delta_{m_1, m+1} \right) \right] \left. \right\}. \tag{D.10}
\end{aligned}$$

Additionally, the contribution of the scattering-in term to the mean free path is taken into account by

$$\begin{aligned}
\sum_{\mathbf{k}'} P_{\mathbf{k}'\mathbf{k}} k_x' &= \frac{2\pi}{\hbar} c_0 N \frac{V m_e k_F}{(2\pi)^3 \hbar^2} \int d\Omega_{\mathbf{k}'} |\tilde{T}_{\mathbf{k}'\mathbf{k}}|^2 \sqrt{\frac{2\pi}{3}} k_F \left[ Y_1^{-1}(\hat{\mathbf{k}}') - Y_1^1(\hat{\mathbf{k}}') \right] \\
&= -\frac{c_0}{V_0} \frac{8\pi^2 \hbar}{m_e} \sum_{l_2 m_2} \sum_{l_3 m_3} \left( Y_{l_2}^{m_2}(\hat{\mathbf{k}}) \right)^* Y_{l_3}^{m_3}(\hat{\mathbf{k}}) \times \\
&\left[ \left( \frac{l_2 + m_2 + 1}{2l_2 + 1} \right) e^{-i\delta_{l_2 + \frac{1}{2}}} \sin \delta_{l_2 + \frac{1}{2}} + \left( \frac{l_2 - m_2}{2l_2 + 1} \right) e^{-i\delta_{l_2 - \frac{1}{2}}} \sin \delta_{l_2 - \frac{1}{2}} \right] \times \\
&\left[ \left( \frac{l_3 + m_3 + 1}{2l_3 + 1} \right) e^{-i\delta_{l_3 + \frac{1}{2}}} \sin \delta_{l_3 + \frac{1}{2}} + \left( \frac{l_3 - m_3}{2l_3 + 1} \right) e^{-i\delta_{l_3 - \frac{1}{2}}} \sin \delta_{l_3 - \frac{1}{2}} \right] \times \\
&\left[ \delta_{l_3, l_2 + 1} \left( \delta_{m_3, m_2 + 1} \sqrt{\frac{(l_2 + m_2 + 1)(l_2 + m_2 + 2)}{(2l_2 + 1)(2l_2 + 3)}} - \delta_{m_3, m_2 - 1} \sqrt{\frac{(l_2 - m_2 + 1)(l_2 - m_2 + 2)}{(2l_2 + 1)(2l_2 + 3)}} \right) \right. \\
&\left. - \delta_{l_3, l_2 - 1} \left( \delta_{m_3, m_2 + 1} \sqrt{\frac{(l_2 - m_2)(l_2 - m_2 - 1)}{(2l_2 + 1)(2l_2 - 1)}} - \delta_{m_3, m_2 - 1} \sqrt{\frac{(l_2 + m_2)(l_2 + m_2 - 1)}{(2l_2 + 1)(2l_2 - 1)}} \right) \right]. \tag{D.11}
\end{aligned}$$

The combination of equations (D.10) and (D.11) leads to integrals over four spherical harmonics which can be expressed in terms of Clebsch-Gordon coefficients (see section 5.6.2 of reference [87])

$$\begin{aligned} & \int d\Omega_{\mathbf{k}} \left( Y_l^m(\hat{\mathbf{k}}) \right)^* Y_{l_1}^{m_1}(\hat{\mathbf{k}}) Y_{l_2}^{m_2}(\hat{\mathbf{k}}) Y_{l_3}^{m_3}(\hat{\mathbf{k}}) \\ &= \sum_{LM} \sqrt{\frac{(2l_1+1)(2l_2+1)(2l_3+1)}{(4\pi)^2(2l+1)}} C_{l_1 0, l_2 0}^{L 0} C_{L 0, l_3 0}^{l 0} C_{l_1 m_1, l_2 m_2}^{LM} C_{LM, l_3 m_3}^{lm} \quad . \quad (\text{D.12}) \end{aligned}$$

Finally, equation (2.197) can be obtained and used to investigate the second contribution to the side-jump conductivity.





## Side-Jump Phase Shift Model - Comparison to Fert and Levy

---

In order to compare the expression for the side-jump conductivity obtained from the phase shift model with the one presented by Fert and Levy in [38], I will rederive it here. The starting point is the transition matrix (2.114) which is entirely the same as equation (1) in reference [38] if the spin-up channel is considered and the density of states of spin-up electrons per volume  $n(E_F) = \frac{\sqrt{2m_e^3}}{2\pi^2\hbar^3} \sqrt{E_F}$  is used. The derivative of the  $T$  matrix can be found similarly to equation (D.5) if the new form of  $f(E)$

$$f(E) = \frac{2}{n(E_F)} \left[ m \frac{\lambda_d}{\Delta} e^{2i\eta_2} \sin^2 \eta_2 - 2e^{i\eta_1} \sin \eta_1 \right] \quad (\text{E.1})$$

is used. Equation (E.1) already takes into account that in this derivation, only  $d$  electrons give rise to effects driven by spin-orbit coupling. Following the steps outlined in appendix D, it is straightforwardly possible to find

$$\int d\Omega_{\mathbf{k}'} T_{\mathbf{k}' \leftarrow \mathbf{k}}^* \frac{\partial}{\partial k'_y} T_{\mathbf{k}' \leftarrow \mathbf{k}} = \frac{4i}{\sqrt{2}n(E_F)} \sum_{m=-2}^2 \sum_{m'=-1}^1 e^{-im} \sin \eta_1 Y_1^{m'}(\hat{\mathbf{k}}) \left( Y_2^m(\hat{\mathbf{k}}) \right)^* \times$$

$$\left( \frac{\partial f}{\partial k'} + \frac{3}{k'} f \right) \left\{ \delta_{m',m-1} \sqrt{\frac{(1+m)(2+m)}{30}} + \delta_{m',m+1} \sqrt{\frac{(1-m)(2-m)}{30}} \right\} \quad (\text{E.2})$$

if the restrictions  $l = 2$  and  $l' = 1$  are used according to Fert and Levy with the  $T$  matrices labeled in the style of references [38, 79]. In a further approximation it is assumed that

$$\left( \frac{\partial f}{\partial k'} + \frac{3}{k'} f \right) \approx \left( \frac{\partial f}{\partial k'} \right) \approx \frac{4}{n(E_F)} \frac{\sin^2 \eta_2}{\Delta} \frac{\hbar^2 k_F}{m_e} \frac{\lambda_d}{\Delta} m e^{3i\eta_2} \sin \eta_2 \quad (\text{E.3})$$

where, according to [79], the relation

$$\frac{\partial \eta_2}{\partial k} = \frac{\partial \eta_2}{\partial E} \frac{\partial E}{\partial k} = \frac{\sin^2 \eta_2}{\Delta} \frac{\partial E}{\partial k} = \frac{\sin^2 \eta_2}{\Delta} \frac{\hbar^2 k}{m_e} \quad (\text{E.4})$$

was used. Taking into account equations (C.1) and (C.3), one finds

$$\int d\Omega_{\mathbf{k}} \int d\Omega_{\mathbf{k}'} T_{\mathbf{k}' \leftarrow \mathbf{k}}^* \frac{\partial}{\partial k'_y} T_{\mathbf{k}' \leftarrow \mathbf{k}} k_x = \frac{4i\hbar^2 k_F^2}{(n(E_F))^2 m_e} \frac{\lambda_d}{\Delta} \frac{\sin^2 \eta_2}{\Delta} e^{i(3\eta_2 - \eta_1)} \sin \eta_2 \sin \eta_1 \times$$

$$\sum_{m=-2}^2 \sum_{m'=-1}^1 m \left[ \delta_{m',m+1} \frac{(m-2)(m-1)}{15} - \delta_{m',m-1} \frac{(m+2)(m+1)}{15} \right] \quad (\text{E.5})$$

where the double series is equal to  $-4$ . Consequently, the expression

$$\text{Im} \int d\Omega_{\mathbf{k}} \int d\Omega_{\mathbf{k}'} T_{\mathbf{k}' \leftarrow \mathbf{k}}^* \frac{\partial}{\partial k'_y} T_{\mathbf{k}' \leftarrow \mathbf{k}} k_x = -\frac{16k_F^2 \hbar^2}{m_e (n(E_F))^2} \frac{\lambda_d \sin^2 \eta_2}{\Delta} \frac{\sin \eta_2 \sin \eta_1 \cos(3\eta_2 - \eta_1)}{\Delta} \quad (\text{E.6})$$

needed for the evaluation of the side-jump conductivity can be found. Finally, with the help of equation (2.191), the expression

$$\begin{aligned} \sigma_{yx}^{+, \text{sj}, \text{I}} &= - \left( \frac{e^2}{\hbar} \right) \frac{c_0}{V_0} \frac{m_e k_F^2}{(2\pi)^5 \hbar^3} \tau_0 \int d\Omega_{\mathbf{k}} \int d\Omega_{\mathbf{k}'} \text{Im} \left\{ \tilde{T}_{\mathbf{k}\mathbf{k}'}^* \frac{\partial \tilde{T}_{\mathbf{k}\mathbf{k}'}}{\partial k'_y} \right\} k_x \\ &= \left( \frac{e^2}{\hbar} \right) \frac{c_0}{V_0} \frac{4\hbar}{\pi m_e} \frac{\lambda_d E_F}{\Delta} \tau_0 \cos(3\eta_2 - \eta_1) \sin^3 \eta_2 \sin \eta_1 \end{aligned} \quad (\text{E.7})$$

is found. Obviously, equation (E.7) has opposite sign in comparison to the combination of equations (6) and (8) from [38].

Additionally, it is possible to derive a generalized expression for the side-jump conductivity in terms of non-relativistic phase shifts which takes into account all scattering events between  $s$ ,  $p$ ,  $d$ , and  $f$  electrons. The necessary steps can be executed equivalently to appendix D but starting with the transition matrix (2.114). Accordingly, one has

$$f(E) = \frac{1}{\sqrt{E}} \left[ \frac{m}{2} \frac{\lambda_l}{\Delta_l} e^{2i\eta_l(E)} \sin^2 \eta_l(E) - e^{i\eta_l(E)} \sin \eta_l(E) \right], \quad (\text{E.8})$$

which ultimately leads to

$$\begin{aligned} \sigma_{yx}^{+, \text{sj}, \text{I}} &= - \left( \frac{e^2}{\hbar} \right) \frac{c_0}{V_0} \frac{\hbar}{2\pi m_e} \tau_0 \sum_{lm} \\ &\text{Re} \left\{ G_{lm}^{(-(l+1))} \left[ \frac{(l-m+1)(l-m+2)}{(2l+1)(2l+3)} \left( e^{-i\eta_{l+1}} \sin \eta_{l+1} - \frac{m-1}{2} \frac{\lambda_{l+1}}{\Delta_{l+1}} e^{-2i\eta_{l+1}} \sin^2 \eta_{l+1} \right) \right. \right. \\ &\quad \left. \left. - \frac{(l+m+1)(l+m+2)}{(2l+1)(2l+3)} \left( e^{-i\eta_{l+1}} \sin \eta_{l+1} - \frac{m+1}{2} \frac{\lambda_{l+1}}{\Delta_{l+1}} e^{-2i\eta_{l+1}} \sin^2 \eta_{l+1} \right) \right] \right. \\ &\quad \left. + G_{lm}^{(l)} \left[ \frac{(l+m-1)(l+m)}{(2l-1)(2l+1)} \left( e^{-i\eta_{l-1}} \sin \eta_{l-1} - \frac{m-1}{2} \frac{\lambda_{l-1}}{\Delta_{l-1}} e^{-2i\eta_{l-1}} \sin^2 \eta_{l-1} \right) \right. \right. \\ &\quad \left. \left. - \frac{(l-m-1)(l-m)}{(2l-1)(2l+1)} \left( e^{-i\eta_{l-1}} \sin \eta_{l-1} - \frac{m+1}{2} \frac{\lambda_{l-1}}{\Delta_{l-1}} e^{-2i\eta_{l-1}} \sin^2 \eta_{l-1} \right) \right] \right\} \end{aligned} \quad (\text{E.9})$$

with

$$\begin{aligned} G_{lm}^{(\gamma)} &= 2E_F \left[ e^{2i\eta_l} - m \frac{\lambda_l}{\Delta_l} e^{3i\eta_l} \sin \eta_l \right] \frac{\partial \eta_l}{\partial E} + \gamma \left[ e^{i\eta_l} \sin \eta_l - \frac{m}{2} \frac{\lambda_l}{\Delta_l} e^{2i\eta_l} \sin^2 \eta_l \right] \\ &\quad - \frac{2m}{2l+1} E_F \frac{e^{2i\eta_l}}{\sin \eta_l} \left[ \left( \frac{\partial \delta_{l-\frac{1}{2}}}{\partial E} - \frac{\partial \delta_{l+\frac{1}{2}}}{\partial E} \right) \sin \eta_l - 2 \left( \delta_{l-\frac{1}{2}} - \delta_{l+\frac{1}{2}} \right) \cos \eta_l \frac{\partial \eta_l}{\partial E} \right], \end{aligned} \quad (\text{E.10})$$

where the relativistic phase shifts used to express the energy derivative of the term  $\frac{\lambda_l}{\Delta_l}$  originate from equation (2.178).

Besides the formulation in terms of non-relativistic phase shifts for the analysis of 5d impurities in Cu [38], Levy et al. also utilized the relativistic version for the description of side jump due to Bi impurities in Cu [94]. In order to execute the same comparison of the final expression as in the case of the non-relativistic approach, I start with

$$\int d\Omega_{\mathbf{k}'} \tilde{T}_{\mathbf{k}\mathbf{k}'}^* \frac{\partial \tilde{T}_{\mathbf{k}\mathbf{k}'}}{\partial k'_y} = \frac{i}{\sqrt{2}} \frac{32\pi^4 \hbar^6}{m_e^3 \sqrt{E}} \sum_{l'm'} \left[ \left( \frac{l'+m'+1}{2l'+1} \right) e^{-i\delta_{l'+\frac{1}{2}}} \sin \delta_{l'+\frac{1}{2}} + \left( \frac{l'-m'}{2l'+1} \right) e^{-i\delta_{l'-\frac{1}{2}}} \sin \delta_{l'-\frac{1}{2}} \right] \sum_{lm} \left( Y_l^m(\hat{\mathbf{k}}) \right)^* Y_{l'}^{m'}(\hat{\mathbf{k}}) \times \left\{ \left( \frac{\partial f}{\partial k'} - \frac{l}{k'} f \right) \left[ \sqrt{\frac{(l-m+1)(l-m+2)}{2(2l+1)(2l+3)}} \delta_{l',l+1} \delta_{m',m-1} + \sqrt{\frac{(l+m+1)(l+m+2)}{2(2l+1)(2l+3)}} \delta_{l',l+1} \delta_{m',m+1} \right] - \left( \frac{\partial f}{\partial k'} + \frac{l+1}{k'} f \right) \left[ \sqrt{\frac{(l+m-1)(l+m)}{2(2l-1)(2l+1)}} \delta_{l',l-1} \delta_{m',m-1} + \sqrt{\frac{(l-m-1)(l-m)}{2(2l-1)(2l+1)}} \delta_{l',l-1} \delta_{m',m+1} \right] \right\} \quad (\text{E.11})$$

from equation (D.8) together with equations (D.6) and (D.7). The predominant contributions to the SHE for the Cu(Bi) alloy come from *ps* scattering events. Accordingly,  $l = 1$  and  $l' = 0$  have to be chosen in the aforementioned equations. The derivation is straightforward and leads to

$$\int d\Omega_{\mathbf{k}} \int d\Omega_{\mathbf{k}'} \text{Im} \left\{ \tilde{T}_{\mathbf{k}\mathbf{k}'}^* \frac{\partial \tilde{T}_{\mathbf{k}\mathbf{k}'}}{\partial k'_y} \right\} k_x = \frac{32\pi^4 \hbar^6 k_F}{9m_e^3 E} \sin \delta_0 \left\{ \cos(2\delta_{3/2} - \delta_0) \frac{\partial}{\partial k} \delta_{3/2} - \cos(2\delta_{1/2} - \delta_0) \frac{\partial}{\partial k} \delta_{1/2} + \frac{1}{2k_F} [\sin(2\delta_{3/2} - \delta_0) - \sin(2\delta_{1/2} - \delta_0)] \right\} \quad (\text{E.12})$$

when the energy derivative of the phase shifts is replaced in favor of a  $k$  derivative according to

$$\frac{\partial}{\partial E} \delta_j = \frac{k_F}{2E_F} \frac{\partial}{\partial k} \delta_j. \quad (\text{E.13})$$

The application of equation (2.191) leads to

$$\sigma_{yx}^{+, \text{sj}, \text{I}} = \left( \frac{e^2}{\hbar} \right) \frac{c_0}{V_0} \frac{2\hbar k_F}{9\pi m_e} \tau_0 \sin \delta_0 \left\{ \cos(2\delta_{1/2} - \delta_0) \frac{\partial}{\partial k} \delta_{1/2} - \cos(2\delta_{3/2} - \delta_0) \frac{\partial}{\partial k} \delta_{3/2} + \frac{1}{2k_F} [\sin(2\delta_{1/2} - \delta_0) - \sin(2\delta_{3/2} - \delta_0)] \right\} \quad (\text{E.14})$$

where the last term in the curly brackets differs by a factor of two from equation [43] of reference [94]. This discrepancy can be solved by the consideration of the terms with  $l = 0$  and  $l' = 1$  and simultaneous negligence of terms including the energy

derivative of the  $s$  phase shifts  $\partial_E \delta_0$ . Accordingly, we find

$$\sigma_{yx}^{+,sj,I} = \left( \frac{e^2}{\hbar} \right) \frac{c_0}{V_0} \frac{2\hbar k_F}{9\pi m_e} \tau_0 \sin \delta_0 \left\{ \cos(2\delta_{1/2} - \delta_0) \frac{\partial}{\partial k} \delta_{1/2} - \cos(2\delta_{3/2} - \delta_0) \frac{\partial}{\partial k} \delta_{3/2} + \frac{1}{k_F} [\sin(2\delta_{1/2} - \delta_0) - \sin(2\delta_{3/2} - \delta_0)] \right\} \quad (\text{E.15})$$

in accordance with the approach of Levy et al. [94] especially with respect to sign<sup>5</sup>.

---

<sup>5</sup>One should take into account that reference [94] considers  $\rho_{yx}$  while we investigate  $\sigma_{yx}$ .

---

# Bibliography

---

- [1] **A. Fert**, *The present and the future of spintronics*. Thin Solid Films **517**, 2–5 (2008).
- [2] **I. Žutić, J. Fabian and S. Das Sarma**, *Spintronics: Fundamentals and applications*. Rev. Mod. Phys. **76**, 323 (2004).
- [3] **J. Brüggemann, S. Weiss, P. Nalbach and M. Thorwart**, *Cooling a Magnetic Nanoisland by Spin-Polarized Currents*. Phys. Rev. Lett. **113**, 076602 (2014).
- [4] **M. N. Baibich, J. M. Broto, A. Fert, F. N. Van Dau, F. Petroff, P. Etienne, G. Creuzet, A. Friederich and J. Chazelas**, *Giant Magnetoresistance of (001)Fe/(001)Cr Magnetic Superlattices*. Phys. Rev. Lett. **61**, 2472 (1988).
- [5] **G. Binasch, P. Grünberg, F. Saurenbach and W. Zinn**, *Enhanced magnetoresistance in layered magnetic structures with antiferromagnetic interlayer exchange*. Phys. Rev. B **39**, 4828 (1989).
- [6] **C. Chappert, A. Fert and F. N. V. Dau**, *The emergence of spin electronics in data storage*. Nat. Mater. **6**, 813 (2007).
- [7] **A. Fert**, *Nobel Lecture: Origin, development, and future of spintronics*. Rev. Mod. Phys. **80**, 1517 (2008).
- [8] **P. A. Grünberg**, *Nobel Lecture: From spin waves to giant magnetoresistance and beyond*. Rev. Mod. Phys. **80**, 1531 (2008).
- [9] **G. A. Prinz**, *Magnetoelectronics*. Science **282**, 1660 (1998).
- [10] **G. Schmidt, D. Ferrand, L. W. Molenkamp, A. T. Filip and B. J. van Wees**, *Fundamental obstacle for electrical spin injection from a ferromagnetic metal into a diffusive semiconductor*. Phys. Rev. B **62**, R4790 (2000).
- [11] **G. Schmidt**, *Concepts for spin injection into semiconductors – a review*. J. Phys. D **38**, R107 (2005).
- [12] **S. A. Wolf, D. D. Awschalom, R. A. Buhrman, J. M. Daughton, S. von Molnár, M. L. Roukes, A. Y. Chtchelkanova and D. M. Treger**, *Spintronics: A Spin-Based Electronics Vision for the Future*. Science **294**, 1488 (2001).
- [13] **N. F. Mott and H. S. W. Massey**, *Theory of Atomic Collisions*. Oxford University Press, London (1965).
- [14] **L. D. Landau and E. M. Lifshitz**, *Quantum Mechanics*. Pergamon (1965).
- [15] **J. E. Hirsch**, *Spin Hall Effect*. Phys. Rev. Lett. **83**, 1834 (1999).
- [16] **Y. K. Kato, R. C. Myers, A. C. Gossard and D. D. Awschalom**, *Observation of the Spin Hall Effect in Semiconductors*. Science **306**, 1910 (2004).

- 
- [17] **Y. V. Pershin, N. A. Sinitsyn, A. Kogan, A. Saxena and D. L. Smith**, *Spin polarization control by electric stirring: Proposal for a spintronic device*. Appl. Phys. Lett. **95**, 022114 (2009).
- [18] **E. H. Hall**, *On a New Action of the Magnet on Electric Currents*. Amer. J. Math. **2**, 287 (1879).
- [19] **E. H. Hall**, *On the Rotational Coefficient in Nickel and Cobalt*. Philos. Mag. **12**, 157 (1881).
- [20] **E. M. Pugh**, *Hall Effect and the Magnetic Properties of Some Ferromagnetic Materials*. Phys. Rev. **36**, 1503 (1930).
- [21] **E. M. Pugh and N. Rostoker**, *Hall Effect in Ferromagnetic Materials*. Rev. Mod. Phys. **25**, 151 (1953).
- [22] **N. A. Sinitsyn**, *Semiclassical theories of the anomalous Hall effect*. J. Phys.: Condens. Matter **20**, 023201 (2008).
- [23] **R. Karplus and J. M. Luttinger**, *Hall Effect in Ferromagnetics*. Phys. Rev. **95**, 1154 (1954).
- [24] **J. Smit**, *The spontaneous Hall effect in ferromagnetics - I*. Physica **21**, 877 (1955).
- [25] **J. Smit**, *The spontaneous Hall effect in ferromagnetics - II*. Physica **24**, 39 (1958).
- [26] **G. Vignale**, *Ten Years of Spin Hall Effect*. J. Supercond. Nov. Magn. **23**, 3 (2010).
- [27] **N. F. Mott**, *The Electrical Conductivity of Transition Metals*. Proc. R. Soc. London A **153**, 699 (1936).
- [28] **H. S. Nalwa**, editor, *Handbook of thin film materials*. Academic Press, San Diego (2002).
- [29] **N. Nagaosa**, *Anomalous Hall Effect —A New Perspective—*. J. Phys. Soc. Jpn **75**, 042001 (2006).
- [30] **T. Seki, Y. Hasegawa, S. Mitani, S. Takahashi, H. Imamura, S. Maekawa, J. Nitta and K. Tkanashi**, *Giant spin Hall effect in perpendicularly spin-polarized FePt/Au devices*. Nat. Mater. **7**, 125 (2008).
- [31] **G. Mihajlović, J. E. Pearson, M. A. Garcia, S. D. Bader and A. Hoffmann**, *Negative Nonlocal Resistance in Mesoscopic Gold Hall Bars: Absence of the Giant Spin Hall Effect*. Phys. Rev. Lett. **103**, 166601 (2009).
- [32] **O. Mosendz, J. E. Pearson, F. Y. Fradin, G. E. W. Bauer, S. D. Bader and A. Hoffmann**, *Quantifying Spin Hall Angles from Spin Pumping: Experiments and Theory*. Phys. Rev. Lett. **104**, 046601 (2010).
- [33] **S. Lowitzer, M. Gradhand, D. Ködderitzsch, D. V. Fedorov, I. Mertig and H. Ebert**, *Extrinsic and Intrinsic Contributions to the Spin Hall Effect of Alloys*. Phys. Rev. Lett. **106**, 056601 (2011).
-

- 
- [34] **M. Gradhand, D. V. Fedorov, P. Zahn and I. Mertig**, *Spin Hall angle versus spin diffusion length: Tailored by impurities*. Phys. Rev. B **81**, 245109 (2010).
- [35] **Y. Niimi, Y. Kawanishi, D. H. Wei, C. Deranlot, H. X. Yang, M. Chshiev, T. Valet, A. Fert and Y. Otani**, *Giant Spin Hall Effect Induced by Skew Scattering from Bismuth Impurities inside Thin Film CuBi Alloys*. Phys. Rev. Lett. **109**, 156602 (2012).
- [36] **M. Gradhand**, *The Extrinsic Spin Hall Effect*. Ph.D. thesis, Martin-Luther-Universität Halle-Wittenberg (2010).
- [37] **B. Gu, I. Sugai, T. Ziman, G. Y. Guo, N. Nagaosa, T. Seki, K. Takanashi and S. Maekawa**, *Surface-Assisted Spin Hall Effect in Au Films with Pt Impurities*. Phys. Rev. Lett. **105**, 216401 (2010).
- [38] **A. Fert and P. M. Levy**, *Spin Hall Effect Induced by Resonant Scattering on Impurities in Metals*. Phys. Rev. Lett. **106**, 157208 (2011).
- [39] **N. A. Sinitsyn, Q. Niu and A. H. MacDonald**, *Coordinate shift in the semiclassical Boltzmann equation and the anomalous Hall effect*. Phys. Rev. B **73**, 075318 (2006).
- [40] **M. Born and R. Oppenheimer**, *Zur Quantentheorie der Molekeln*. Ann. Phys. **84**, 457 (1927).
- [41] **N. W. Ashcroft and N. D. Mermin**, *Festkörperphysik*. Oldenbourg Verlag, München (2001).
- [42] **P. Hohenberg and W. Kohn**, *Inhomogeneous Electron Gas*. Phys. Rev. **136**, B864 (1964).
- [43] **W. Kohn and L. J. Sham**, *Self-Consistent Equations Including Exchange and Correlation Effects*. Phys. Rev. **140**, A1133 (1965).
- [44] **J. Zablouil, R. Hammerling, L. Szunyogh and P. Weinberger**, *Electron Scattering in Solid Matter*. Springer-Verlag Berlin Heidelberg New York (2005).
- [45] **P. Strange**, *Relativistic Quantum Mechanics: With Applications in Condensed Matter and Atomic Physics*. Cambridge University Press, Cambridge (1998).
- [46] **E. N. Economou**, *Green's Functions in Quantum Physics, Second Corrected and Updated Edition*. Springer-Verlag Berlin Heidelberg New York Tokyo (1983).
- [47] **J. Korringa**, *On the calculation of the energy of a Bloch wave in a metal*. Physica **13**, 392 (1947).
- [48] **W. Kohn and N. Rostoker**, *Solution of the Schrödinger Equation in Periodic Lattices with an Application to Metallic Lithium*. Phys. Rev. **94**, 1111 (1954).
- [49] **R. Zeller and P. H. Dederichs**, *Electronic Structure of Impurities in Cu, Calculated Self-Consistently by Korringa-Kohn-Rostoker Green's-Function Method*. Phys. Rev. Lett. **42**, 1713 (1979).
-

- 
- [50] **R. Podloucky, R. Zeller and P. H. Dederichs**, *Electronic structure of magnetic impurities calculated from first principles*. Phys. Rev. B **22**, 5777 (1980).
- [51] **P. J. Braspenning, R. Zeller, A. Lodder and P. H. Dederichs**, *Self-consistent cluster calculations with correct embedding for 3d, 4d, and some sp impurities in copper*. Phys. Rev. B **29**, 703 (1984).
- [52] **K. Wildberger, R. Zeller and P. H. Dederichs**, *Screened KKR-Green's-function method for layered systems*. Phys. Rev. B **55**, 10074 (1997).
- [53] **P. Zahn**, *Screened Korringa-Kohn-Rostoker-Methode für Vielfachschichten*. Ph.D. thesis, Technische Universität Dresden (1998).
- [54] **M. Czerner**, *Beiträge zur Theorie des Elektronentransports in Systemen mit nichtkollinearer magnetischer Ordnung*. Ph.D. thesis, Martin-Luther-Universität Halle-Wittenberg (2009).
- [55] **I. Mertig, E. Mrosan and P. Ziesche**, *Multiple Scattering Theory of Point Defects in Metals: Electronic Properties*. B.G. Teubner Verlagsgesellschaft Leipzig (1987).
- [56] **E. Merzbacher**, *Quantum Mechanics*. John Wiley & Sons Inc., New York (1998).
- [57] **J. Binder**, *Giant Magnetoresistance - eine ab-initio Beschreibung*. Ph.D. thesis, Technische Universität Dresden (2000).
- [58] **R. Zeller, P. H. Dederichs, B. Újfalussy, L. Szunyogh and P. Weinberger**, *Theory and convergence properties of the screened Korringa-Kohn-Rostoker method*. Phys. Rev. B **52**, 8807 (1995).
- [59] **N. Papanikolaou, R. Zeller and P. H. Dederichs**, *Conceptual improvements of the KKR method*. J. Phys.: Condens. Matter **14**, 2799 (2002).
- [60] **C. Herschbach**, *Spin-Hall-Effekt in ultradünnen Metallfilmen*. Master's thesis, Martin-Luther-Universität Halle-Wittenberg (2011).
- [61] **M. Gradhand, M. Czerner, D. V. Fedorov, P. Zahn, B. Y. Yavorsky, L. Szunyogh and I. Mertig**, *Spin polarization on Fermi surfaces of metals by the KKR method*. Phys. Rev. B **80**, 224413 (2009).
- [62] **J. Fabian and S. Das Sarma**, *Spin Relaxation of Conduction Electrons in Polyvalent Metals: Theory and a Realistic Calculation*. Phys. Rev. Lett. **81**, 5624 (1998).
- [63] **F. Pientka, M. Gradhand, D. V. Fedorov, I. Mertig and B. L. Györfy**, *Gauge freedom for degenerate Bloch states*. Phys. Rev. B **86**, 054413 (2012).
- [64] **J. M. Ziman**, *Prinzipien der Festkörpertheorie*. Akademie-Verlag Berlin (1974).
- [65] **I. Mertig**, *Transport properties of dilute alloys*. Rep. Prog. Phys. **62**, 237 (1999).
-



- 
- [66] **W. Kohn** and **J. M. Luttinger**, *Quantum Theory of Electrical Transport Phenomena*. Phys. Rev. **108**, 590 (1957).
- [67] **A. Fert**, **A. Friederich** and **A. Hamzic**, *Hall effect in dilute magnetic alloys*. J. Magn. Magn. Mater. **24**, 231 (1981).
- [68] **A. Fert** and **O. Jaoul**, *Left-Right Asymmetry in the Scattering of Electrons by Magnetic Impurities, and a Hall Effect*. Phys. Rev. Lett. **28**, 303 (1972).
- [69] **N. Nagaosa**, **J. Sinova**, **S. Onoda**, **A. H. MacDonald** and **N. P. Ong**, *Anomalous Hall effect*. Rev. Mod. Phys. **82**, 1539 (2010).
- [70] **M. V. Berry**, *Quantal phase factors accompanying adiabatic changes*. Proc. R. Soc. London A **392**, 45 (1984).
- [71] **R. Shindou** and **K.-I. Imura**, *Noncommutative geometry and non-Abelian Berry phase in the wave-packet dynamics of Bloch electrons*. Nucl. Phys. B **720**, 399 (2005).
- [72] **M. Gradhand**, **D. V. Fedorov**, **F. Pientka**, **P. Zahn**, **I. Mertig** and **B. L. Györfy**, *Calculating the Berry curvature of Bloch electrons using the KKR method*. Phys. Rev. B **84**, 075113 (2011).
- [73] **M. Gradhand**, **D. V. Fedorov**, **F. Pientka**, **P. Zahn**, **I. Mertig** and **B. L. Györfy**, *First-principle calculations of the Berry curvature of Bloch states for charge and spin transport of electrons*. J. Phys.: Condens. Matter **24**, 213202 (2012).
- [74] **X. Wang**, **J. R. Yates**, **I. Souza** and **D. Vanderbilt**, *Ab initio calculation of the anomalous Hall conductivity by Wannier interpolation*. Phys. Rev. B **74**, 195118 (2006).
- [75] **G. Y. Guo**, **S. Murakami**, **T.-W. Chen** and **N. Nagaosa**, *Intrinsic Spin Hall Effect in Platinum: First-Principles Calculations*. Phys. Rev. Lett. **100**, 096401 (2008).
- [76] **H.-A. Engel**, **B. I. Halperin** and **E. I. Rashba**, *Theory of Spin Hall Conductivity in n-Doped GaAs*. Phys. Rev. Lett. **95**, 166605 (2005).
- [77] **L. Berger**, *Side-Jump Mechanism for the Hall Effect of Ferromagnets*. Phys. Rev. B **2**, 4559 (1970).
- [78] **N. A. Sinitsyn**, **Q. Niu**, **J. Sinova** and **K. Nomura**, *Disorder effects in the anomalous Hall effect induced by Berry curvature*. Phys. Rev. B **72**, 045346 (2005).
- [79] **P. M. Levy**, *Extraordinary Hall effect in Kondo-type systems: Contributions from anomalous velocity*. Phys. Rev. B **38**, 6779 (1988).
- [80] **N. A. Sinitsyn**, **A. H. MacDonald**, **T. Jungwirth**, **V. K. Dugaev** and **J. Sinova**, *Anomalous Hall effect in a two-dimensional Dirac band: The link between the Kubo-Streda formula and the semiclassical Boltzmann equation approach*. Phys. Rev. B **75**, 045315 (2007).
-

- 
- [81] **J. Sinova, S. O. Valenzuela, J. Wunderlich, C. H. Back and T. Jungwirth**, *Spin Hall Effect*. arXiv:1411.3249 (2014).
- [82] **M. Gradhand, D. V. Fedorov, P. Zahn and I. Mertig**, *Extrinsic Spin Hall Effect from First Principles*. Phys. Rev. Lett. **104**, 186403 (2010).
- [83] **Monod, P. and Schultz, S.**, *Conduction electron spin-flip scattering by impurities in copper*. J. Phys. (Paris) **43**, 393 (1982).
- [84] **Y. Yafet**, *g Factors and Spin-Lattice Relaxation of Conduction Electrons*. Solid State Phys. **14**, 1 (1963).
- [85] **D. V. Fedorov, P. Zahn, M. Gradhand and I. Mertig**, *First-principles calculations of spin relaxation times of conduction electrons in Cu with nonmagnetic impurities*. Phys. Rev. B **77**, 092406 (2008).
- [86] **Y. Yafet**, *Conduction-Electron Spin Relaxation by Transition-Element Impurities in Copper*. J. Appl. Phys. **39**, 853 (1968).
- [87] **D. A. Varshalovich, A. N. Moskalev and V. K. Khersonskii**, *Quantum Theory of Angular Momentum*. World Scientific, Singapore (1988).
- [88] **M. Gradhand, D. V. Fedorov, P. Zahn and I. Mertig**, *Skew Scattering Mechanism by an Ab Initio Approach: extrinsic spin Hall effect in noble metals*. Solid State Phenom. **168**, 27 (2011).
- [89] **H. Ebert, H. Freyer, A. Vernes and G.-Y. Guo**, *Manipulation of the spin-orbit coupling using the Dirac equation for spin-dependent potentials*. Phys. Rev. B **53**, 7721 (1996).
- [90] **W. H. Butler**, *Theory of electronic transport in random alloys: Korringa-Kohn-Rostoker coherent-potential approximation*. Phys. Rev. B **31**, 3260 (1985).
- [91] **P. T. Coleridge**, *Impurity scattering in copper*. J. Phys. F **2**, 1016 (1972).
- [92] **X. Wang, J. Xiao, A. Manchon and S. Maekawa**, *Spin-Hall conductivity and electric polarization in metallic thin films*. Phys. Rev. B **87**, 081407 (2013).
- [93] **J. Sinova, D. Culcer, Q. Niu, N. A. Sinitsyn, T. Jungwirth and A. H. MacDonald**, *Universal Intrinsic Spin Hall Effect*. Phys. Rev. Lett. **92**, 126603 (2004).
- [94] **P. M. Levy, H. Yang, M. Chshiev and A. Fert**, *Spin Hall effect induced by Bi impurities in Cu: Skew scattering and side-jump*. Phys. Rev. B **88**, 214432 (2013).
- [95] **G. Y. Guo, Y. Yao and Q. Niu**, *Ab initio Calculation of the Intrinsic Spin Hall Effect in Semiconductors*. Phys. Rev. Lett. **94**, 226601 (2005).
- [96] **Y. Yao and Z. Fang**, *Sign Changes of Intrinsic Spin Hall Effect in Semiconductors and Simple Metals: First-Principles Calculations*. Phys. Rev. Lett. **95**, 156601 (2005).
-

- 
- [97] **M. Gradhand, D. V. Fedorov, P. Zahn, I. Mertig, Y. Otani, Y. Niimi, L. Vila and A. Fert**, *Perfect Alloys for Spin Hall Current-Induced Magnetization Switching*. SPIN **02**, 1250010 (2012).
- [98] **Y. Niimi, M. Morota, D. H. Wei, C. Deranlot, M. Basletic, A. Hamzic, A. Fert and Y. Otani**, *Extrinsic Spin Hall Effect Induced by Iridium Impurities in Copper*. Phys. Rev. Lett. **106**, 126601 (2011).
- [99] **P. Levy**. Private Communication (2013).
- [100] **A. Fert and P. M. Levy**, *Erratum: Spin Hall Effect Induced by Resonant Scattering on Impurities in Metals [Phys. Rev. Lett. 106, 157208 (2011)]*. Phys. Rev. Lett. **111**, 199904 (2013).
- [101] **G. Kresse and J. Hafner**, *Ab initio molecular-dynamics simulation of the liquid-metal–amorphous-semiconductor transition in germanium*. Phys. Rev. B **49**, 14251 (1994).
- [102] **P. E. Blöchl**, *Projector augmented-wave method*. Phys. Rev. B **50**, 17953 (1994).
- [103] **B. Gu, Z. Xu, M. Mori, T. Ziman and S. Maekawa**, *Sign and Magnitude of Spin Hall Effect in CuBi Alloys*. arXiv:1402.3012v1 (2014).
- [104] **Z. Xu, B. Gu, M. Mori, T. Ziman and S. Maekawa**, *Sign Change of the Spin Hall Effect due to Electron Correlation in Nonmagnetic CuIr Alloys*. Phys. Rev. Lett. **114**, 017202 (2015).
- [105] **J. Friedel**, *Metallic alloys*. Nuovo Cimento **7**, 287 (1958).
- [106] **P. J. Braspenning, R. Zeller, P. H. Dederichs and A. Lodder**, *Electronic structure of non-magnetic impurities in Cu*. J. Phys. F **12**, 105 (1982).
- [107] **A. A. Kovalev, J. Sinova and Y. Tserkovnyak**, *Anomalous Hall Effect in Disordered Multiband Metals*. Phys. Rev. Lett. **105**, 036601 (2010).
- [108] **J. Weischenberg, F. Freimuth, J. Sinova, S. Blügel and Y. Mokrousov**, *Ab Initio Theory of the Scattering-Independent Anomalous Hall Effect*. Phys. Rev. Lett. **107**, 106601 (2011).
- [109] **S. Lowitzer, D. Ködderitzsch and H. Ebert**, *Coherent Description of the Intrinsic and Extrinsic Anomalous Hall Effect in Disordered Alloys on an Ab Initio Level*. Phys. Rev. Lett. **105**, 266604 (2010).
- [110] **J. Griffith**, *The Theory of Transition-metal Ions*. Cambridge University Press, Cambridge (1961).
-



# List of Publications

---

- [H1] **C. Herschbach, M. Gradhand, D. V. Fedorov and I. Mertig**, *Enhancement of the spin Hall angle by quantum confinement*. Phys. Rev. B **85**, 195133 (2012).
- [H2] **D. V. Fedorov, C. Herschbach, A. Johansson, S. Ostanin, I. Mertig, M. Gradhand, K. Chadova, D. Ködderitzsch and H. Ebert**, *Analysis of the giant spin Hall effect in Cu(Bi) alloys*. Phys. Rev. B **88**, 085116 (2013).
- [H3] **C. Herschbach, D. V. Fedorov, I. Mertig, M. Gradhand, K. Chadova, H. Ebert and D. Ködderitzsch**, *Insight into the skew-scattering mechanism of the spin Hall effect: Potential scattering versus spin-orbit scattering*. Phys. Rev. B **88**, 205102 (2013).
- [H4] **A. Johansson, C. Herschbach, D. V. Fedorov, M. Gradhand and I. Mertig**, *Validity of the relativistic phase shift model for the extrinsic spin Hall effect in dilute metal alloys*. J. Phys.: Condens. Matter **26**, 274207 (2014).
- [H5] **C. Herschbach, D. V. Fedorov, M. Gradhand and I. Mertig**, *Colossal spin Hall effect in ultrathin metallic films*. Phys. Rev. B **90**, 180406(R) (2014).



# Eidesstattliche Erklärung

---

Hiermit erkläre ich gemäß §5 der Promotionsordnung der Naturwissenschaftlichen Fakultäten I, II, III und des Zentrums für Ingenieurwissenschaften der Martin-Luther-Universität Halle-Wittenberg vom 13.06.2012, dass ich die vorliegende Arbeit

## Optimization and Modeling of the Spin Hall Effect in Dilute Alloys A Theoretical Study

selbstständig und ohne fremde Hilfe verfasst, keine anderen als die angegebenen Quellen und Hilfsmittel benutzt und die den benutzten Werken wörtlich oder inhaltlich entnommenen Stellen als solche kenntlich gemacht habe. Ich erkläre weiterhin, die Angaben wahrheitsgemäß gemacht und weder diese noch eine andere Dissertation an einer anderen wissenschaftlichen Einrichtung vorgelegt zu haben.

Christian Herschbach





# Acknowledgment

---

At this point, I would like to take the opportunity to thank the people that supported me on the long road to this PhD thesis.

The first gratitude appertains to Prof. Dr. Ingrid Mertig who suggested the interesting topic. Additionally, her input in difficult phases of the project cleared my view on problems and enabled further progress. Furthermore, I have to thank her for the possibilities to visit conferences and workshops as well as for the chance to work together with great scientists as Balázs Gyórfy.

Special thanks go to my supervisor Dr. Dmitry Fedorov who escorted me during the long preceding journey. I really enjoyed the modality of our collaboration. Especially his affection for meticulousness impressed me. Thank you Dima for your outstanding support.

Another important supporter was Dr. Martin Gradhand who taught me the use of the *ab initio* codes. In addition, he maintained the project's progress by fresh-minded and irrespective comments in partially long e-mail conversations.

Besides the direct assistance of these collaborators, I want to thank the entire group *Quantum Theory of the Solid State* at the Martin Luther University Halle-Wittenberg for the pleasant working atmosphere. I really enjoyed the scooter on the floor and the comics at the door. In addition, the cluster administrators headed by Steven Achilles deserve gratitude for nearly undisturbed cluster performance.

Large parts to my contentment during almost nine years of studying physics were contributed by Matthias Geilhufe and Kilian Stumpf. Many discussions and short presentations during countless stays in the refectory improved my general education. And last but not least, I want to express special thanks to my family. In particular my parents and my brother had to dispense with me often but never stopped supporting me. Finally, I would like to thank my wife Madeleine for her lovely assistance during the last years.



# Curriculum Vitae

---

## Personal Data

name Christian Herschbach  
address Hyazinthenstraße 33, 06122 Halle  
date and place of birth April 16<sup>th</sup>, 1986 in Halle (Saale)

## University Education

since 04/2012 **Nano-IMPRS**, *Member of the International Max Planck Research School for Science and Technology of Nanostructures.*

since 11/2011 **Doctoral Studies**, *Martin Luther University Halle-Wittenberg.*

10/2009–10/2011 **Master degree course, M.Sc.**, *Martin Luther University Halle-Wittenberg, Halle, course specialization: theoretical physics, final grade 1.3.*  
*Master thesis: Spin-Hall-Effekt in ultradünnen Metallfilmen (Spin Hall Effect in Ultrathin Metallic Films)*

10/2006–09/2009 **Bachelor degree course, B.Sc.**, *Martin Luther University Halle-Wittenberg, Halle, final grade 1.2.*  
*Bachelor thesis: Untersuchung der Reflexions- und Transmissionszeiten beim Tunnelprozess (Investigation of Reflection and Transmission Times of the Quantum Tunneling Process)*

## Education and Civilian Service

10/2005–06/2006 **Civilian Service**, *Pharmacy of the BG Clinic Bergmannstrost, Halle.*

08/1996–07/2005 **Grammar School**, *“Gymnasium im Bildungszentrum”, Halle, final (Abitur) grade 1.1.*

08/1992–07/1996 **Elementary School**, *“Grundschule Ernest Hemingway”, Halle.*